

BRNO UNIVERSITY OF TECHNOLOGY

VYSOKÉ UČENÍ TECHNICKÉ V BRNĚ

CENTRAL EUROPEAN INSTITUTE OF TECHNOLOGY BUT

STŘEDOEVROPSKÝ TECHNOLOGICKÝ INSTITUT VUT

PREPARATION AND CHARACTERIZATION OF NANOSTRUCTURED III-V SEMICONDUCTOR MATERIALS

PŘÍPRAVA A CHARAKTERIZACE NANOSTRUKTURNÍCH III-V POLOVODIČOVÝCH MATERIÁLŮ

DOCTORAL THESIS

DIZERTAČNÍ PRÁCE

AUTHOR

Ing. Jaroslav Maniš

AUTOR PRÁCE

SUPERVISOR

prof. RNDr. Tomáš Šikola, CSc.

ŠKOLITEL

BRNO 2023

Abstract

The aim of the presented PhD thesis was to develop and analyze gallium nitride (GaN) nanostructures in three different forms. Firstly, three dimensional GaN nanocrystals prepared on graphene were studied from the perspective of the intrinsic crystal properties as well as growth statistics. Adopting the method of droplet epitaxy allowed the formation of such nanostructures at a low substrate temperature ($T \approx 200\,^{\circ}\text{C}$). In order to demonstrate possible applications, the proof of concept of an UV sensitive device was designed and tested with the successful results and the great promise to the future work. Secondly, two dimensional GaN nanostructures were prepared on a pristine silicon surface also at low temperature ($T \approx 200$ °C). Following experiments were focused on a study of a crystal structure and an elemental analysis as these structures have been observed for the first time. Two dimensional structures are promising candidates into the high power applications which are emerging in these days. Thus, preparation of such 2D GaN nanostructures serves as a solid foundation for the further research. Thirdly, one dimensional GaN horizontal nanowires were fabricated on different sapphire planes. The prepared nanowires provided adequate dataset for the subsequent data analysis related to the growth kinetics. Collected dataset was used for verification of the developed theoretical model of the nanowire growth. It has been shown that the theoretical model describes the growth of nanowires with great precision and, thus, provide a useful insight into the growth mechanisms.

Keywords: GaN, nanocrystals, nanowires, deposition, graphene, sapphire, scanning electron microscopy, atomic force microscopy, Raman spectroscopy

Abstract in Czech

Předkládaná dizertační práce se zabývá výrobou a analýzou gallium nitridových (GaN) nanostruktur ve třech odlišných formách. V prvním případě byl zkoumám trojdimenzionální GaN ve formě nanokrystalů rostených na grafenu. Nanokrystaly byly připraveny s využitím techniky droplet epitaxy, která mimo jiné umožňuje růst nanostruktur za nízké teploty substrátu ($T \approx 200$ °C). Studium se zaměřovalo jak na charakterizaci kvality připravených nanokrystalů, tak na statistický popis růstu. V dalším kroku byly připravené struktury využity pro výrobu fotodetektoru citlivého na ultrafialové světlo. Výroba fotodetektoru a jeho úspěšné použití slouží jako základ pro navazující výzkum. Ve druhém případě byly studovány dvoudimenzionální GaN nanostruktury, které byly rovněž připraveny za nízké teploty křemíkového substrátu. Následná analýza se soustředila na popis krystalové struktury a prvkovou analýzu, neboť byly takovéto struktury pozorovány vůbec poprvé. Další rozvoj možností přípravy těchto nanostruktur je předmětem navazujícího výzkumu. Ve třetím případě byly zkoumány jednodimenzionální GaN nanodráty připravené na safírovém substrátu. Účelem tohoto projektu bylo získání datasetu pro ověření teoretického modelu, který popisuje růst horizontálních nanodrátů. Na základě sběru a analýzy dat se podařilo modelovat růstovou dynamiku GaN nanodrátů, která byly v souladu s teoretickým modelem.

Klíčová slova: GaN, nanokrystaly, nanodráty, depozice, grafén, safír, skenovací elektronová mikroskopie, mikroskopie atomárních sil, Ramanova spektroskopie

Acknowledgment

I would like to express my gratitude to Prof. Tomas Sikola and Dr. Jindrich Mach whose expertise was invaluable in formulating the research directions and methodology. Your thorough feedback and support helped me to adopt the scientific habits and brought my experimental work to a new level.

I would also like to thank Prof. Ernesto Joselevich for the opportunity I was given to do an internship at the Weizmann Institute of Science. Your insightful comments and suggestions related to both scientific work and the country have made my life and study in Israel a wonderful time.

I would like to acknowledge my colleagues for their support, feedback and endless hours spent on stimulating discussions of scientific topics. The PhD study requires longtime focus on a given scientific topic but it also requires broadening of the ones knowledge in order to understand the relations and connections between various scientific disciplines. Therefore, it is highly desirable to be in touch with mentors and colleagues who pushed one to sharpen ones mind. Fortunately, I have found such mentors, colleagues and friends in the following people Ing. Tomas Musalek, Dr. Martin Konecny, Dr. Miroslav Kolibal, Ing. Lukas Kachtik and Dr. Amnon Rothman.

In addition, I would like to acknowledge Czech Science Foundation (grant no. 20-28573S), European Commission (H2020-Twininning project no. 810626 SINNCE, M-ERA NET HYSUCAP-TACR-TH71020004), BUT specific research no. FSI-S-20-6485, and Ministry of Education, Youth and Sports of the Czech Republic (CzechNanoLab Research Infrastructure LM2018110) for the financial support of the measurements and sample fabrication at the CEITEC Nano Research.

Finally, I would not be able to finish my PhD thesis without the invaluable support of my wife, Mgr. Ruzenka Manisova. Your encouragement, patience and belief in me helped me overcome all the obstacles which had emerged during my PhD study. In addition, I would like to thank my parents and sister for being there for me all the time.



Contents

Al	bstrac	ct		3
Al	bstrac	ct in Cz	zech	4
A	cknov	vledgn	ient	6
Co	onten	ts		9
1	Intr	oductio	on	12
2	Sem	icondu	ictors in the light of modern devices	16
	2.1	Role o	of III-nitride semiconductors	18
		2.1.1	Light-emitting diods	19
		2.1.2	High power devices	20
		2.1.3	Ultraviolet detectors and emitters	22
3	Obj	ectives	of presented PhD thesis	24
4	Phy	sical pl	henomena behind the growth of gallium nitride	27
	4.1	Molec	cular beam epitaxy	28
	4.2	Dropl	et epitaxy	31
		4.2.1	Means of elemental deposition	34
		4.2.2	Surface diffusion	36
		4.2.3	Ostwald ripening	39
	4.3	Chem	ical vapor deposition	41
	4.4	Physic	cal properties of gallium nitride	43
5	GaN	l nanoc	crystals on graphene	48
	5.1	Fabric	cation of GaN nanocrystals	51
		5.1.1	Sample preparation	51
		5.1.2	Formation of Ga islands on graphene	53
		5.1.3	Formation of GaN nanocrystals on graphene	58
	5.2	Fabric	cation of an UV sensitive photodetector	65
		5.2.1	Fabrication of electrodes	66
		5.2.2	Experimental setup	67

CONTENTS

		5.2.3 Response to the UV light	69
	5.3	Conclusion	72
6	Two	dimensional GaN	74
	6.1	Sample preparation	76
	6.2	Si (111) substrate with the 4° miscut	78
	6.3	Si (111) substrate with the 0.2° miscut	83
	6.4	Conclusion	91
7	GaN	N nanowires	93
	7.1	Sample preparation	96
	7.2	MOCVD gallium nitride nanowires	97
	7.3	CVD gallium nitride nanowires	102
		7.3.1 Kinetic model of horizontal nanowires	105
		7.3.2 Data fitting	110
	7.4	Conclusion	115
8	Con	clusion	117
9	Aut	hors publications and other outputs	118
Bi	bilio	graphy	119

1 Introduction

Semiconductors are the materials which revolutionized a human society as few technologies. "Even though, the evolution of mankind may seem as a linear process, the revolutions are the engine which drives the human society," says the neuroscientist and science popularizer V. S. Ramachandran [1]. The industrialization, the electrification, the automatization and the internetization. Four industrial revolutions which have brought the mankind to the new era [2]. The last two of them - the automatization and the internetization - were possible due to the rise of semiconductors without any doubts. The speed at which the human society has been mutually connected throughout last 70 years is unprecedented. The whole spectrum of devices enabling such connection - from GPS and telecommunication satellites orbiting the Earth to micro USB flash drives in our pockets - is the great example of how sci-fi has become reality.

Yet, we are still at the very beginning of our society transformation. According to professor of history at Hebrew University Y. N. Harari, the emerging artificial intelligence, industry 4.0, autonomous vehicles, 5G networks or social robots will not only change the way how we live but also change the way how we think since we will have to face and more importantly to answer some serious ethical questions which rise with such technologies [3]. The enormous number of semiconductors flooding every aspect of both industry and personal sphere increases environmental risks connected to the mining of rare elements or unregulated nanoparticles usage [4], social risks linked to a replacement of repetitive work in commercial and government sectors [5] and rises up ethical questions related to artificial intelligence [6]. However, these relevant questions are rather challenges than obstacles and will not hinder the technology development as says Collingridge's dilemma in which "design inevitably comes before ethical assessment since the design influences heavily how the technology will interact with society" [7].

Emerging new technologies will bring a fresh breeze and another acceleration to the semiconductor market as the semiconductors take place as base building blocks in a great number of appliances and gadgets. Despite the fact that the semiconductor global market revenue decreased by 12 % to \$412 billion in 2019, the forecast predicts further steady growth which has been observed for several years [8]. According to World Economic Fo-

rum, the global battery market is expected to grow 14 times and reach 2 400 GWh in 2030 [9]. Since those batteries will be part of the smart systems such as passengers electric cars and commercial vehicles, smart power grids or off-grid systems, they will be equipped with microprocessors or computers. In addition, complex protection circuitry and advanced sophisticated monitoring systems are expected to be incorporated in future solar power systems [10] or low power robotic applications in both industry and domestic use [11]. Brand new, and in these days still unpredictable market, appears to be Internet of Things (IoT) and all the devices such as data storage servers or communication systems related to it. A number of institutes or private offices forecasts unprecedented market share of IoT in tens of billions of U.S. dollars arguing that every single household will be equipped with numerous smart self-communicating devices resulting in billions of devices worldwide [12, 13]. However, in order to fulfill these predictions the semiconductor industry will be forced to overcome some significant challenges coming from the more basic levels - the physical limitations.

As the performance of functional devices such as light emitting diodes [14], thin-film transistors [15] or photovoltaic cells [16] is increasing and their dimensions are getting smaller, a strong interest to fabricate these devices in nanoscale rises. Sustained research and resolute determination enabled reduction of dimensions from the first point-contact transistor developed in Bell laboratories in 1947 by W. Shockley, J. Barden and W. Brattain to the Fin-FET transistors used in modern processors by a factor of 10⁷ [17]. However, one has to bear in mind that the reduction of dimensions changes material properties. Ratio of the number of surface atoms of a nanodevice to the number of its bulk atoms is getting higher as the dimensions of the device are getting smaller. Since the electronic and optical properties are determined by the distribution of atoms and electrons, the nanoscale objects have completely different properties to those in microscale. On top of that, the efforts to reduce the dimensions of functional devices are about to reach the limitations set by quantum mechanics. Among the others, a quantum confinement plays a crucial role in further reduction of nanodevices since it causes enlargement of the band gap energy.

As a consequence of above mentioned, scientists were forced to change the state of their minds in the past 20 years. Instead of using top-down methods for reducing the dimensions to nanometers scale, their effort have been strongly reoriented to the endeavour to fabri-

1 INTRODUCTION

cate new types of functional materials by using bottom-up methods. In these days, main scientific research in the field of nanotechnology is focusing on the 2D, 1D and even 0D nanostructures. Flat structures of a sub-nanometer thickness, nanotubes, nanowires and nanodots. All these structures are hot candidates for future functional devices in the light of new demands which are required by the modern nanotechnology discipline. However, relative novelty of these nanoscale structures limits their use in these days. Since the properties as well as mutual interactions of sub-3D nanostructures are quite unique, there is still space for a fundamental research.

The aim of the presented PhD thesis is to bring a pinch of knowledge to the already-built pile of understanding of semiconductors. Specifically, we are aiming to fabricate and describe the representative of III-nitride semiconductors - gallium nitride - in several forms. First, gallium nitride is fabricated in a form of nanocrystals on graphene which paves the way for adopting this multistructure into an ultraviolet light sensitive device. Second, fabrication of two dimensional gallium nitride is demonstrated accompanied with analysis of crystal structure in TEM. Third, gallium nitride is fabricated in a form of nanowires on sapphire substrates. These nanowires then served as a dataset for the study of kinetics and helped to support the theoretical description of horizontal nanowires growth.

2 Semiconductors in the light of modern devices

The history of semiconductors is a bibliography of the great minds of the past. From the first observation of a cork attracted by a charged glass made by Stephen Gray (1666 - 1736), through suggested concept of conductivity introduced by Jean-Theophile Desaguiliers (1683 - 1744) to observations of materials "which are actually permeable to the electric fluid, but oppose a strong resistance to its passage" as described them Alessandro Volta (1745 - 1827). Followed by Humphry Davys' (1778 - 1829) experiments on conductivity of materials such as copper, silver or iron and conductivity measurements of nonmetallic sulfides, oxides and carbides by Michael Faraday (1791 - 1867). In addition, reported passing current between a solid and a liquid electrolyte after irradiating with light observed by Alexandre Edmond Becquerel (1820 - 1891) and many other partial findings put together the solid foundations which then resulted into development of the first semiconductor device - point-contact rectifier - by Karl Ferdinand Braun (1850 - 1918) in 1874 [18, 19]. Those experimental observations were supported with a theoretical description in the first half of the last century resulting in developing a quantum band theory of solids by Alan Herries Wilson in 1931.

By the definition, the semiconductors are materials whose conductivity is lower than of metals but higher than in the case of insulators. Semiconductors can be also defined as the materials whose conductivity rises with increasing temperature. The theoretical description of a band structure can be found elsewhere [20]. The peculiar properties of the semiconductors may be explained by considering increasing number of charge carriers with rising temperature. The amount of charge carriers moving through a material dominates over the scattering caused by lattice vibrations. Thus, unlike in the metals, the resistivity of semiconductors is decreasing with increasing temperature. The number of charge carriers can be further increased by doping with additional atoms of element different from the bulk material. In that case, the conductivity can vary over several orders of magnitude.

The research of semiconductors was initially limited by the missing applications. This obstacle had changed before and during the World War II with the increased demands on high frequencies communication and development of radar [21]. It is not surprising that the breakthrough technology came a few years after the end of the WWII. The first point-contact transistor was built in 1947 [22]. Next decade was marked with outstanding work on field-

effect transistors and other semiconductor devices. The theory of "a unipolar "field-effect" transistor" was developed by William Shockley in 1952 [23]. The first grown n-p-n junction structure was developed in the same year followed by the first commercially available silicon device introduced in 1954. Another improvements followed in the late fifties with increasing quality of devices and introducing new architectures. Development of transistors is still running on in these days with the International Technology Roadmap for Semiconductor 2.0 forecasting sub-10 nm technology after 2021 [24].

Side by side with transistors, the other semiconductor devices have been developed in that period of time. Germanium tunnelling diodes and silicone diodes were reported in 1958. The first integrated circuit incorporating several devices on silicon wafer was demonstrated in the same year. The proposals of metal-oxide-semiconductor field-effect transistor (MOSFET) and complementary metal-oxide-semiconductor (CMOS) architectures were also presented. The charge-coupled device (CCD) concept was introduced couple of years later in 1970 [17].

As the research of semiconductor devices has been accelerated, the new concepts were proposed, developed or invented. In addition to the standard well-known semiconductors such as silicon, germanium or indium arsenide, the II-VI, III-V and other groups of semiconductors have been introduced. A special category is III-nitrides which enabled development of effective light-emitting diodes and which are promising for future high power and high temperature applications as will be discussed in the following Section 2.1.

2.1 Role of III-nitride semiconductors

The III-nitride semiconductors represent a group of materials in which representatives of the group-III of the periodic table of elements form chemically stable compounds with nitrogen. Namely, those are boron nitride (BN), aluminium nitride (AlN), gallium nitride (GaN), indium nitride (InN) and thallium nitride (TlN). The III-nitrides are hot candidates for using in modern electronic and photonic devices. The main reason for that is the range of band-gap values for individual compounds as well as tunability of it. Figure 1 (a) shows the band-gaps of binary III-nitride representatives spread over wide energy interval from 7 eV in case of a monolayer of AlN to 0.7 eV in case of a bulk InN [25, 26]. Moreover, tuning of stoichiometric ratio in ternary compounds leads to a continuous change in the wavelength emitted from such structures as illustrated in Figure 1 (b) [27].

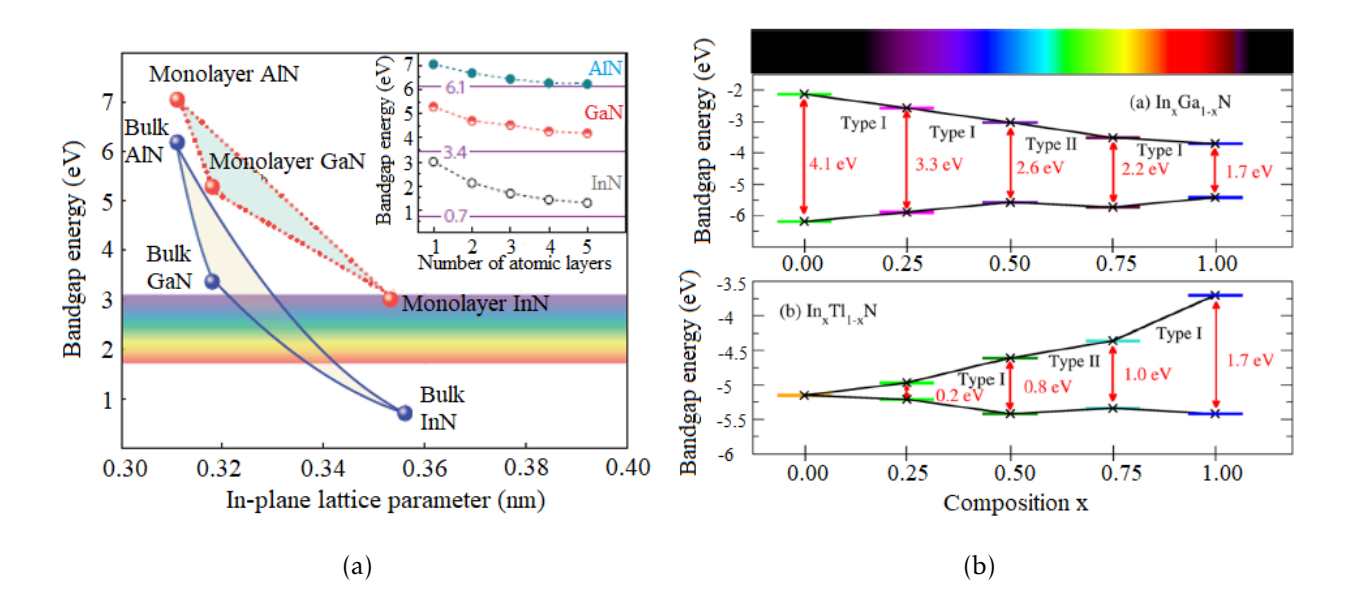


Figure 1: (a) Band-gap energies of III-nitrides with respect to the electromagnetic spectrum. Band-gap energies of hexagonal III-nitrides with respect to the number of monolayers is plotted in the inserted box [28]. (b) Composition-based tuning of band-gap energies in ternary compounds of $In_xGa_{1-x}N$ and $In_xTl_{1-x}N$ [27].

The suitability of materials for applications is defined by their electrical and optical properties. While a breakdown voltage and a thermal conductivity are relevant aspects for transistor, the materials useful for light emitting devices are sorted mostly based on a band-gap energy. Group-III nitrides provides promising candidates which could meet the requirements put upon these devices as the binary or ternary compounds cover whole spec-

trum from near infra-red represented by InN to deep ultraviolet representedy by AlN. Up to date, there is a number of devices covering infra-red [29, 30, 31], visible light [14, 32, 33] and ultraviolet part of the electromagnetic spectrum [34, 35, 36, 37, 38]. Three technologies based on III-nitrides which impacted the society or appears to be promising parts of advanced devices in the future are shortly described below. Of particular interest - with respect to the focus of the presented PhD thesis - is GaN whose physical properties are summarized in detail in Section 4.4.

2.1.1 Light-emitting diods

One of the technology based on III-nitrides worth mentioning is undoubtedly a blue light-emitting diode (LED) because the technological and social impact caused by this technology was enormous. The way to an efficient and ready-to-produce blue LED has been "a wonderful, though sometimes rocky, journey" as Nakamura admits in his Nobel lecture [14]. While the first red LED was introduced in 1962 followed by a green LED in 1968, the blue LED had a long way in ahead since the requirements on direct band-gap material with an appropriate wavelength emitted and a crystal quality of satisfactory level had not met for almost four decades. The beginning of the research of the blue LED can be traced back to the report on a Mg-doped GaN LED in 1973. For more than two decades the luminescence and physical properties of various III-V alloys had been studied and innovated which resulted in development of a GaN p-n junction in the early 90's [33]. The fruits of this labor could be implemented into more advanced technology such as a white LED using an InGaN blue LED which was commercialized in 1996 as is illustrated in Figure 2 (a).

Today, the comparison of efficiency and lifetime of an obsolete tungsten filament light bulb illustrates the impact of LEDs greatly. While the average filament light bulb requires approximately $60\,\mathrm{W}$ to produce brightness of $350\,\mathrm{lumen}$ (efficiency $6\,\mathrm{lm}\cdot\mathrm{W}^{-1}$), the LED requires only $5\,\mathrm{W}$ for the same brightness (efficiency $70\,\mathrm{lm}\cdot\mathrm{W}^{-1}$). In addition, the $2\,000\,\mathrm{hours}$ lifetime of the incandescent bulbs compared to $15\,000\,\mathrm{hours}$ in case of LEDs reveals the benefits of semiconductors based technology. Such arguments could be easily interpreted in a way that the LED lighting saves the energy consumption by far. In fact, recent studies have shown that the LED lighting technology reduced energy consumption only temporarily. As the cost of the LED lighting decreases significantly, the expansion of lighting in households

and a public sphere erodes the gains from more efficient technology [39]. Data spanned over three centuries, six continents and five lighting technologies gives a clear conclusion that "there is a massive potential for the growth in the consumption of light if new lighting technologies are developed with higher luminous efficacy and lower cost of light" [40]. Thus, the real impact of the LED technology is more likely an expansion of lighting rather than saving the energy.

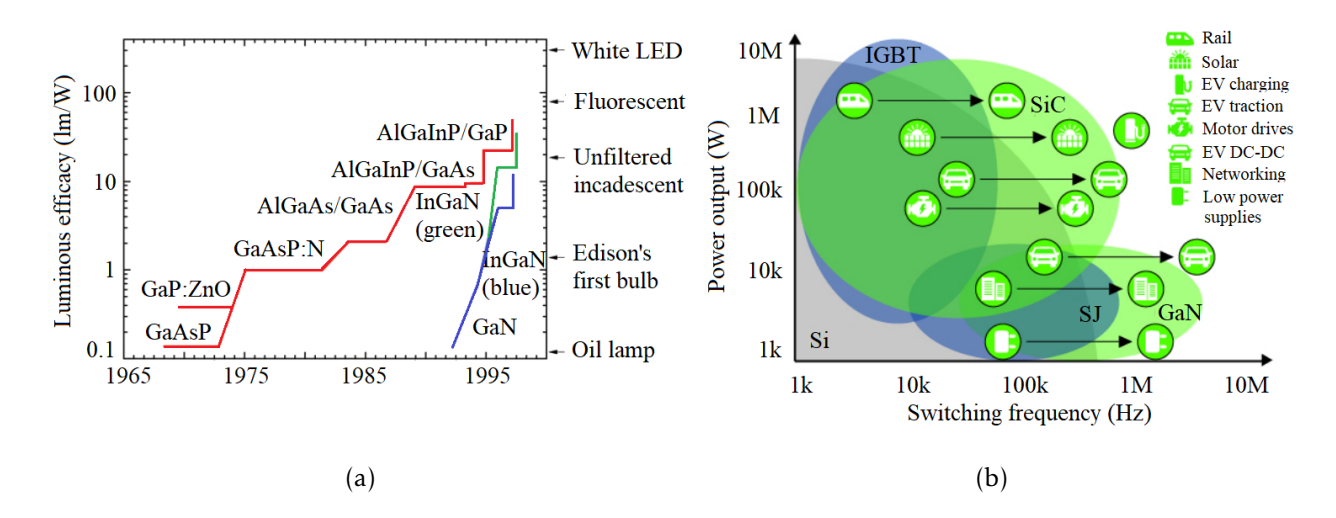


Figure 2: (a) Evolution of luminous efficiency of red, green and blue LEDs [14]. (b) Analysis of future transformation of chosen high voltage, high current applications from the perspective of power capabilities with respect to switching frequencies as a transformation from a silicon-based (Si) insulated gate bipolar transistor (IGBT) and super junction (SJ) devices towards the silicon carbide (SiC) and gallium nitride (GaN) based devices [41].

2.1.2 High power devices

Another benefit resulting from the wide band-gap semiconductors is their suitability for high power applications. The role of the power devices in the future technologies is diverse. From the microturbines designed to output power ranging from 25 kW to 500 kW to energy storage systems designed as stand-alone or smart grid subsystems [42]. As was mentioned above, the energy band-gap greatly influences the electronic properties of materials. For example, a higher band-gap energy leads to a higher breakdown voltage (the lowest voltage which causes destroying of the device). At the same time, a higher operational voltage allows to operate at lower currents which leads to a lower dissipation of energy, i.e. lower

energy loss.

Figure 2 (b) provides an insight to a very-well established silicon technology in various kinds of applications. However, silicon reaches its limits in high operation temperature and high switching frequency applications. In this sense, new candidates for high power devices have to be introduced to bring a new generation of high performance devices. Nowadays, the most promising candidate for high power applications is silicon carbide (SiC). With the 10 times higher breakdown voltage ($E_b = 4.9 \times 10^6 \,\mathrm{V} \cdot \mathrm{cm}^{-1}$) and 3 times higher thermal conductivity ($c_\tau = 3 \,\mathrm{W} \cdot \mathrm{cm}^{-1}$) in comparison with silicon, the operation temperature can be up to 200°C [43]. In fact, SiC Schottky diodes already compete with the Si power diodes on the commercial market. Their comparison at working voltage 1 200 V demonstrates a 30 % decrease in total power loss at 150°C in case of SiC Schottky diode [44].

In case of GaN, the major obstacle hindering the application usage is extremely difficult growth process of low defect density and crack free wafers resulting in a high cost per unit wafer area. Yet, the tremendous properties which predestines GaN for high power applications are still of particular interest. Instead of growing large volume bulky GaN, the effort is, thus, directed into a fabrication of heterostructures such as vertical GaN on Si wafer which combines the benefits of mature and low-cost technology of silicon wafer production and demands on materials suitability for high power electronics. The cost per unit wafer area illustrates the rationality of such approach without any doubts. The cost of 2 inch GaN-on-GaN wafer varies from \$60 to \$100 per cm². In comparison with 8 inch Gan-on-Si with the cost of \$1 per cm², the difference in cost is dramatic [45].

The comparison of electrical properties of 600 V Si MOSFET, 600 V SiC MOSFET and 600 V GaN HEMT (high electron mobility transistor) at the temperature of 150 °C provided in [46] shows superiority of SiC and GaN over Si. At frequency of 25 kHz and 50 % of duty cycle (a fraction of one period in which the device is active) the energy loss of silicon device was $205 \,\mu$ J which was more than 10 times higher than in case of SiC (17 μ J) and 20 times higher than in case of GaN device (10 μ J). So the state-of-the-art silicon technology together with promising III-nitrides' properties give a solid foundation for a following development of high power GaN-Si / SiC-Si devices and this trend will be probably speed up in the near future with new demands on new generation electronics [47].

2.1.3 Ultraviolet detectors and emitters

Ultraviolet (UV) detectors and emitters are widely used in advanced devices in both military and civil spheres. The ozone layer of the Earth hugely absorbs the radiation in the wavelength interval of 240 - 280 nm. For that reasons, these wavelengths are almost non-existent in the atmosphere. This UV spectral region is thus suitable for observing, for example, electrical discharges as a part of missile-detector systems [48, 49]. Another applications of UV devices could be their implementation into water purification processes [50]. Because of the continuing urbanization the good quality water supply starts to be a serious issue all over the world. The devices producing UV light could be suitable supplement to physical (e.g. filtration) and chemical (e.g. hydrochloride treatment) methods of removing the pollutants from the waste-water [51, 52].

Even though the ternary III-nitrides alloys bring benefit of continuously varying band-gap, high density of structural defects hinders their usage to some extent. Therefore, structures with higher structural quality such as nanowires are greatly explored as possible candidates for UV detector applications.

UV detectors can be in general distinguished into two categories - vacuum and solid-state detectors. Vacuum detectors are mature technology based on various types of photomultipliers with excellent gain and large area detection possibility. However, drawbacks such as weight, high power consumption and fragility give rise to the other group heavily based on semiconductors. A detailed review describing photoconductive, Schottky, p-n junction and p-i-n junction detectors can be found in [48] and [53]. For example, the CVD grown GaN nanowires acting as a photosensitive structure connected to the electrodes made of silver nanowires exhibit promising photoresponse to UV light from a xenon lamp [54]. Alternatively, an ultra-long (60-80 μ m) AlN nanowire bonded at the opposite ends with golden electrodes exhibits clear photoconductivity response to 325 nm light from He-Cd laser [55]. In both cases, III-nitrides structures were grown on Si/SiO₂ substrate but as other experimental works confirm it is also possible to introduce more unconventional substrates as reviewed in [56].

3 Objectives of presented PhD thesis

Objectives of the presented PhD thesis lay in the experimental work on fabrication and characterization of chosen III-nitrides nanostructures. Specifically, these are three-dimensional gallium nitride (GaN) nanocrystals, two-dimensional GaN nanosheets and one-dimensional GaN nanowires. In all three cases, the nanostructures were prepared using different methods and characterized using different analytic techniques.

The presented PhD thesis is divided into four parts. In the first part, used fabrication methods as well as general physical phenomena involved in the fabrication processes are briefly described in Section 4. Then, three sections dealing with individual projects are presented further in the thesis.

The experimental work on three-dimensional GaN nanocrystals is presented in Section 5. GaN nanocrystals were prepared using a droplet epitaxy growth technique in the laboratories of the Institute of Physical Engineering at Brno University of Technology (BUT) under supervision of Prof. Tomas Sikola and Dr. Jindrich Mach. Additional characterization such as SEM imaging, AFM imaging or Raman spectroscopy measurement were done at the Central European Institute of Technology (CEITEC) in Brno. Additionally, the proof of concept of utilizing such nanostructures into UV sensitive device was demonstrated.

An interesting phenomenon of a formation of 2D hexagonal GaN layers at specific conditions was observed during the work on UV sensitive devices. This phenomenon was further studied and the results are presented in the Section 6. Similarly as in the previous case, the experimental part of the work was done at the Institute of Physical Engineering at BUT while the characterization was carried out at CEITEC BUT. The results of this side project were published in [57] and presented by the author as an oral talk at the International Vacuum Conference in Malmö in 2019.

A fourth part of presented thesis, summarized in Section 7, deals with the CVD growth of GaN nanowires and the study of nanowires growth kinetics. The value of this project is in the connection between the theoretical model and its experimental verification. The experimental part of this project was done during an internship in the group of Prof. Ernesto

Joselevich in the Weizmann Institute of Science in Israel. The theoretical model was developed by Prof. Vladimir Dubrovskii at St. Petersborough University in Russia. The results of this project were published in *Nanomaterials* [58].

4 Physical phenomena behind the growth of gallium nitride

The growth of nanostructures is a complex process which is carried out in an ultra-high vacuum (UHV) system which is maintained to keep a very low base pressure ($p < 10^{-7} \, \text{Pa}$). A number of different aspects step into the fabrication process from the point of view of technological means as well as physical phenomena occurring during the nanostructures formation. This section tends to provide a short description of such phenomena and means since their understanding is essential for successful growth of nanostructures.

UHV systems have several specifics such as an absence of heat conduction through the air which, for instance, prolongs the cooling phase significantly. In addition, special sample holders are involved which also brings some limitation considering temperature control. On top of that, sources of deposited elements of different kinds with their characteristics (such as a ramp speed, an operation temperature or a flux rate) are of the great importance to maintain the system at appropriate working conditions.

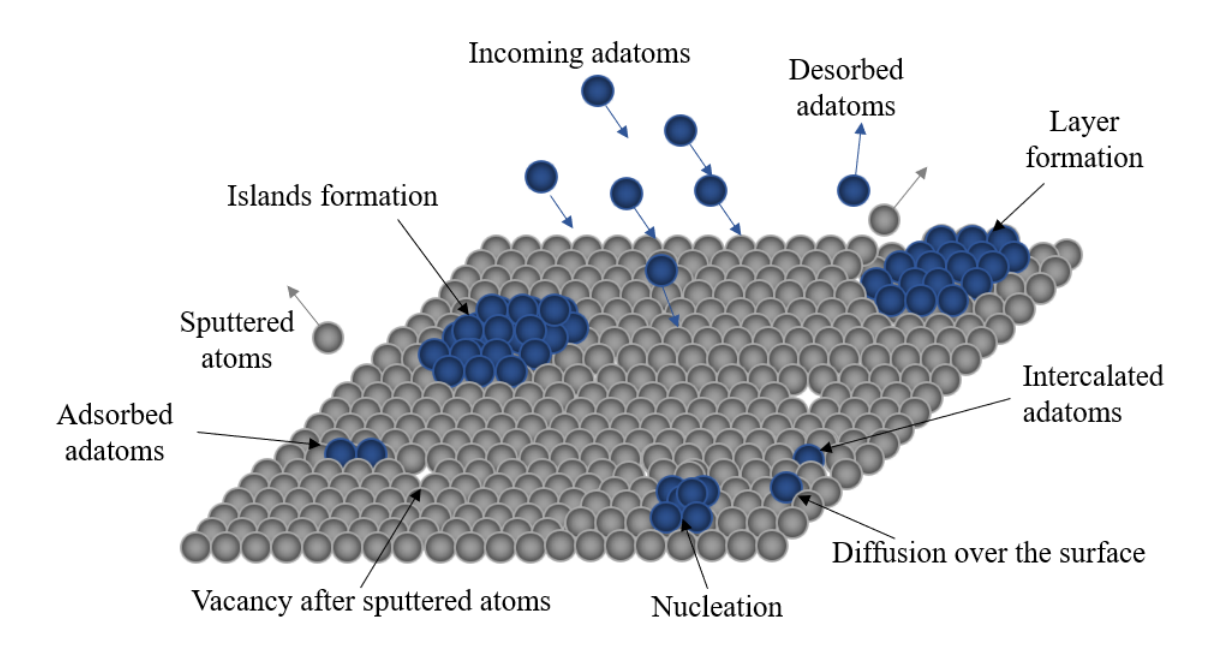


Figure 3: Surface dynamics involves a number of phenomena occurring on the surface after exposing it to the incoming beam of atoms.

Once those technological means are used for deposition, the physical phenomena occur during the deposition and formation process. A schematic representation of a surface dynamics is depicted in Figure 3. Adsorbed particles diffuse over the surface and coalescence together which results in an initiation of nucleation. Nuclei merge to the larger structures in the process called Ostwald ripening which can lead to a formation of islands or layers. In the same time, the atoms of a substrate can be sputtered off from the surface while the adatoms can fill up created vacancies. A substrate temperature, a surface energy, a flux rate or a time of deposition are major factors determining the processes occurring on the surface and define the nature and shape of formed nanostructures. Thus, the droplets, two dimensional structures, nanowires and other form of nanostructures can be observed.

To distinguish different kinds of nanostructures or, in general, to predict the nature of nanostructures formed at specific conditions, a sufficient level of knowledge is necessary. Therefore, a brief description of physical properties of the material of interest - *gallium nitride* - is provided in this section as well.

4.1 Molecular beam epitaxy

Molecular beam epitaxy (MBE) is one of the well-established and deeply understood fabrication technique for preparation of nanostructures of defined shapes and properties [59]. The additional value of MBE over other techniques is in the ability of controlled environmental and growth conditions such as:

- 1. The base pressure in the chamber is in the ultra-high vacuum region (below $p < 10^{-7} \,\mathrm{Pa}$).
- 2. The partial pressure of undesirable elements is kept at minimum.
- 3. Fluctuation of set temperatures over time is negligible.
- 4. Possibility of deposition of individual pure element is provided.
- 5. Flux rate of elements impinging on the substrate over time is constant.
- 6. Growth rate of nanostructures is controlled.
- 7. Subsequent analytical measurement of prepared structures is possible without exposing the nanostructures to the atmosphere.

The MBE technique has a long history through which a number of materials have been fabricated. Many of the materials were also synthesized by other methods but MBE is still a powerful tool for formation of III-nitrides [60, 61]. The ultimate ability of controlling the thickness is one of the greatest benefit of MBE allowing the growth of fine structures such as ferromagnetic thin films on flexible materials [62]. Despite the fact that MBE cannot provide such a growth rate as other techniques, it still has its place among nanostructure formation techniques such as fabrication of "beyond Si CMOS" devices [63].

In case of the presented work, a vacuum chamber for MBE was a part of a complex vacuum system, as depicted in Figure 4, located in the Institute of Physical Engineering at Brno University of Technology. The vacuum system consists of several separate vacuum chambers - a deposition chamber, an analytical (XPS) chamber, a carusel chamber and a load-lock chamber - which are mutually connected in order to allow the sample transfer between them. This arrangement brings a benefit of fabricating (MBE), analysing (X-ray photoelectron spectroscopy (XPS)) and storing the samples under UHV conditions. Each vacuum chamber is equipped with a turbomolecular pump, a rotary pump and an ion pump (XPS chamber also comprises a sublimation pump). Such a combination of pumps is sufficient to maintain the vacuum base level below $p < 10^{-7} \, \text{Pa}$ (usually about $9 \times 10^{-8} \, \text{Pa}$). The already published experimental work involving all the analytical means of said system is provided in [64].

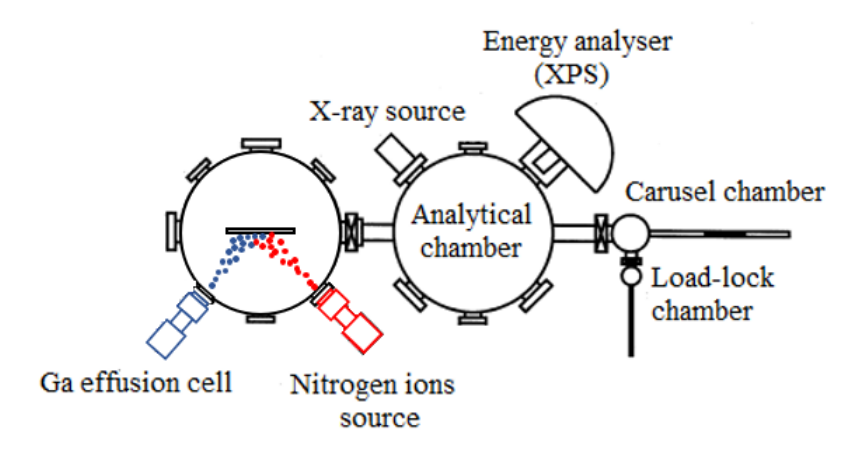


Figure 4: Schematic representation of a complex UHV system.

Sample transfer through the system is enabled by using a magnetic rod and a standardized set of sample holders. Sample holders are of two kinds - utilized for a direct current heating (Figure 5 (a)) and equipped with a pyrolitic boron nitride (PBN) heating plate (Figure 5 (b)). While the direct current heating allows to reach an arbitrary temperature (limitation is set by the melting point of the sample), the PBN heating plate provides uniformly distributed temperature which is stable over a long period of time.

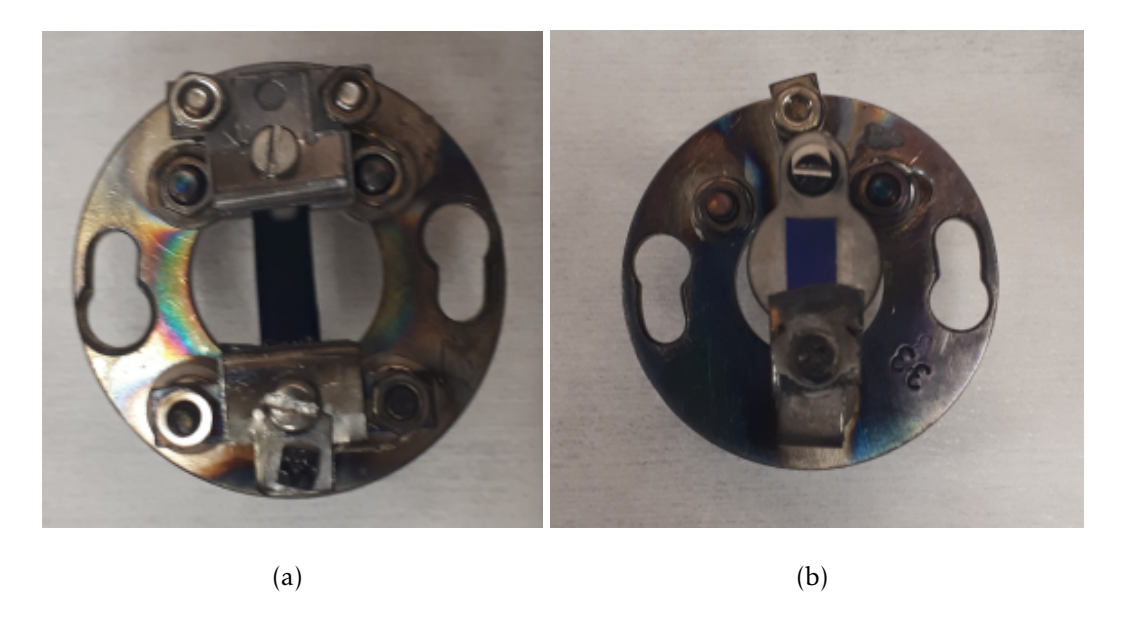


Figure 5: (a) Sample holder utilized for a direct current heating with typical $17 \times 4 \,\mathrm{mm}^2$ silicon sample loaded. (b) Sample holder equipped with a PBN plate with a typical $10 \times 4 \,\mathrm{mm}^2$ silicon sample loaded.

As was mentioned above, the temperature control in the UHV system is challenging. For that reason, both kinds of sample holders require calibration before its use. In the case of the direct current heating sample holder, the temperature of a sample is measured with pyrometer camera. Monitoring of the temperature is limited to the interval of $600^{\circ}\text{C}-1500^{\circ}\text{C}$ which is given by an optical transfer function of the pyrometer. For the temperatures below 600°C , the required temperature was extrapolated based on the linear function. Despite the fact that the measured temperature at given current is not linear function of the current, the linear function allows to set the same temperature for all measurements. In case of the sample holder equipped with PBN heating plate, the temperature was calibrated with a thermocouple. Thus, the combination of extrapolation based on linear function and the calibration based on thermocouple provided the correlation between the measured temperatures and set currents and voltages.

4.2 Droplet epitaxy

Droplet epitaxy (DE) is an alternative nanostructure growth technique utilized to be used in a standard molecular beam epitaxy (MBE) vacuum chamber. This technique was originally developed for GaAs quantum nanostructures but can be optimized for III-V nanostructures in general. The difference from the standard MBE nanostructures fabrication is in splitting the deposition process of group-III elements and group-V elements into two separate steps.

In the first step, the deposition of group-III element, e.g. gallium, is performed. Since the melting point of gallium is considerably low ($\approx 30\,^{\circ}$ C), it stays liquefied at almost all growth temperatures. Diameter of liquefied droplet is strongly dependent on the substrate temperature and the overall density of droplets on the surface is defined by the amount of gallium, i.e. flux rate over time of deposition, at defined temperature. Thus, the size and the coverage can be modulated by changing the substrate temperature and the flux rate. A critical role of the temperature and the flux rate illustrates the fact that at defined conditions a Ga droplet size dispersion is lower than $10\,^{\circ}$ [65].

Deposition of gallium establishes separate reservoirs of metallic gallium in the form of liquefied droplets of defined size spread over the surface with defined density. Once this step is finalized, the formation (crystallization) of required nanostructures can be done by irradiating those reservoirs with group-V elements. Similarly to Ga droplets formation, the substrate temperature and the flux rate are of same importance within this step. In this case, the substrate temperature and the flux rate significantly influence the shape of formed nanostructures. The crystalline nanostructures can be found in a ring, a double ring, a cone or a 'volcano' shape as illustrated in Figure 6 (a) [66].

In addition, a standard routine of DE can be modified by changing of the parameters during the crystalline nanostructures formation. Such modification is known as a pulsed droplet epitaxy (PDE) which is characterized by pulsing the supply of group-V element at the same or varying temperature. Advantage of PDE is a formation of complex quantum nanostructures such as ring-ring, dot-ring, ring-disc, etc. as shown in Figure 6 (b) [67, 68].

Droplet epitaxy brings a number of benefits into the controlled fabrication process of

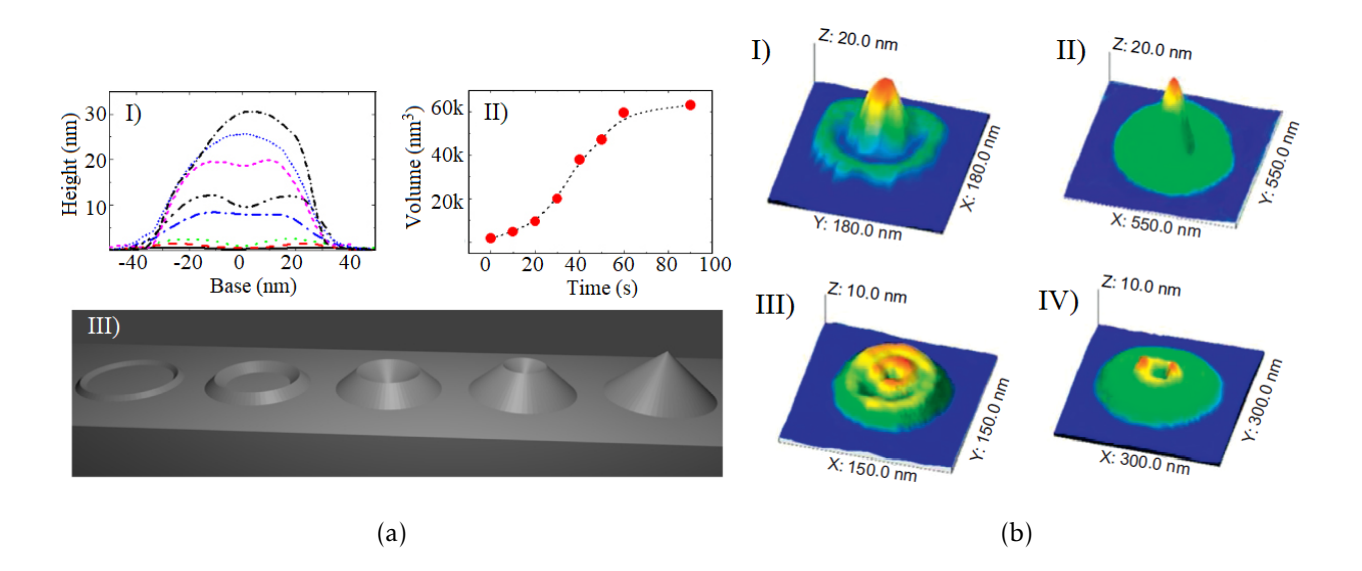


Figure 6: (a) Effect of deposition of group-V element on the shape and size of crystalline nanostructures (in this case Ga droplets were irradiated by As atoms). I) AFM profile of resulted structures. As the amount of As atoms is higher the nanostructures are bigger. II) The amount of As atoms increases with increasing time of post-irradiation. The volume of the grown nanostructures increases with time. III) The visualization of formed quantum nanostructures as a result of an increasing number of As atoms irradiating the Ga droplet [66]. (b) AFM profile of complex quantum nanostructures (the effect of pulsed droplet epitaxy): I) dot-ring, II) dot-disk, III) ring-ring, IV) ring-disk [67, 68].

nanostructures such as:

- 1. Size and density control by substrate temperature.
- 2. Density control over several orders of magnitude.
- 3. Growth suitability for lattice matched as well as lattice mismatched substrates.
- 4. Shaping of quantum nanostructures by changing the post-irradiation conditions.

Droplet epitaxy also brings a benefit of 3D growth of nanostructures since the very first moment of the growth. Due to the establishing of nucleation centers in the form of uniformly spread droplets, the growth is initiated only in the defined places. In comparison with the standard MBE in which the elements are supplied in the same time which results in a 2D lateral (Frank-van der Merwe) growth, a 3D island (Volmer-Weber) growth or their mutual combination in a Stranski-Krastanov growth mode, the DE is suitable for fabrication of defined periodical structures.

Despite the fact that the DE is a great technique for a growth of defined quantum nanostructures with defined periodicity, it needs to be taken into consideration that described method is suitable for *quantum* nanostructures of limited size only. If the density of gallium droplets is kept in the range of $10^8 \, \text{cm}^{-2}$ to $10^{11} \, \text{cm}^{-2}$, the DE type of growth of quantum nanostructures can be expected. However, as the density is higher the other surface mechanisms such as Ostwald ripening or coalescence of Ga droplets during the deposition are entering the growth process which can results in a formation of completely different nanostructures from the perspective of the size and density as well as electro-optical properties [65].

4.2.1 Means of elemental deposition

The gallium nitride nanostructures fabricated in the presented work were prepared in two-step deposition process. Firstly, the metallic gallium was deposited by an effusion cell. Secondly, the post-nitridation process was carried out using an ion-atomic nitrogen beam source.

Gallium effusion cell

The gallium effusion cell used in the presented work was a Knudsen type of effusion cell. Such a cell consists of a crucible, a heating filament, a collimator and a shutter as illustrated in Figure 7. The heating filament made of tantalum or tungsten is connected to the control unit which provides a current (usually about $I = 2\,\mathrm{A}$). The current flowing through the filament causes its heating which results in a thermionic emission of electrons. These electrons are subsequently accelerated towards the crucible by applied voltage of $U = 800\,\mathrm{V}$. The amount of emitted electrons is measured by an emission current which is usually about $\epsilon = 30\,\mathrm{mA}$.

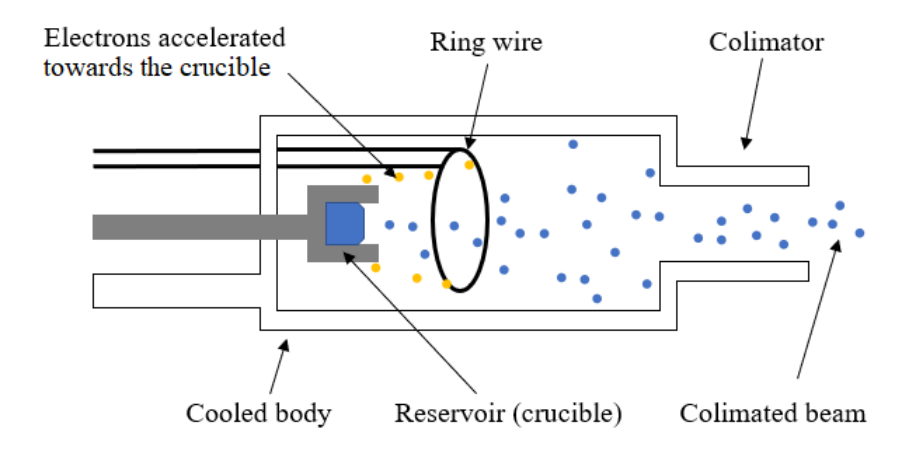


Figure 7: Schematic visualization of a gallium effusion cell.

Electrons impacting on the Mo crucible (with a pyrolitical boron nitride cup inside) cause its heating which leads to a sublimation or evaporation of the material inside - in this particular case gallium (in order to reach a sufficient gallium vapor pressure $(1\times 10^{-2}\,\mathrm{Pa})$, the temperature has to reach $T_\mathrm{M}=950\,^\circ\mathrm{C}$). At the usual emission current of $\epsilon=30\,\mathrm{mA}$ the flux of gallium atoms is about $f=1.4\times 10^{13}\,\mathrm{cm}^{-2}\cdot\mathrm{s}^{-1}$ which corresponds to $0.2\,\mathrm{ML}\cdot\mathrm{min}^{-2}$. The beam of gallium atoms is spatially collimated by the collimator which directs the beam

towards the sample. The arrangement of an MBE chamber defines the impinging angle of gallium atoms on the sample close to 55° with respect to the sample surface normal.

The temperature stability of the effusion cell is secured by a water cooling. The water cooling prevents the body of the effusion cell made of oxygen-free copper (copper purity is greater than 99.996%) from overheating. The final part of the effusion cell - the shutter - ensures the immediate control of a deposition state - on/off. This metallic plate placed above the collimator can be rotated in that way that obstructs the beam path, partially obstructs the beam path or provides free path to the substrate.

Ion-atomic nitrogen beam

The ion-atomic nitrogen beam is designed to provide the mixture of gallium atoms and low energy nitrogen ions as reported in [69]. However, the operation mode used in presented work was chosen to produce nitrogen ions only since the gallium atoms were provided by the gallium effusion cell.

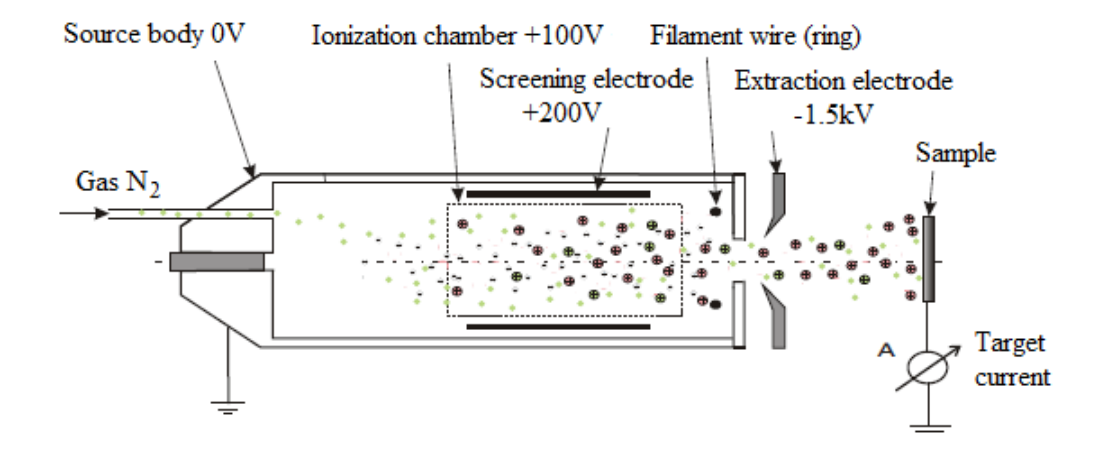


Figure 8: Schematic visualization of an ion-atomic nitrogen source [69].

The ion-atomic nitrogen source is depicted in Figure 8. The nitrogen N_2 gas (of purity 99.9999%) is injected into an ionization chamber from the side. The nitrogen gas partial pressure is kept at 5.5×10^{-5} Pa in the deposition chamber. A tungsten filament wire is placed in the opposite side of the ionization chamber. Current (I = 5.4A) passing through

the filament ring causes thermoemission of electrons from the wire with the initial energy ranging from 0.1 eV to 2 eV. These electrons are accelerated towards a cylindrical ionization grid which is at potential of U = 50V placed in the middle part of the ionization chamber. The collisions of accelerated electrons with the nitrogen gas results in ionization of N_2 molecules. Subsequently, the mixture of N_2^+ , N_2^{2+} , N^+ , N^{2+} is accelerated towards the extraction electrodes at which the negative potential of U = -1500V is applied and spatial collimated to the cone by a collimation electrode (U = -500V). The nitrogen current density measured by a Faraday cup is approximately I = 1000nA·cm⁻² which can be recalculated to the flux rate of 6.24×10^{12} cm⁻²·s⁻¹.

The efficiency of nitrogen molecules ionization (an ionization cross-section) is the highest if the electrons energy is near to $E = 100 \,\text{eV}$. In the same time, the energy of nitrogen ions is determined by the potential applied to a cylindrical grid. Thus, an additional screening electrode is placed in the ionization chamber to ensure the $100 \,\text{eV}$ ionization energy at an arbitrary grid potential.

4.2.2 Surface diffusion

Surface diffusion is a thermodynamic process of a random motion of adatoms (or adparticles in general) over the surface which is thermally activated. In presence of a concentration gradient, the diffusion (random motion) of each individual adatoms results in a net diffusion in the direction opposite to the direction of the gradient.

Figure 9 (a) shows a schematic representation of an adatom on the surface in the stable position of an adsorption site (1) and metastable position of a transition (bridge) site (2). The energy necessary to hopping from one adsorption (minimum energy) site to another is equal to the activation energy of diffusion E_{diff} which can be defined as a difference of the minimum (1) and maximum (2) in potential energy as can be seen from Figure 9 (b). A random site-to-site hopping of the adatom can be represented by the mean-square displacement $\langle \delta r^2 \rangle$ over time t as follows:

$$\langle \delta r^2 \rangle = \nu_{\text{eff}} a^2 t,\tag{1}$$

where the a is a site-to-site distance (jump distance) and $v_{\rm eff}$ is an effective hopping

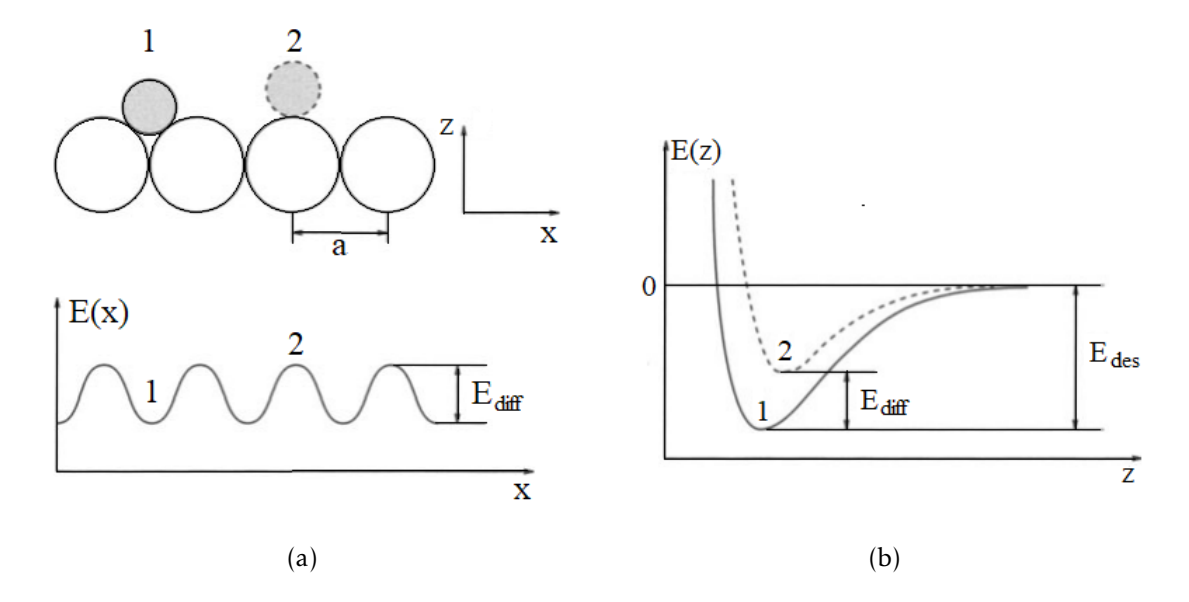


Figure 9: (a) Representation of stable position (1) and metastable position (2) of adatoms on a surface. Corresponding potential defines the activation energy of diffusion (site-to-site jump) E_{diff} as a difference between minimum energy (1) and maximum energy (2) position. (b) Potential energy of adatoms in position (1) and (2) as a function of position z. E_{des} corresponds with the energy of desorption of an adatom from the surface [70].

frequency (so the $v_{\rm eff}t$ equals to a number of jumps over time t). As was mentioned above, the diffusion is a thermodynamic process driven by thermal excitation. For that reason, the $v_{\rm eff}$ is modified by a Boltzman factor which represent the probability of thermal excitation corresponding to the energy of diffusion $E_{\rm diff}$

$$v_{\text{eff}} = v e^{-\frac{E_{\text{diff}}}{k_{\text{B}}T}},\tag{2}$$

where ν is a hopping frequency, $k_{\rm B}$ is a Boltzman constant and T is an absolute temperature.

Ratio of mean-square displacement over the number of available neighboring sites z in time t is known as a time-independent *diffusion coefficient*

$$D = \frac{\langle \delta r^2 \rangle}{zt} = \frac{\nu_{\text{eff}} a^2}{z}.$$
 (3)

where z=2 represents the one dimensional diffusion, z=4 diffusion over the square surface and z=6 diffusion over the hexagonal surface. Naturally, the different surfaces has also different activation energies of diffusion $E_{\rm diff}$, i.e. different effective hopping frequency $\nu_{\rm eff}$.

Considering the ensemble of adparticles which is define by the concentration of particles on a surface ρ (for example atoms per cm⁻²) the definition of a *diffusion current J* can be formulated as

$$J = -D\nabla \rho,\tag{4}$$

where $\nabla \rho$ is a gradient of concentration of adatoms. Therefore, the direction of the diffusion current is opposite to the gradient of concentration (i.e. adatoms diffuse from an area of higher concentration to an area of lower concentration). Obviously, provided explanation is rather quantitative to express the diffusion from the point of view of a single atom. The more statistical approach can be found in [71] while the deeply theoretical approach can be found in [72].

The measurement of diffusion coefficients and corresponding diffusion lengths vary for different combinations of adsorbed particles and surfaces. A number of methods have already been developed allowing measurement of diffusion coefficient D in the range of $(10^{-17}-10^{-5})\,\mathrm{cm}^{-2}\cdot\mathrm{s}^{-1}$ and corresponding diffusion length in the range of $(10^{-8}-10^{-2})\,\mathrm{cm}$) [71]. In case of gallium, the diffusion coefficient as well as activation energy varies based on the method used. In order to provide at least general idea the activation energy of diffusion E_{diff} varies from $0.3\,\mathrm{eV}$ to $4\,\mathrm{eV}$ and diffusion coefficient D varies from $0.85\times10^{-5}\,\mathrm{cm}^{-2}\cdot\mathrm{s}^{-1}$ to $0.2\,\mathrm{cm}^{-2}\cdot\mathrm{s}^{-1}$ in case of Ga adatoms diffusing over GaAs(001) surface [73]. Such a dispersion is caused by (i) different methods of measurement (e.g. extrapolation of parameters based on measurements at varying temperatures), (ii) a cleanliness of the substrate [74].

It is worth mentioning that the study of surface diffusion has not only theoretical consequences of knowing parameters of an activation energy or a diffusion coefficient. Interestingly enough, the diffusion can be used for determining the shape of nanoparticles as reported for example in [75] which paves the way for using of knowledge of diffusion parameters for formation of different nanostructures. Vice versa, if the shape of nanoparticles can be intentionally modified by diffusion, then it is natural to expect that the diffusion plays a significant role in determining shape of nanoparticles in general.

Alternatively to a diffusion coefficient, a diffusion length can be used as a numerical characteristic of diffusion. There are two definition of the diffusion length which can be

applied. First, the diffusion length can be defined as an average distance between the point where the atoms was adsorbed and the point where it was re-evaporated. Second, the definition of diffusion length can take into consideration that the adatoms are incorporated into formed structures. In this case, the diffusion length is equal to an average distance between the point of arrival and the point in where an atom is incorporated into the surface structure [76].

4.2.3 Ostwald ripening

Ostwald ripening (also known as coarsening) is a thermodynamic diffuse-control process in two-phase mixtures. Coarsening can be observed in the systems with varying size of particles dispersed in matrix but can be also adopted for particles on a surface. During the Ostwald ripening, the large crystals grow in size while small particles shrink as a result of decreasing total free energy of the system. The theoretical end point of this process is a one particle containing all the material of one phase embedded by the second phase [77].

First quantitative description of the process was provided by W. Ostwald in 1901. It took almost 60 years before Lifshitz, Slyozov and Wagner developed the first theoretical description (known as LWS theory) [77]. However, following experimental work could not reach a perfect match between the theoretical prediction and experimental results. Up to now, there is no full theory which would described the Ostwald ripening in full scale. There is a number of modern theories which deals with the coarsening phenomenon reviewed in [78] but as author claims none of the theories fully describe whole phenomenon.

First step into the theoretical description of Ostwald ripening can be made with the equation describing the evolution of a radii r in time t:

$$\frac{\mathrm{dr}}{\mathrm{dt}} = -\frac{2D\Omega\gamma}{R_{\mathrm{B}}T} \left(\frac{1}{r} - \frac{1}{r_{\mathrm{A}}}\right),\tag{5}$$

in where D is a diffusion coefficient of the particle in a matrix (or on a surface), Ω is a mean volume of the particle, γ is a specific interfacial energy of particle-matrix interface (or a surface energy), $R_{\rm B}$ is a universal gas constant, T is absolute temperature and $r_{\rm A}$ is an average diameter of particles dispersed in a matrix (or on a surface). The fraction before a bracket is a constant depending on a material of concern. The important part allowing

quantitative evaluation is only variable r which can be lower or bigger than r_A :

for
$$r < r_A$$
, $\frac{dr}{dt} < 0$, (6)

for
$$r > r_A$$
, $\frac{dr}{dt} > 0$. (7)

The explanation of positive or negative change of radius with respect to time $\frac{dr}{dt}$ could be as follows. Ensemble of particles dispersed in a matrix (or on a surface) is defined by their average radius r_A . From the point of view of each individual particle, if a particle has smaller radius r than an average radius r_A , the particle tends to shrink. Vice versa, the particle with bigger radius r than average radius r_A tends to increase its radius (i.e. volume) [79]. As was mentioned above, the driving force of Ostwald ripening is a decrease of a total energy. The energy of the particle is defined by the ratio of surface atoms to volume atoms. The smaller the particle, the higher the number of surface atoms, the higher the ratio of surface versus volume atoms and the higher the energy. Thus, Ostwald coarsening results in a formation of particles with smaller surface to volume atoms ratio which leads to a decrease in the total energy of a system eventually.

4.3 Chemical vapor deposition

Chemical vapor deposition (CVD) is a well-established technique for the growth of variety of nano- and micro- structures which is heavily used in semiconductor industry for a production of vast range of solid materials. The CVD is based on a heat decomposition of volatile precursors and their subsequent reaction resulting in a formation of desired materials.

Over the years a number of CVD modifications have been introduced to satisfy the demands for alternative materials. To give a few examples, the plasma enhanced CVD (PECVD) in where the plasma enhances chemical reaction rate or metal organic CVD (MOCVD) in where the metal organic compounds are used as precursors have been developed.

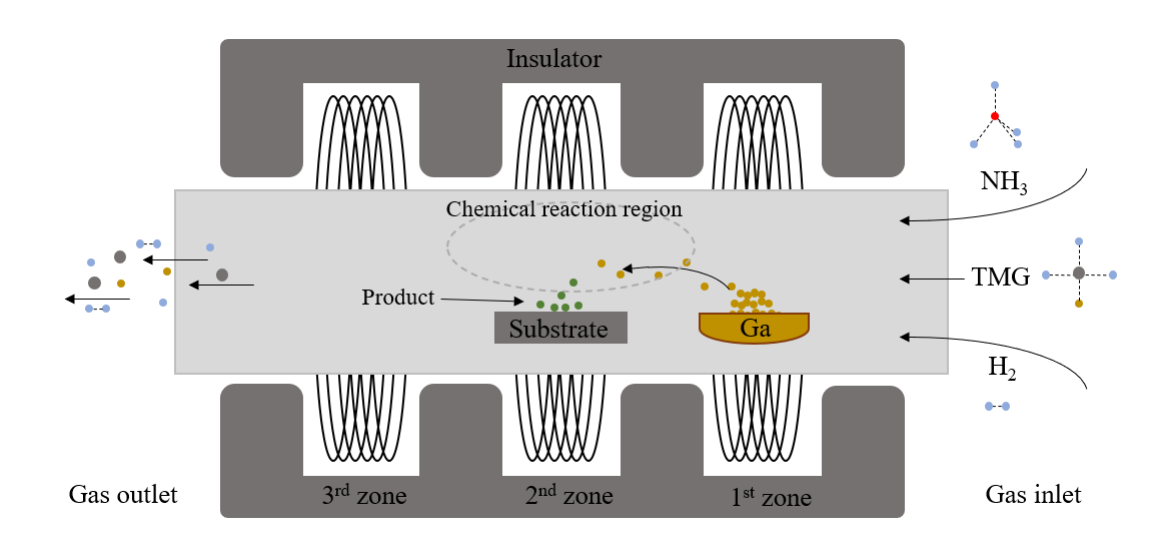


Figure 10: Scheme of a three-zone CVD instrument.

A standard CVD instrument arrangement is exemplified in Figure 10. A sample is placed inside the tube usually made of a quartz glass. The quartz tube is placed to an oven which can be divided into several heating zones which brings a benefit of separate regions with different temperatures. One side of the tube is connected to the inlet of gases and precursors, the opposite side of the tube is connected to the outlet (usually a rotary pump).

Before the deposition, the sample is heated up and several cycles of nitrogen rinsing is performed to clean the sample and the inside of the tube from the dust and other contaminants. Once the sample is clean and the temperature is set, the gases are introduced into the

tube. The molecular nitrogen N_2 and hydrogen H_2 are usually used as carrier gases which ensure both the constant flow of precursors through the tube which is established by the pressure gradient (from over-pressure inlet tube to under-pressure rotary pump outlet) and the uniform flow of precursors.

After the constant flow is established, the precursors line is opened. Precursors are either in the form of pure gases or in the form of mixture with carrier gas (usually molecular nitrogen). In this case, the carrier gas goes through a bubbler in where the nitrogen "bubbles" through the liquefied precursor. Once the precursors enter the quartz tube the thermal decomposition of them is initiated and the products of this decomposition chemically react. Eventually, the desired product is formed on the surface in form which is given by a flow rate of gases, a substrate temperature and precursors used while the side products of the chemical reaction are carried away from the tube.

Versatility of CVD for the fabrication of different kinds of materials is one of the great advantage of this method. Diamond coating could serve as one example. Low expansion coefficient, chemical inertness and wide optical transparency make a diamond a suitable material for optical, tribological and thermal management applications or wear-resistance coating [80, 81]. Significant role of CVD can be also find in the chip production [82]. Besides the film formation, CVD can also be utilized for fabrication of one dimensional materials such as nanowires [83]. III-nitrides [56, 84], ZnO [85] or SiC [86] nanowires are only few examples of versatility of CVD. CVD also enables production of graphene on large scale [87] which allows the mass production of this tremendous material.

Despite many benefits, CVD also suffers from several drawbacks. The volatility (very often even explosiveness) and toxicity of precursors require strict conditions of use. In addition, the temperature gradients inside the quartz tube and random chemical reactions can influence desired structures. However, the fine tuning of the system helps overcome much of these drawbacks and allows to fully accommodate all benefits of CVD.

4.4 Physical properties of gallium nitride

Gallium nitride can be found in two stable crystalline forms at ambient conditions - zincblend (cubic) and wurtzite (hexagonal) as shown in Figure 11 (a). While the cubic form is determined by ABCABC stacking sequence of (111) close packed layers, the wurtzite structure is characterized by ABABAB stacking sequence of close packed (0001) planes. Since most of the efforts is placed into the growth of the wurtzite structures, the further description will also focus on this structural form of GaN.

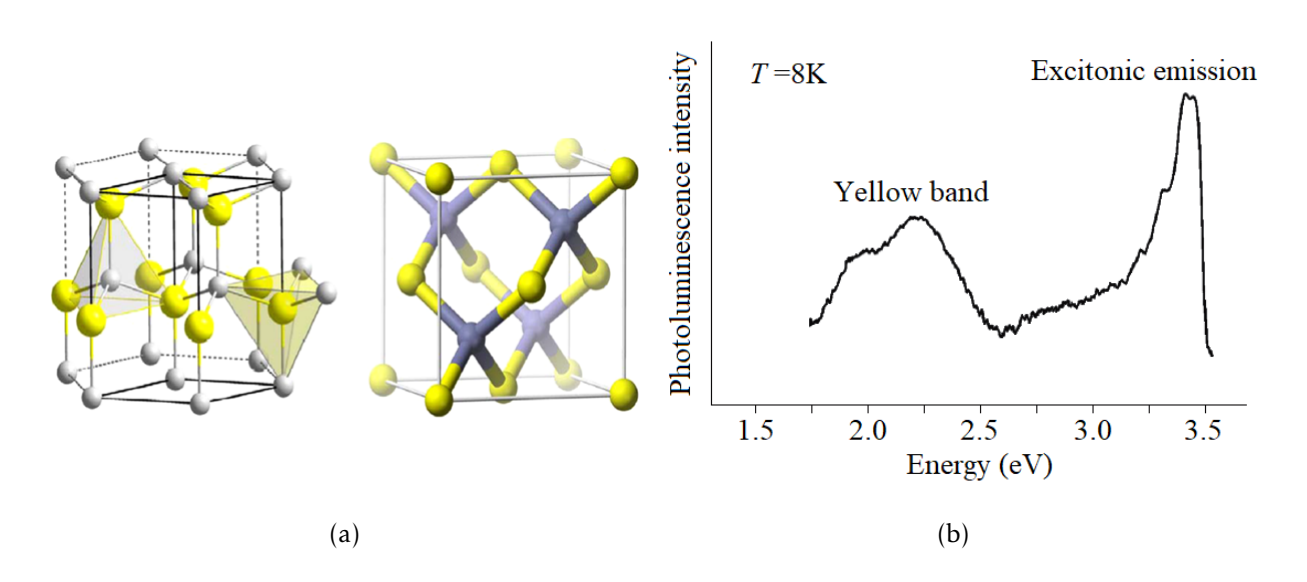


Figure 11: (a) Hexagonal wurtzite and cubic zincblende structures of GaN nitride [88]. (b) Photoluminescence response of GaN to $\lambda = 325 \,\text{nm}$ wavelength [89].

Wurtzite structure of GaN is defined by an a-axis lattice parameter $a=3.18\,\text{Å}$ and a c-axis lattice parameter $c=5.19\,\text{Å}$ of a hexagonal prism [88]. Based on the surface termination the several reconstructions can be recognized. The c-axis projection on the surface normal in ([0001]) or ([0001]) directions defines polar +c-plane or -c-plane. The other widely used surface reconstructions are the non-polar ([1010]) m-plane, the non-polar ([1120]) a-plane and the semi-polar ([1012]) r-plane [90].

The surface polarity comes from the unequal electronegativity of nitrogen and gallium atoms. This inequality results in a formation of polar covalent bonds in between these two elements in where the orientation of polarization directs from nitrogen to gallium atoms. Therefore, the surface termination plays a major role in the polarity of a surface - a surface

terminated with gallium atoms ([0001] - G-face) has opposite polarity to a surface terminated with nitrogen atoms ($[000\bar{1}]$ - N-face). Despite the fact that the polarity has significant effect on various GaN characteristics it is still challenging to measure its orientation. Provided connection between piezoelectric direction and the sign of GaN polarity as well as the effect of polarity on surface reconstruction were not undoubtedly confirmed as discussed in [91]. Interestingly, the polarity is a bulk characteristic so, for example, a gallium layer deposited on GaN does not change the polarity. For that reason, the polarity also plays a decisive role in the crystallographic growth of epitaxial layers or heterostructures resulting in preferential faces on which the growth of appropriate devices is possible (e.g. FET heterostructure should be grown on Ga-face to reduce the effect of induced strain).

GaN is also extensively studied for its optical properties. The band-gap energy of $E_{\rm b}=3.42\,{\rm eV}$ at 300 K corresponds with the wavelength of $\lambda=362\,{\rm nm}$. The overview of the band-gap energy measurement at various temperatures can be found in [92]. The photoluminescence spectrum is illustrated in Figure 11 (b). The photoluminescence response of the n-type GaN was extensively studied because of the presence of a broad peak covering yellow (2.2 eV) and green (2.4 eV) band of the electromagnetic spectrum. The origin of yellow and green luminescence is still an open question. Early work based on the first principle calculation suggests an idea that deep acceptors levels induced by gallium vacancies are responsible for this yellow luminescence response [93]. The following experiments with two excitations energy - above and below the band-gap - are in agreement with this argument suggesting that the yellow luminescence is attributed to the defects near the surface while the deep bulk defects contribute to the green luminescence [94].

The electrical properties of GaN are strongly influenced by intentional, but also unintentional, doping. At the room temperature the electron mobility of GaN reaches $\mu_e = 900\,\mathrm{cm^2\cdot V^{-1}\cdot s^{-1}}$ at charge carriers concentration of $n=4\times 10^{16}\,\mathrm{cm^{-3}}$ [96]. At the temperature of liquid nitrogen the electron mobility can reach $\mu_e=1\,500\,\mathrm{cm^2\cdot V^{-1}\cdot s^{-1}}$ (charge carrier concentration $n=8\times 10^{15}\,\mathrm{cm^{-3}}$) [92]. However, those values can be significantly changed during the growth process when remnants of atomic hydrogen diffuse into the material and react with the dangling or defect bonds. In addition, when GaN is p-type doped with Mg (which is the element of choice for p-doping because its low ionization energy), the hydrogen can form neutral centers with Mg resulting in decreasing conductivity. Hydrogen

	$E_{\rm G}\left({\rm eV}\right)$	λ (nm)	a (Å)	$E_{\rm b}(10^6\cdot{\rm V\cdot cm^{-1}})$	$\mu_{\rm e}({\rm cm}^2\cdot{\rm V}^{-1}\cdot{\rm s}^{-1})$	$c_{\tau} \left(\mathbf{W} \cdot \mathbf{cm}^{-1} \right)$	Ref.
InN	0.64	1900	3.53	0.35	2050	0.8	[95, 96]
Si	1.1	1127	5.43	0.3	1400	1.5	[97]
4H-SiC	3.26	380	3.08	3	900	4.9	[43, 97]
GaN	3.42	362	3.19	5	900	1.3	[96]
AlN	6.14	200	3.11	11	300	2.9	[96]

Table 1: Electrical and optical characteristics of chosen semiconductors (sorted by increasing band-gap energy). Energy band-gap at the room temperature E_G (eV), corresponding wavelength λ (nm), lattice constant a(Å), breakdown voltage E_b (10⁶ · V · cm⁻¹), electron mobility μ_e (cm² · V⁻¹ · s⁻¹), thermal conductivity c_τ (W · cm⁻¹).

also interacts (i.e. passivates acceptor centers) with other p-dopants such as zinc or calcium as elucidated in [92]. However, this behavior can be used in producing high resistivity GaN using a light-ion implantation in which process the electron and hole traps are created. On the contrary, the elements such as oxygen or residual silicon cause residual n-doping of GaN. It is also worth mentioning that nitrogen vacancies probably do not contribute to the n-type conductivity of GaN since their high formation energy prevent them to occur at high concentrations [98]. Since all these elements are present in various concentrations during MOCVD, there is still place for a fine tuning in the growth process.

In Table 1, the most prominent binary semiconductors are listed and compared to silicon. As was mentioned above, the different applications put demands on different properties. It can be favourable to combine benefits of several materials in heterostructures. For instance, mature and low-cost production of Si wafers can be combined with the specific electrical properties of wide band-gap GaN for high power applications as described in Section 2.1.2. However, the 16% mismatch between Si and GaN lattices and different thermal conduction coefficients can result in creation of cracks in the vicinity of the Si / GaN interface during the growth process (especially during the cooling phase) which influences the critical thickness of formed GaN layer. In addition, an aggressive environment of hydrogen and oxygen radicals during the MOCVD growth process can initiate chemical reactions of a silicon substrate with the environmental atmosphere resulting in etching of silicon [89]. The effect of doping by residual gasses has been already discussed. These drawbacks were partially overcame by developing of new strategies such as growing of a buffer layer at first or introducing differ-

4 PHYSICAL PHENOMENA BEHIND THE GROWTH OF GALLIUM NITRIDE

ent growth techniques. However, the complexity of the heterostructures growth process is still high and a number of unintentional circumstances might occur during the preparation of the new and advanced nanostructures.

5 GaN nanocrystals on graphene

Gallium nitride (GaN) is a well-established material widely used in industry as is demonstrated by the GaN power technology roadmap [99]. GaN based functional devices such as light emitting diodes, high electron mobility transistors or ultraviolet detectors were already discussed in Section 2.1. Since GaN based devices impact the technology to such an extent, the need of a large scale production at a sufficient quality level has been increasing for the last couple of years.

The most common technique for the large scale production of gallium nitride is a chemical vapour deposition (CVD) and its modification. Dissociations of chemical precursors at high temperatures leads to a formation of an uniform layer of gallium nitride of variable thickness as described in Section 4.3.

Another widely used technique for the growth of GaN is a molecular beam epitaxy (MBE). This technique takes an advantage from the long history of its use. The MBE technique has been involved in the research of LED diodes from the very beginning. Thus, it is very well established and all the parameters which can affect the GaN growth are known. Historically, the MBE growth process of GaN uses a Knudsen type of an effusion cell as an atomic gallium source and a radio-frequency plasma source as a source of nitrogen (usually the plasma source provides the combination of atomic and radical nitrogen). Alternatively, decomposition of nitrogen precursors such as ammonia (NH $_3$) can be implemented into the growth process [100]. Both methods result in a formation of GaN thin films with considerably good quality represented by a decent electron mobility as high as $800\,\mathrm{cm}^2\cdot\mathrm{V}^{-1}\cdot\mathrm{s}^{-1}$ which is comparable with the best samples fabricated using MOCVD.

In addition to above mentioned, the alternative methods of GaN fabrication are being developed. One of them takes a benefit from introducing hyperthermal nitrogen ion beams. Hyperthermal refers to nitrogen ions with energy below 100 eV. It has been already demonstrated that an ion-beam-assisted MBE can enhance the GaN quality significantly [101]. Interestingly, it was found that there is a crucial difference between simultaneous deposition of gallium and nitrogen in one step and step-by-step multisequence deposition of the same elements as will be described below.

Simultaneous deposition of ionic nitrogen and metallic gallium leads to the formation of a thin film. One aspect influencing the formed thin film is the presence of either molecular nitrogen N_2^+ or atomic nitrogen N^+ . Another aspect is the ratio of ionic nitrogen and atomic gallium fluxes. In case of molecular nitrogen ions N_2^+ , the film thickness shows a linear trend with respect to the ions/atoms ratio in which the higher the gallium supply the thicker the film. If the atomic nitrogen ions N^+ are used, the film thickness follows a similar linear trend but the maximum thickness is approximately half of that one related to the film grown by molecular nitrogen N_2^+ . This suggests that the impact-induced dissociation of N_2^+ molecule is efficient enough to produce atomic nitrogen even for energy below $100 \, \text{eV}$ [102].

To give an example, a simultaneous deposition of hyperthermal nitrogen ions of the energy $E = 25 \,\text{eV}$ and gallium thermal atoms with the ions/atoms ratio of 2.7 at a temperature of $T = 750 \,^{\circ}\text{C}$ results in an epitaxially grown thin layer of wurtzite GaN (w-GaN) [103].

While the simultaneous deposition of gallium atoms and nitrogen ions (at an appropriate $Ga/N_2^+(N^+)$ ratio) results in a smooth layer of GaN, the deposition divided into (i) deposition of gallium and (ii) post-nitridation (referred as a sequential deposition) leads to a formation of GaN crystals [104, 105]. In this case, the hyperthermal nitrogen ions diffuse over the surface of a liquefied metallic Ga droplets into the region where the gallium droplet is in contact with the surface where the nucleation of GaN nanocrystals is initiated.

Sequential deposition brings a benefit of possibility to grow GaN selectively. Sites in which the gallium atoms initiate a formation of droplets can be effectively defined by, for instance, creating the surface features such as holes milled by a focused ion beam. An array of periodically arranged GaN nanocrystals can then serves as a functional matrix for a plasmonic applications [106]. On top of that, a sequential deposition process enables to cultivate GaN nanocrystals in their size. Thus, a well ordered array of GaN of an uniform morphology and size can be fabricated as demonstrated by our group [107].

Throughout the years, an appropriate substrate allowing the growth of high quality epitaxial gallium nitride has been a limiting factor. Silicon, the material number one in semiconductor industry, provides advantages of low cost and large wafer production. However, a

significant mismatch between corresponding crystal lattices hinders the possibility of production of large scale Si/GaN heterostructures. Other materials, such as sapphire, help overcome the issue with the lattice mismatch but high cost and low scalability of their production together with worse properties compared to silicon (e.g. heat conduction) remain bottlenecks in a mass production.

The usual way of increasing the quality of GaN on a silicon substrate is the application of a buffer layer. This layer, placed in between the silicon substrate and the GaN layer, acts as a bridge which absorbs cracks at the silicon/buffer layer interface and thus allows to grow high quality GaN. As an example, aluminium nitride with lattice constant comparable to GaN can be used as a buffer layer for the growth of high quality GaN [108]. In addition, formed AlN buffer layer acts as a barrier layer which prevents a direct interaction of Ga atoms with a pristine Si surface which, otherwise, leads to an etching of silicon.

Alternative materials can also be used for bridging the silicon and gallium nitride. Those materials can be two dimensional nanostructures, as for instance hexagonal boron nitride or graphene. An ultimate thickness of 2D materials circumvents the necessity of a considerably high thickness of the buffer layer and can also bring new properties which are characteristic for 2D materials. The possible application of 2D materials has already been demonstrated by using hexagonal boron nitride as a layer suitable for the growth of single crystal gallium nitride [109]. Similarly, an evidence for high quality gallium nitride grown on graphene has been provided as well [110].

Combining electrical properties of 2D materials and electrooptical properties of GaN paves the way for a fabrication of light sensitive devices. In this specific case, the sensitivity to UV radiation can be expected. Recently, such UV sensitive devices have been presented. GaN nanocrystals grown on Si(111) [111] and graphene/sapphire [112] substrates showed a sharp responsiveness to UV radiation. In both cases, however, a high temperature during the CVD process was used. The selectivity in the growth of GaN nanocrystals was, thus, limited due to the increased thermally induced surface diffusion. Using an alternative approach of droplet epitaxy can make this growth selectivity possible which could be a key factor for a modulation of a UV sensitive GaN device to a wide range of wavelengths.

5.1 Fabrication of GaN nanocrystals

Fabrication of gallium nitride nanocrystals is based on a growth process taking place in a deposition chamber of the vacuum system described in Section 4.1. The salient feature of this process lays in the fact that the deposition is divided into i) an evaporation of metallic gallium by using the effusion cell and ii) post nitridation of formed gallium droplets by using the nitrogen ion-beam source, which provides hyperthermal ($E \le 50\,\text{eV}$) nitrogen ions, both tools are described in Section 4.2.1. Such a process is known as the droplet epitaxy which was described in Section 4.2. The presence of nitrogen ions of the energy $E \le 50\,\text{eV}$ at a low substrate temperature (below 300°C) as well as the use of a graphene monolayer as a kind of a buffer layer between GaN and silicon dioxide makes this method unique to all referred literature.

The formation of GaN nanocrystals is a process sensitive to the deposition conditions. The substrate temperature, gallium droplet distribution or the number of deposition sequences are only the examples of phenomena associated with the fabrication process. Therefore, several experiments focusing on these aspects were performed before the GaN growth itself. Initially, the distribution of gallium droplets as a function of the substrate temperature was studied. Afterwards, the effect of the number of deposition sequences, i.e. the sequences of gallium deposition and post-nitridation, was evaluated. Once those experiments had been done, the GaN nanocrystals formation was studied with respect to the influence of substrate temperature and energy of nitrogen ions.

5.1.1 Sample preparation

Silicon wafer (n-type Si(100), $\rho = (0.577 - 0.601)\Omega \cdot \text{cm}$, ON Semiconductors) with a 285 nm thick thermally grown silicon dioxide layer was chosen as a substrate for the fabrication of GaN nanocrystals. The thickness of silicone dioxide is especially suitable for graphene-based devices for two reasons. Firstly, this particular thickness is well-known to "make graphene visible" even by optical methods because the combination of reflectivity of the SiO₂ layer and graphene results in a possibility of seeing the graphene by naked eye [113]. Secondly, 285 nm thick silicon dioxide layer is sufficient enough to act as an insulating layer which allows the measurement in a FET arrangement.

Graphene used in prepared samples was a commercial CVD product (Graphenea) with a declared electron mobility of $\mu=1\,500\,\mathrm{cm^2\cdot V^{-1}\cdot s^{-1}}$. As graphene was delivered on a copper foil, several steps had to be taken to transfer it to a silicon substrate. The standardized routine (developed in our group) consists of several steps:

- Coating of graphene on a copper foil with a 150nm layer of poly(methyl methacrylate)
 (PMMA A4 950) using a spin coating technique. PMMA provides a supportive layer for graphene transfer.
- Cutting the foil into pieces of a required size (typically $2 \times 2 \text{ mm}^2$).
- Rinsing sample pieces at $0.2 \, \text{mol}$ solution of ammonium persulfate $((NH_4)_2S_2O_8)$ for 2 hours. The solution dissolves the copper, so graphene stays attached to the PMMA layer.
- Rinsing in a deionized water. Remnants of the ammonium persulfate are dissolved in the water, so the chemical reaction is terminated.
- Rinsing the pieces in 5 % chlorine acid (HCl). HCl chemically reacts with the remnants of copper atoms ensuring graphene is free from copper contamination.
- Rinsing in deionized water. Remnants of HCl are dissolved in the water, so the chemical reaction is terminated.
- Transferring graphene onto prepared sample.
- Drying the sample at the ambient atmosphere at room temperature for at least 12 hours. The remaining water molecules trapped in between the graphene and the surface evaporate during this period of time.
- Rinsing in an acetone bath for 1 hour. After 1 hour the temperature of the acetone bath is raised up to 63°C for another 1 hour. Acetone dissolves the PMMA layer, so only the graphene layer stays attached to the surface.
- Rinsing in deionized water. Remnants of acetone are dissolved in the water, so the chemical reaction is terminated.

• Blowing the sample dry with nitrogen for 5 min.

The sample is then attached on a pyrolitical boron nitride (PBN) plate of the sample holder as can be seen in Figure 5 (b) and inserted into the vacuum system described in Section 4.1.

As the final step of the preparation procedure, the sample is heated up to 300°C in order to desorbed contaminants such as water or hydrocarbons from the surface. As mentioned in Section 4.1, the base pressure of the vacuum system is maintained below $p < 8.5 \times 10^{-8} \, \text{Pa}$. Once the sample is heated up the pressure typically rises to $p = 5 \times 10^{-6} \, \text{Pa}$ (this is caused by the desorption of the contaminants from the sample). The sample is kept at this temperature until the pressure falls back below $p = 1.2 \times 10^{-7} \, \text{Pa}$ at which moment the sample is considered to be clean and prepared for the GaN growth process.

5.1.2 Formation of Ga islands on graphene

As the first step, the distribution of gallium islands on graphene was studied. The preparation of the substrates followed the routine described in Section 5.1.1. The deposition of gallium took place in the complex vacuum system described in Section 4.1 using the gallium effusion cell described in Section 4.2.1.

The deposition time of gallium was set to 50 minutes. During that period of time, 4.3×10^{16} atoms per cm² impacted the surface which is equivalent to 10 monolayers. The effect of the substrate temperature on the distribution and size of gallium islands formed on graphene can be seen in Figure 12. At a temperature of 150° C (Figure 12 (a)), gallium forms small islands with diameter below 20 nm and average density about $200 \,\mu\text{m}^{-2}$. Interestingly, some islands are brighter than the others. As a temperature rises to 200° C (Figure 12 (b)), the brighter islands grow in size, while the darker islands tend to coalescence into larger clusters. The situation changes at the temperature of 250° C (Figure 12 (c)). While the size of the brighter islands is saturated, the darker islands further coalescence into larger islands. As a temperature continues to grow to 300° C (Figure 12 (d)), the darker islands become more prominent. At a temperature of 350° C (Figure 12 (e)), both bright islands as well as dark islands are slightly larger but no significant difference can be observed. The

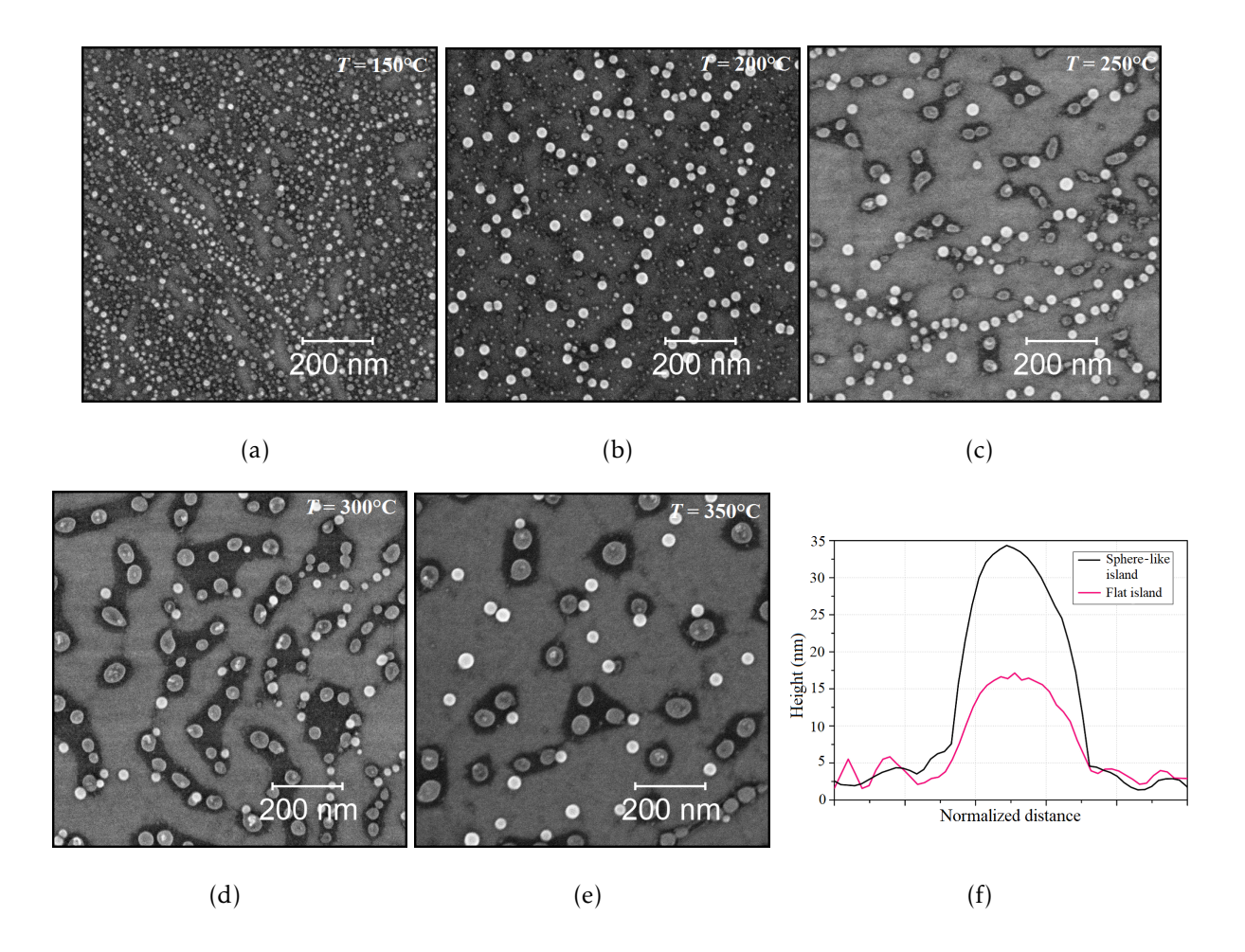


Figure 12: SEM images of gallium islands formed on graphene at (a) 150° C, (b) 200° C, (c) 250° C, (d) 300° C and (e) 350° C. (f)An AFM profile of gallium islands on graphene at 350° C. The diameters of islands were normalized in order to show the difference in height. The SEM images were taken by a FEI Verios 460L microscope at a landing energy of E = 8 keV and probe current of I = 25 pA. AFM images were taken by an ICON Brucker microscope using the ScanAssyst mode and probe.

combination of bright islands and dark islands seems to be stable until the substrate temperature is so high that Ga atoms are desorbed from the surface which is approximately above 500°C. Figure 12 (f) shows the AFM profiles of the islands grown at 350°C. Here, the difference between the bright and dark islands is clearly visible. While the bright islands are more hemispherical, the dark islands appear to have flat tops. The difference in the intensity (bright/dark) is most likely caused by their different height and thus distinct secondary electron yields.

The effect of temperature on the distribution and size of gallium islands is clearly visible from the plots in Figure 13. The distribution and size analysis was done using an ImageJ

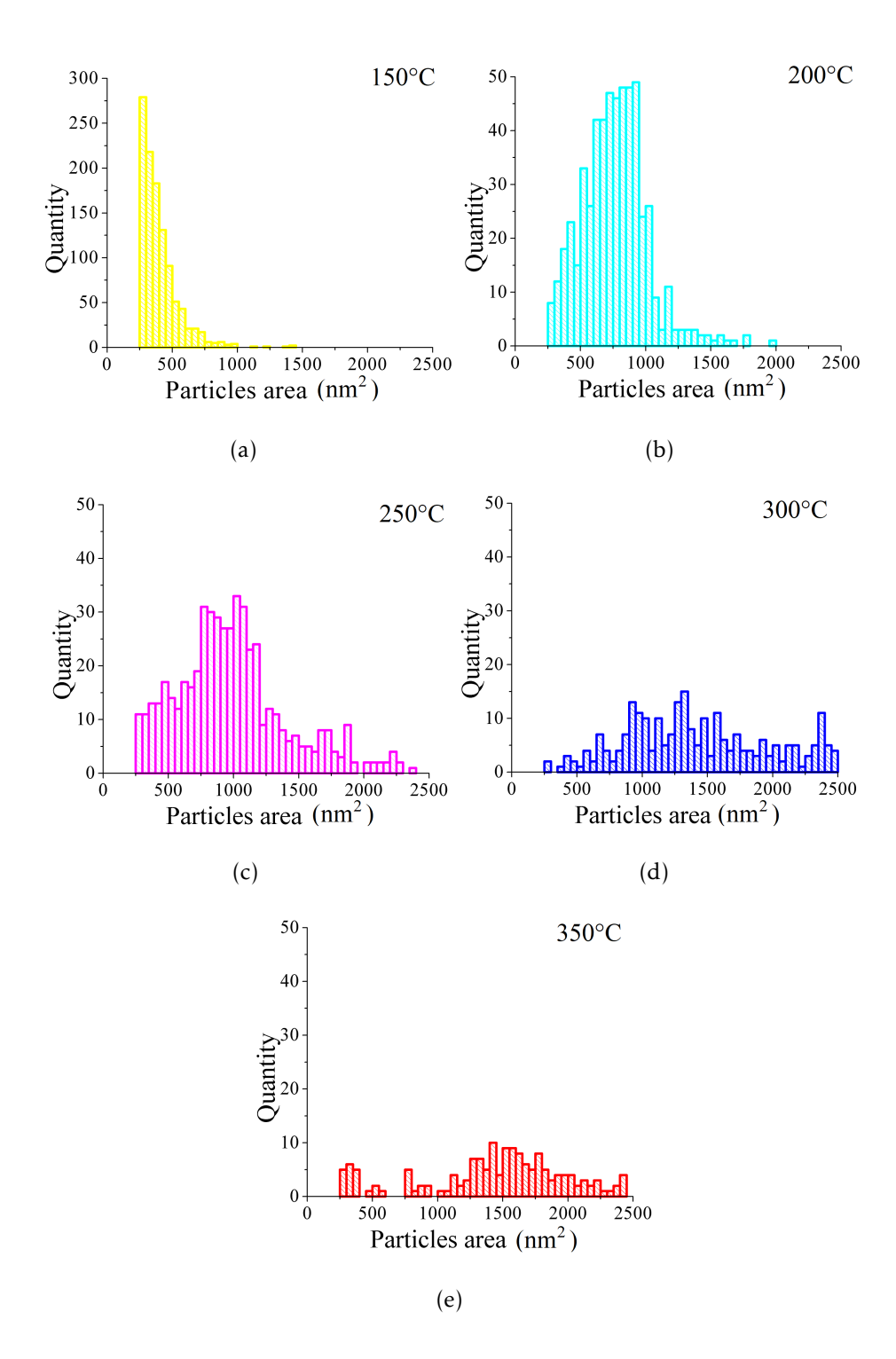


Figure 13: Distribution of Ga islands projected area at temperature of (a) 150°C, (b) 200°C, (c) 250°C, (d) 300°C and (e) 350°C. The area was defined as a top-down projection of the islands.

software in which the particle analysis with the watershed thresholding was applied to the SEM images. The applied method provides a particles (islands) projected area distribution. In general, the most critical point of any particle analysis is a proper setting of particle segmentation algorithm. In order to ensure proper selection of particles of interest, the

particle areas below 250 nm² (which corresponds to particle diameter below 15 nm) were excluded from the dataset. The area distribution obviously follows trend in SEM images. At a temperature of 150°C (Figure 13 (a)), islands with the area below 500 nm² are dominant. As the temperature rises, the area distribution peak maximum moves to bigger areas and distribution curve becomes flat. Interestingly, the diameter of the different islands (bright sphere-like islands and dark flat islands) can be estimated based on these plots. At a temperature of 200°C the bright islands seem to be the largest particles in the corresponding SEM image (Figure 13 (b)). In addition, the area of those bright islands seem to be constant with increasing temperature (Figure 13 (c), Figure 13 (d)). Therefore, it can be estimated that the area of bright sphere-like islands vary from 750 nm² to 1000 nm² which corresponds to the diameter ranging from 25 to 35 nm. Considering the SEM image of Ga grown at 350°C (Figure 13 (e)) in which the dark flat islands are dominant with corresponding particle area distribution 1500 nm² to 2500 nm², it can be estimated that the diameter of dark flat islands varies between 45 and 50 nm.

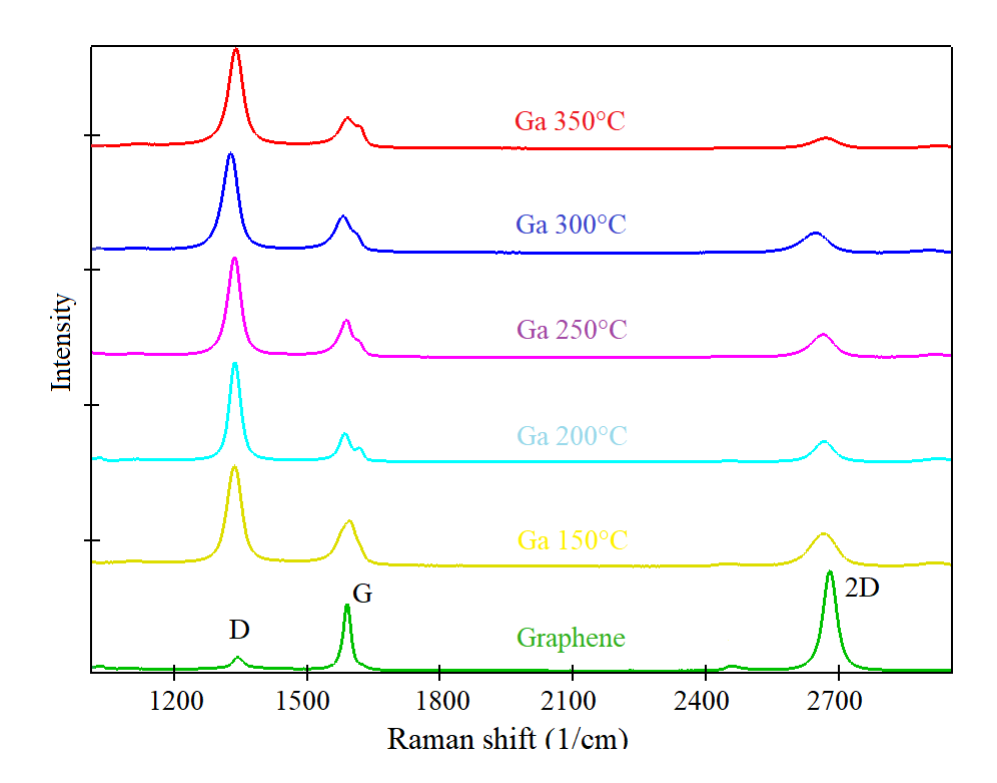


Figure 14: Raman spectra of graphene samples with Ga atoms deposited at various substrate temperatures compared to the Raman spectrum of pure graphene. The spectra were taken by a Witec Raman system using a 532 nm excitation laser.

Gallium atoms impinging on a graphene sheath can possibly influenced its quality. There-

fore, the graphene quality before and after the deposition of gallium at various temperatures was also investigated. The corresponding Raman spectra are plotted in Figure 14. The spectrum of pure graphene (green line) reveals the D, G and 2D at the positions of $1350\,\mathrm{cm^{-1}}$, $1580\,\mathrm{cm^{-1}}$, and $2690\,\mathrm{cm^{-1}}$, respectively, which is in agreement with referred literature [114]. The mutual ratio of D, G and 2D peaks suggest a considerably good quality of graphene. The Raman spectra taken after the deposition of gallium at various temperatures indicate the disorder of graphene after the deposition of gallium. An increased intensity of the "defect" D peak and a reduced G and 2D peak intensities are reliable indicators of deterioration of graphene quality. On top of that, the splitting of the G peak into G+D' peaks suggests additional changes in the graphene crystal structure caused by an applied stress [115]. Similar behaviour was already observed during oxygen plasma etching of graphene singlecrystals in [116]. These findings lead to a conclusion that deposition of Ga affects the graphene layer quality but the graphene layer itself is still preserved.

5.1.3 Formation of GaN nanocrystals on graphene

Once the graphene was covered with gallium droplets, the second phase of the growth process - nitridation - was initiated. The substrate temperature was either kept at the same temperature as in the case of deposition of gallium or reduced to the specific temperature. In both cases, a 30-minute gap between terminating the gallium deposition and initiating the nitridation was kept in order to let gallium droplets stabilize. After that time, the chamber was filled with the nitrogen gas (partial pressure $\approx 5.5 \times 10^{-5} \, \mathrm{Pa}$) and nitridation was initiated.

Growth of nanocrystals was conducted at various deposition conditions in order to evaluate the effect of the substrate temperature, time of individual deposition steps and the number of steps in a deposition sequence on the morphology and topography of formed nanocrystals.

SEM images in Figure 15 demonstrate how the number of deposition sequences at a given temperature (in here $T=280^{\circ}\text{C}$) affects both the distribution and size of formed nanocrystals. In the case of one deposition sequence GaN forms nanocrystals with the area peak maximum around $600\,\text{nm}^2$ which corresponds to a diameter of $28\,\text{nm}$. For two sequences, the area peak maximum shifts to a value of $1\,000\,\text{nm}^2$ which corresponds to a diameter of $35\,\text{nm}$, but the distribution is broader. Finally, three sequences leads to a more uniform distribution over an area of $(800-1\,600)\,\text{nm}^2$ which corresponds to the diameters ranging from $30\,\text{nm}$ to $45\,\text{nm}$. In addition, a significant number of particles with a diameter below $25\,\text{nm}$ can be observed, which are probably the seeds of nanocrystals created in the previous sequence. Based on these findings we can speculate on two conclusions. Firstly, the formation of nanocrystals is limited by the amount of the delivered building material - the more deposition sequences, the higher the amount of the material. Secondly, the process of crystallization requires a certain time - the more deposition sequences, the longer time for crystallization.

Therefore, the further experiments were carried out by applying the following deposition strategy - 50 min of Ga deposition followed by 1 hour of nitridiation performed in three cycles with 20 min space between each step. The size of formed nanocrystals is heavily dependent on the substrate temperature as can be seen in Figure 16. The size of the

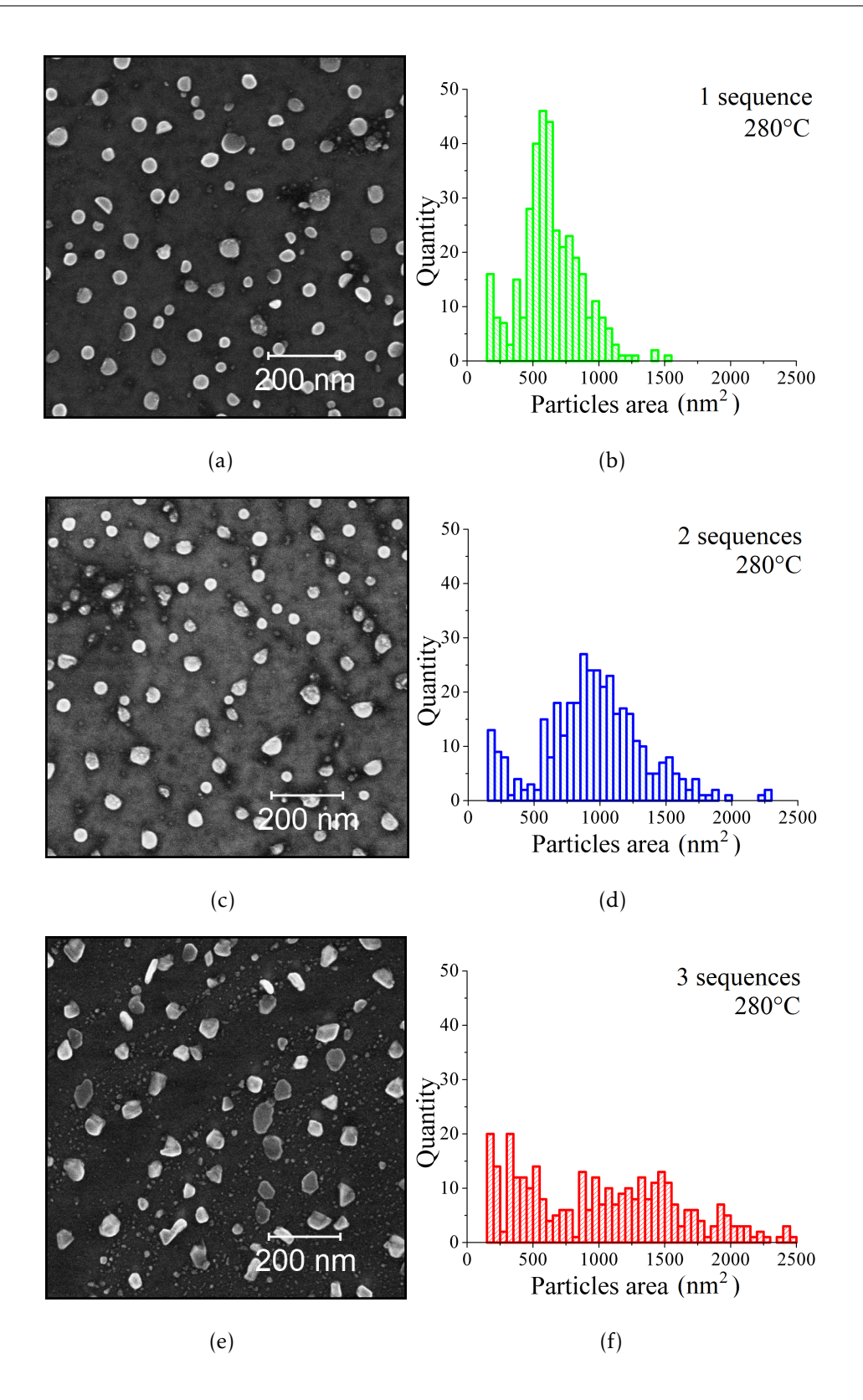


Figure 15: SEM images of formed nanocrystals on graphene during (a) one sequence, (c) two sequences and (e) three sequences. (b, d, f) Corresponding particle area distributions. The SEM images were taken by an FEI Verios 460L microscope at a landing energy of $E = 8 \,\text{keV}$ and a probe current of $I = 25 \,\text{pA}$.

nanocrystals grown at a temperature of 240°C (Figure 16 (a)) is in the range of (20 - 30) nm. As the substrate temperature increases, the nanocrystals grow in size which can be up to 100 nm at 280°C and higher. The shape of nanocrystals is random even though the faceted sides are clearly visible. In comparison with the nanocrystals grown on a SiO_2 surface and observed in [107], there is no significant difference in their shape.

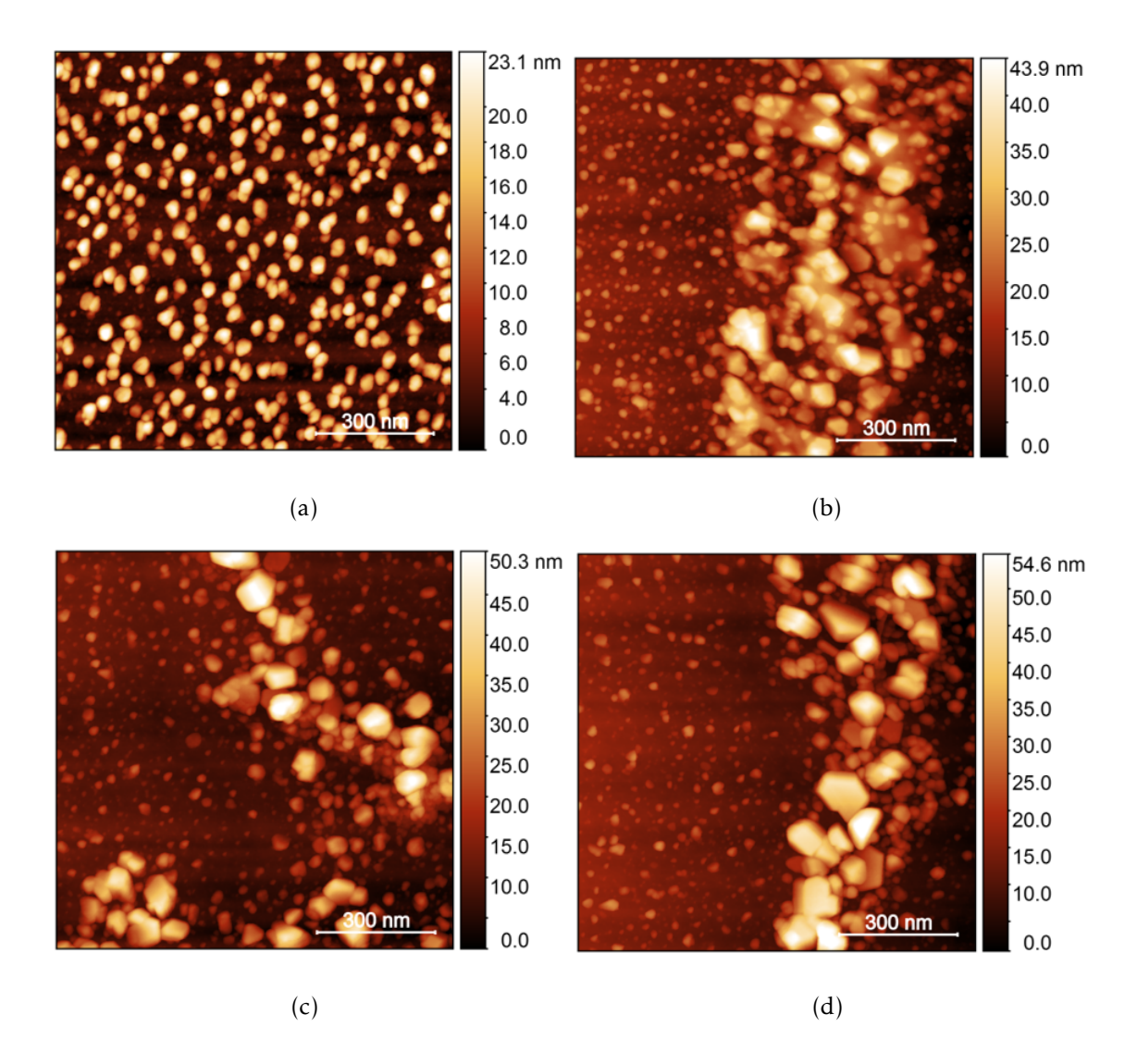


Figure 16: AFM images of nanocrystals formed on graphene at (a) 240°C, (b) 260°C, (c) 280°C and (d) 300°C. AFM images were taken by an ICON Brucker microscope using the ScanAssyst mode and probe.

Despite the fact that the quality of nanocrystals seems to be sufficiently high, the quality of the graphene layer suffers from the atoms/ions irradiation. Figure 17 (a) shows the Raman spectra of a graphene layer after one (green line), two (blue line) and three (red line) deposition sequences. In all three cases, the absence of the 2D peak and presence of the

D peak brings a sufficient evidence that graphene layer quality is significantly affected and goes down with the number of sequences. In our experimental arrangement, the resistance of a graphene monolayer placed on SiO_2 was typically around 900Ω . The formation of nanocrystals on graphene (graphene exposed to Ga atoms and nitrogen ions) increased the resistance up to $15\,000\,\Omega$ which was a significant obstacle for the measurement of electrical properties.

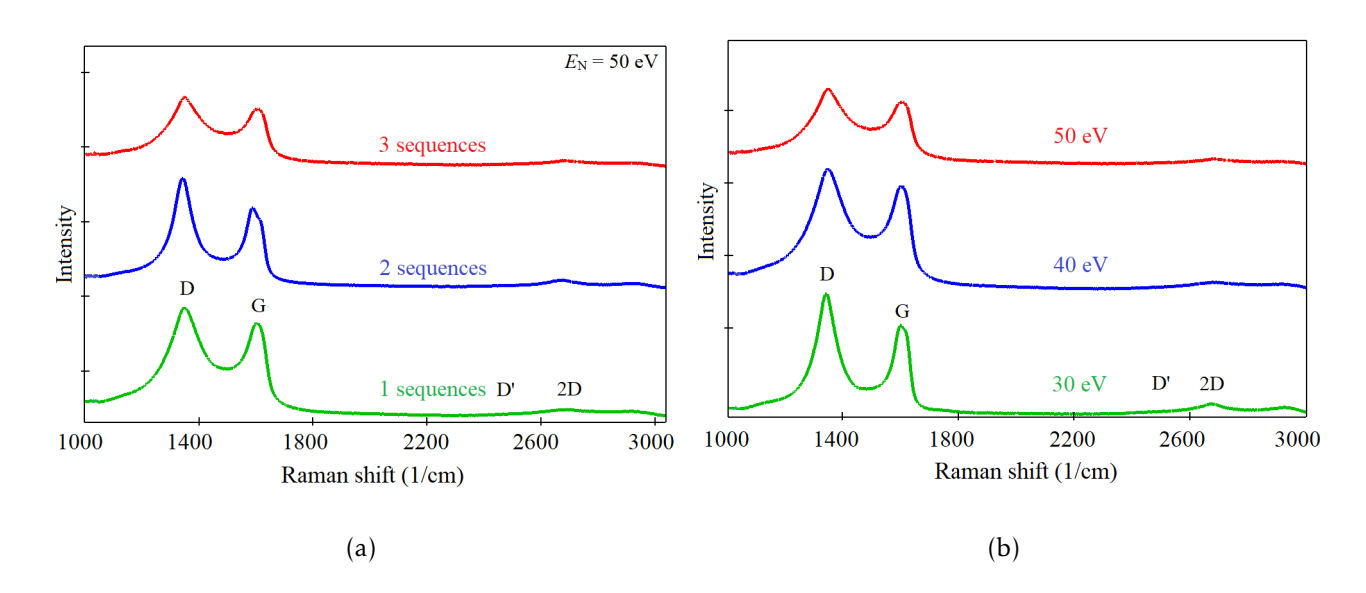


Figure 17: (a) Raman spectra of graphene with nanocrystals on grown using a different number of deposition sequences. (b) Raman spectra of graphene illustrating the effect of used nitrogen ions energy on the quality of the graphene layer. The Raman spectra were measured by a Witec Raman system using lambda = 532 nm excitation laser.

In order to circumvent this issue, the effect of energy of nitrogen ions during the growth was also studied. Figure 17 (b) indicates the quality of the graphene layer after a synthesis of nanocrystals using an energy of 50 eV (red line), 40 eV (blue line) and 30 eV (green line). Increasing energy of nitrogen ions results in decreasing the quality of the graphene layer. Although at the lowest energy (30 eV), the D and G peaks are clearly split, the 2D peak is very small. Hence, one can see that the reduction of nitrogen ion beam energy represents only a limited way how to preserve the graphene layer at a reasonably high quality.

The photoluminescence response of GaN nanocrystals to a UV excitation laser ($\lambda = 325\,\text{nm}$) is plotted in Figure 18. The comparison of nanocrystals grown using different nitrogen ion energy reveals several aspects. The blue emission peak corresponding to the inner

electron transition in GaN is located at 3.33 eV, 3.41 eV and 3.42 eV for ions energies 50 eV, 40 eV and 30 eV, respectively, as sum up in Table 2. The maximum of the yellow peak which corresponds to the deep acceptor level in GaN as discussed in Section 4.4 is positioned at 2.23 eV, 2.30 eV and 2.32 eV for 50 eV, 40 eV and 30 eV, respectively. Photoluminescence measurement legitimates us to claim that grown nanocrystals are GaN nanocrystals. Interestingly, the full-width-at-half maximum (FWHM) parameter of the yellow peak is equal for all three photoluminescence peaks. However, the same parameter differs in case of the blue peak. In overall, it can be seen that the photoluminescence response for 30 and 40 eV is identical and these are in a very good agreement with literature. In contrary, the response of the 50 eV GaN nanocrystals is slightly shifted towards lower energies by approximately 0.1 eV with the narrower blue emission peak.

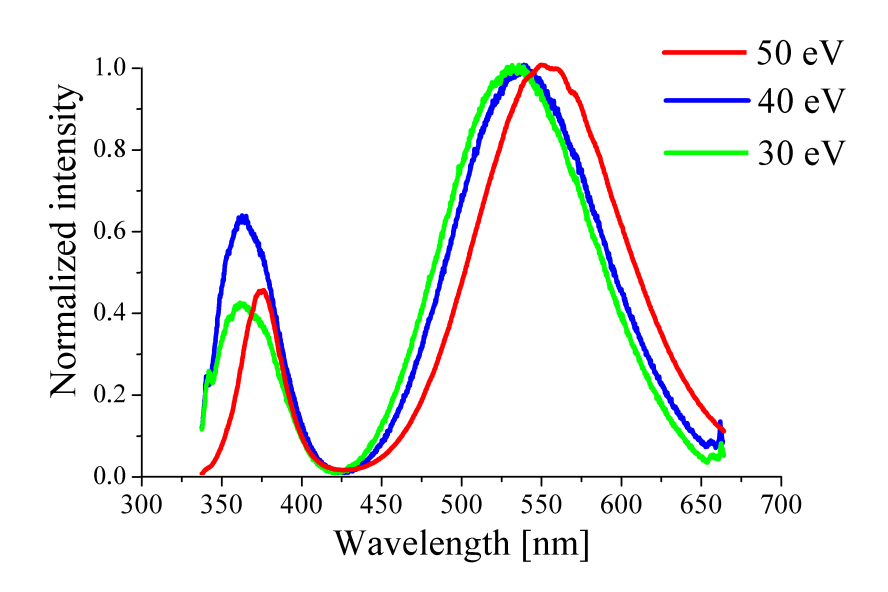


Figure 18: Photoluminiscence spectra of GaN nanocrystals grown at different nitrogen ion beam energies. The spectra were taken by a NT-MDT Ntegra Spectra Raman system using a 325 nm excitationlaser.

The shape of yellow peak between 450 nm and 650 nm is often observed in GaN photo-luminescence response if impurities incorporated in a crystal lattice of formed GaN crystals are presented as was already mentioned. By fitting of three Gaussian sub-band-gap emission peaks at 475 nm (2.29 eV), 510 nm (2.43 eV) and 540 nm (2.61 eV) the authors in [117] identified three donor-acceptors recombinations which can be attributed to two phenomena. First, the emission peak at 475 nm (2.29 eV) can be associated with a diffusion of silicon atoms from the substrate into the GaN crystal lattice causing a lattice distortion which can

result in enhanced n-type doping behaviour. Second, the peak at the longer wavelengths can be attributed to shallow donors - deep acceptors transition, in where the shallow donors are associated with substitutional atoms such as oxygen, silicon or carbon while the deep acceptors are linked to gallium vacancies [98].

$E_{\rm ions}$ (eV)	$\lambda_{\mathrm{BL}}(\mathrm{nm})$	$E_{\mathrm{BL}}(\mathrm{eV})$	FWHM _{BL} (nm)	$\lambda_{\mathrm{YL}}(\mathrm{nm})$	$E_{\mathrm{YL}}(\mathrm{eV})$	FWHM _{YL} (nm)
50	372	3.33	27	555	2.23	107
40	364	3.41	42	538	2.30	106
30	362	3.42	48	533	2.32	108

Table 2: Photoluminescence characteristics. $E_{\rm ions}$ is the energy of nitrogen ions. $\lambda_{\rm BL}$ is the wavelength of the blue photoluminescence. $E_{\rm BL}$ is the energy of blue photoluminescence. $FWHM_{\rm BL}$ is the full width at half maximum of the blue photoluminescence peak. $\lambda_{\rm YL}$ is the wavelength of the yellow photoluminescence. $E_{\rm YL}$ is the energy of yellow photoluminescence. $FWHM_{\rm YL}$ is the full width at half maximum of the yellow photoluminescence peak.

The above mentioned results are in a good agreement with the former experimental work of our group [107] as well as with the theoretical description of GaN nanocrystal formation provided in [118]. Based on new findings together with theoretical description the growth of GaN nanocrystals can be generalized as follows. The formation of GaN nanocrystals is a result of interactions of nitrogen ions with the gallium atoms from the gallium droplet. The crystallization starts at the solid-liquid interface, i.e. in the close proximity of a liquefied Ga droplet and a solid substrate interface. There are several paths through which nitrogen ions can diffuse to this region - (i) entering the gallium droplet and diffusing through the liquefied volume, (ii) diffusing along the droplet surface or (iii) diffusing over the substrate surface as described by Gerlach [118].

Even though there is also a concentration gradient of nitrogen ions between a vapor-liquid interface and a liquid-solid interface, the low solubility of nitrogen in a liquid gallium droplet obstructs this diffusion path since the nitrogen diffusion coefficient in the Ga droplet is smaller than $10^{-5} \, \mathrm{cm}^2 \cdot \mathrm{s}^{-1}$. The mass transport along the droplet interface can be several orders of magnitude higher compared to the diffusion through the liquid Ga. The convex shape of the droplet surface provides considerably more bonds which result in a prominent diffusion of nitrogen ions along this interface represented by the surface current.

The diffusion coefficient in this particular case varies from 1×10^{-4} to 1×10^{1} cm²·s⁻¹. The diffusion path along the vapor-solid interface also has to be taken into consideration since the diffusion coefficient of nitrogen ions on the surface is generally high [118].

In addition to the above mentioned diffusion paths, the sputtering of Ga atoms by nitrogen ions steps into the process as well. However, the landing energy of nitrogen ions in the 30 - 50 eV interval can be still considered as a soft-landing process. Considering that the simulating sputtering yields at temperature above 500°C are less than 0.05 atoms per ion and that with decreasing temperatures the sputtering yield is even smaller [118], this effect can be neglected.

5.2 Fabrication of an UV sensitive photodetector

Fabrication and characterization of GaN nanocrystals grown on graphene opened a way for the implementation of these nanostructures into a functional device. Motivation behind this application is combining two research directions in our group - GaN nanocrystals and graphene. During the work on this project a similar effort had been presented [111, 112]. In their papers, the authors demonstrated CVD grown GaN nanocrystals on the graphene layer placed in between two electrodes. Exposing this device to a UV light resulted in an increase of photocurrent between two electrodes.

In the following text, the proof of principle of a similar UV sensitive photodetector is presented. The droplet epitaxy at low temperature as described in Section 5.1.3 has been involved to fabricate the GaN nanocrystals on the graphene layer. These GaN nanocrystals act as active elements responding to the UV light.

Figure 19 (a) shows a schematic representation of the UV sensitive device design. The silicon with a 280 nm thick silicon dioxide layer is used as a substrate. There are two electrodes on the substrate surface made of gold which are separated by a $100\,\mu\text{m}$ gap. The area of the gap is covered with a graphene sheet in such a way that graphene is in an ohmic contact with both electrodes. The graphene sheet is covered with the gallium nitride nanocrystals which behave as UV sensitive structures. The electrodes are connected to a lock-in amplifier providing a voltage supply. Once the gallium nitride nanocrystals are exposed to an UV light, they provide charge carriers to graphene and thus changes in graphen electrical resistance are detected. A detailed description of the fabrication process of presented UV sensitive device and subsequent testing of its behaviour is provided in the following sections.

5.2.1 Fabrication of electrodes

Fabrication of an UV sensitive photosensor consists of several steps. First, gold electrodes are fabricated on the surface of a silicon substrate. Second, graphene is transferred onto the prepared structures. Third, GaN nanocrystals are synthesized in a UHV deposition chamber. Fourth, the prepared sample is attached onto ceramic expander which is then connected to a circuit designed for electrical measurements. The individual activities are summarized in detail in the following overview:

- Coating of a silicon wafer (n-type Si(100), $\rho = (0.577 0.601)\Omega \cdot \text{cm}$, ON Semiconductors) with a 1.4 μ m thick layer of an AR-P 3540 negative resist.
- Performing optical lithography by an UV Direct Write Laser system (HEIDELBERG DWL 66-fs).
- Dissolving the irradiated negative resist in a solution of developer AR 300-47 and deionized water in 1:1 ratio.
- Rinsing in deionized water in order to terminate chemical reactions.
- Deposition of a 3 nm thin layer of titanium which serves as an adhesive layer followed by a 100 nm thick layer of gold from which the electrodes are made of. This process was performed in an UHV deposition chamber using a Kauffman type of the ion beam source.
- Dissolving the rest of the resist by acetone in an ultrasonic bath.
- Plasma cleaning of the sample substrate.
- Rinsing the sample in isopropylalcohol and deionized water in order to terminate the chemical reactions and rinse away possible remnants of the resist.
- Transferring graphene onto the prepared samples as described in Section 5.1.1.
- Deposition of GaN nanocrystals as described in Section 5.1.3. Three sequence deposition of gallium atoms and nitrogen ions of energy $E = 30 \,\text{eV}$ at a substrate temperature of 280°C .
- Attaching the prepared sample onto a ceramic expander using a conductive glue G302 (silver flakes dissolved in the methylizobuthylketon). The ceramic expanders contains silver contacts and allows heating the sample up to 500°C.

• Conductive connection of golden electrodes and silver contacts by $25 \,\mu m$ copper wires using a TPT HB 16 Wire bonder.

The photo of the UV photodetector attached to a sample holder with a PBN plate is shown in Figure 19 (b).

5.2.2 Experimental setup

The experimental setup for testing of the photodetector response to the UV light is depicted in Figure 19 (a). The prepared sample attached onto a ceramic expander is placed in front of an UV laser. The He-Cd laser produces monochromatic UV light of wavelength 325 nm. A mechanical shutter located at the far end of the laser instrument provides an easy way of selecting on/off operation state. The sample electrodes are connected to a Keithley/Lock-in measurement system developed in our group [119]. A voltage 1 V at a frequency of 1.333 kHz is set as an output value of a SR830 Lock-in amplifier (Stanford Research Systems). A signal goes to the first electrode on the sample through a $10\,\mathrm{M}\Omega$ resistor. The second electrode is then connected to the ground potential. The current flowing through graphene is then measured using a LabView software developed in our group. In addition to the basic circuit, the Keithley source provides gate voltage and thus allows measuring in a FET-like arrangement.

The FET-like arrangement is a possible way how to measure the carrier concentration inside the conductive graphene layer. The gold electrodes serve as a source and a drain in this arrangement. The silicon substrate isolated from the electrodes via the 285 nm thick silicon dioxide layer acts as a gate electrode. In the first approximation [120], described system can be simplified as a plate capacitor with capacitance

$$C = \epsilon_0 \epsilon_r \frac{S}{d} = \frac{Q}{U_g} = \frac{Ne}{U_g},\tag{8}$$

where $\epsilon_0 = 8.85 \times 10^{-12} \, \mathrm{F} \cdot \mathrm{m}^{-1}$ is the vacuum permitivity, $\epsilon_0 = 3.9 \, \mathrm{F} \cdot \mathrm{m}^{-1}$ is the relative permitivity for silicon dioxide, $S = l \times w = 100 \times 400 = 40\,000\,\mu\mathrm{m}^2$ is the effective area between two electrodes, $d = 285\,\mathrm{nm}$ is the thickness of isolating silicon dioxide layer, Q is the charge, U_{g} is the gate voltage between silicon substrate and electrodes, $e = 1.602 \times 10^{-19} \, \mathrm{C}$ is the elementary charge and N is the number of charge carriers. Considering the formulas for the

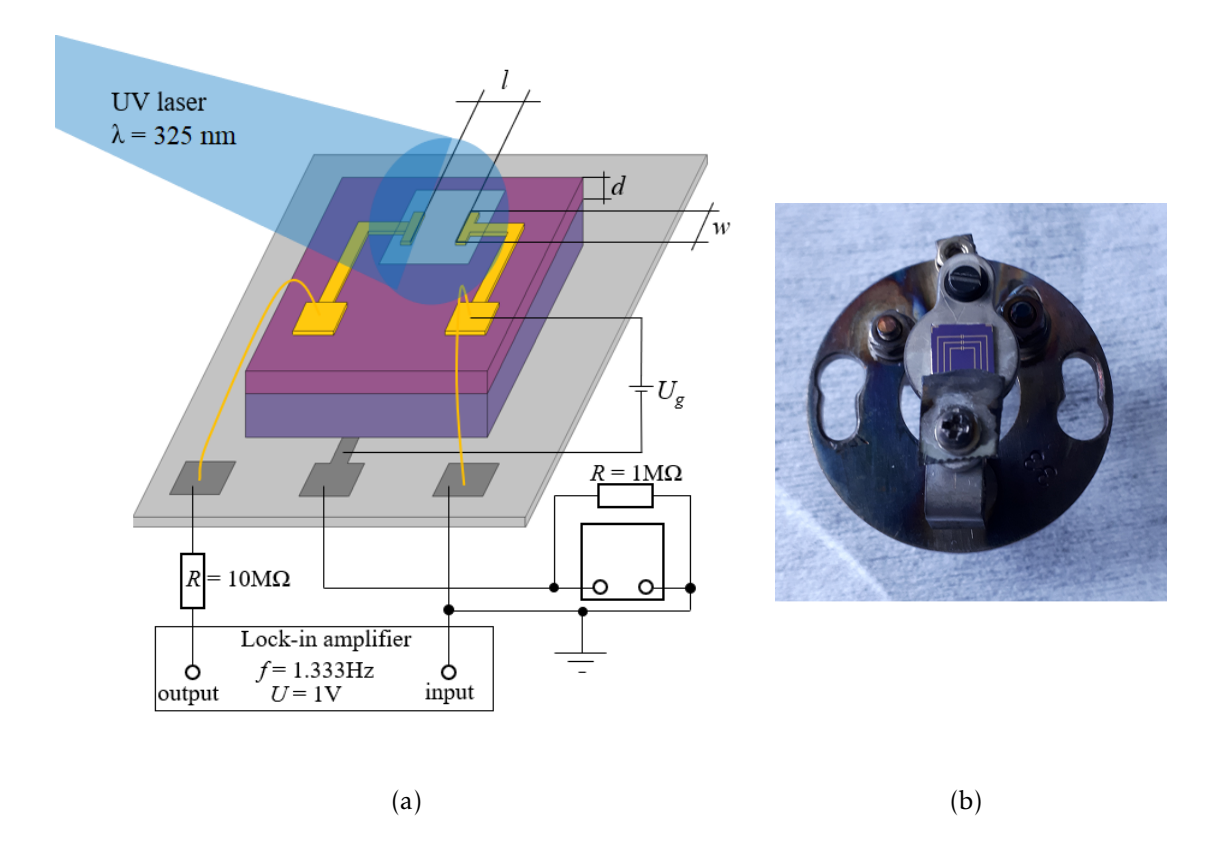


Figure 19: (a) Schematics of an experimental setup for detection of the response to the UV light with schematics of the electrical connection. (b) Photo of the UV photodetector attached to a sample holder with a PBN plate.

charge carrier concentration n = N/S and electrical conductivity $\sigma = ne\mu$, the charge carrier mobility μ can be determined from the linear dependence of the electrical conductivity on the gate voltage.

$$\sigma = \left(\frac{\epsilon_0 \epsilon_r}{d} \mu\right) U_g. \tag{9}$$

Obviously, the electrical conductivity can be expressed as $\sigma = 1/\rho = l/wR$, where ρ is the resistivity, l is the length of the channel (i.e. the distance between electrodes) and w is the width of the channel (i.e. the width of the electrodes). Thus, the charge carrier mobility μ can be calculated based on the measurement of the resistance R measured at a given gate voltage U_g .

5.2.3 Response to the UV light

The response of the UV sensitive photodetector to a UV light irradiation was measured using experimental setup described in previous Section 5.2.2 according to the arrangements in Figure 19 (a). The voltage applied to the gate was 30 V for all measurements.

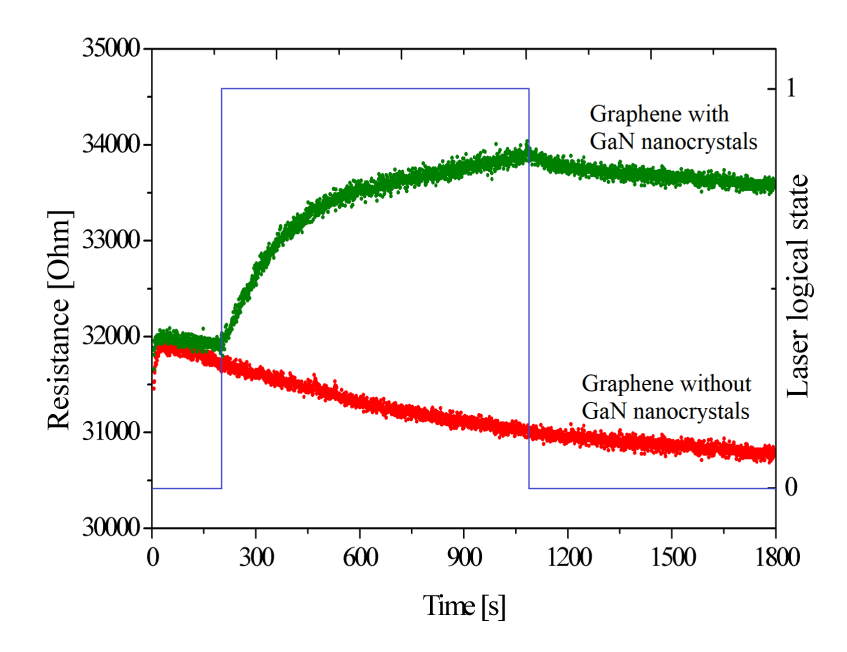


Figure 20: Response of the fabricated UV sensitive device to a UV light irradiation in the case of graphene covered with GaN nanocrystals (green line) and without them (red line).

Naturally, the first measurement was designed to compare the effect of irradiation of the graphene transducing layer with and without gallium nitride. As can be seen from Figure 20 the irradiation of graphene without GaN nanocrystals (red line) has no effect on the measured resistance. On the other hand, the experiment related to graphene with GaN nanocrystals exposed to the UV light shows an instant change in the measured resistance (green line). The resistance increases up to $34k\Omega$ compared to the initial value of $32k\Omega$ which provides a relative change of 8%.

It can be also seen from Figure 20 that the resistance is constantly going down when the UV light is off. This effect is still not fully understood and further experiments need to be performed to elucidate this phenomenon.

In the following experiments, the sample was irradiated with the UV laser for varying

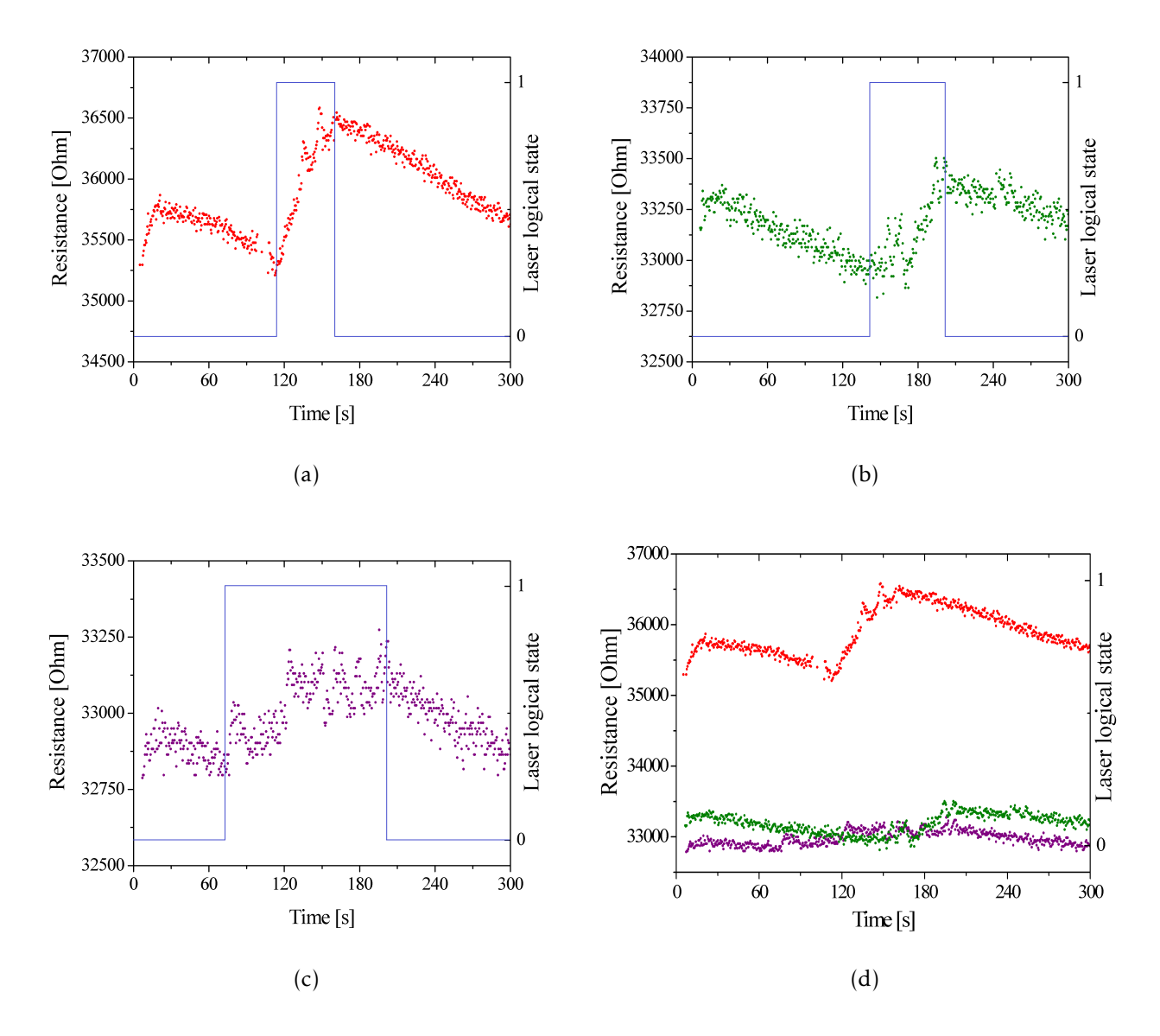


Figure 21: Response of the fabricated UV sensitive device to the irradiation with the UV light for (a) 40s, (b) 60s and (c) 120s. (d) Merge of plots (a)-(c) showing the decrease in resistance.

time interval. Figure 21 shows the measured response of the sample irradiated for (a) 40 s, (b) 60 s and (c) 120 s. In all cases, the instant change in resistance correlates with switching the laser on and off. In the first measurement, the rapid increase of resistance by $1\,000\,\Omega$ is observed. In the second measurement, the resistance increases roughly by $500\,\Omega$. The change in resistance in the third measurement is less dramatic when it increases by only $300\,\Omega$ despite the fact, that the irradiation lasted for $120\,\mathrm{s}$.

Figure 21 (d) reveals a direct comparison of these measurements on one sample. It can be clearly seen that the initial resistance decreases with each consecutive photodetector irradi-

Additionally, the amplitude of the response is also decreasing with the irradiation intervals. This could be attributed to a decrease in quality of either the graphene layer or gallium nitride crystals. However, the former case is unlikely since the irradiation of graphene without GaN nanocrystals provided strong evidence that the UV light has no visible effect on measured resistance. On the other hand, the latter case also seems very unlikely since GaN is in general a material stable and robust enough against external conditions and interactions.

The change in the resistance could be a consequence of increasing the temperature of the sample due to irradiation by the laser. However, this effect is probably low as the slope at which the resistance goes down before and after the irradiation is the same. If there was a temperature effect involved, the slope after laser switching off would be more rapid compared to that one before switching on since the temperature would decrease more rapidly.

Despite the fact that obtained results are not fully understood, the proof of concept experiment related to the UV photodetector has been successful. It has clearly confirmed that the GaN nanocrystals grown on the graphene layer at low temperatures provides a response of the UV photodetector to the UV light. This promising result paves the way to the new experimental field in our research group.

5.3 Conclusion

It has been demonstrated that the deposition of gallium atoms on a graphene layer placed on a silicon dioxide substrate results in a formation of two kinds of islands - sphere-like and flat ones. The size of these islands depends on the substrate temperature which as shown for the temperature range 150°C - 300°C. The diameter at a temperature of 300°C can reach 35 nm and 50 nm for the sphere-like and the flat islands, respectively. However, the quality of the graphene layer is affected by gallium atoms as was documented by the Raman spectra.

In the second part of this Section, it has been shown that the post-nitridation of gallium islands by hyperthermal nitrogen ions results in a formation of GaN nanocrystals. The size of the formed nanocrystals can be scaled up by the cultivation of these nanocrystals by the means of sequential deposition routine in which the gallium deposition and post-nitridation cycles are repeated for several times.

Cultivated GaN nanocrystals exhibits clear photoluminiscence response to the UV laser. There are two peaks present in the photoluminiscence spectrum - the blue peak at 362 nm and the yellow peak at 533 nm. The observed peaks are in line with the already published results [118] and in correspondence with the previous measurement of our group [107]. These findings further extend the potential of the droplet epitaxy method which can be beneficial for the production of GaN nanocrystals of various size and possibly in ordered structures.

The formation of GaN nanocrystals on graphene has then been implemented into an application which serves as a proof of concept of an UV sensitive photodetector. GaN nanocrystals were grown on a graphene sheet laid across Au electrodes. The whole device was then connected to the system for electrical measurements in the FET-like arrangement. After irradiation of the sample with UV light $\lambda = 325\,\mathrm{nm}$, the change in resistance of the layer was observed. Such a clear response to the UV light provides a significant opportunity for further research.

6 Two dimensional GaN

Discovery of graphene in 2004 [121] opened the door into a new scientific branch of two dimensional materials. Since that time, a number of articles dealing with calculation of stability of various forms of 2D materials has been published. Reviews summarizing possible 2D materials can be found in [122, 123].

While the prediction of hexagonal boron nitride (h-BN) led to its fabrication and following implementation into devices such as transistors, where acts, for instance, as a buffer layer for graphene because of its flatness and the similar lattice constant [124, 125], and other applications [126, 127, 128], the situation in other 2D III-nitride is not so matured. A stability of both 2D AlN [129, 130, 131] and GaN [129, 130, 132, 133, 134] has already been predicted based on numerical calculations.

Two dimensional III-nitrides semiconductors seem to be suitable for variety of applications due to their unique properties. Similarly to graphene, the doping of 2D GaN and AlN influences their properties. Doping by copper [135], transition-metals [136] and other elements [137] have shown change in the magneto-electrical properties resulting in enlarged spin polarization and increased Curie temperature. The opposite approach, i.e. creating vacancies in the 2D structures, plays an important role in changing electrical properties such as charge carrier mobility [138, 139]. These findings set the scene for implementation of 2D III-nitrides into spintronic applications in which the spin polarization brings a new degree of freedom.

Another direction of scientific interest tries to evaluate the feasibility of 2D III-nitrides for energy storage applications. Combination of these nanostrutures with an anode in Li-ion and Na-ion batteries increases the storage capacity of such device greatly [140]. Similarly, the viability of 2D AlN for hydrogen storage has been predicted recently [141]. The suitability of III-nitrides for high power electronics and transistors is also discussed in Section 2.1.2. As an additional example, the feasibility of III-nitrides for field-effect transistors heterostructures has been studied in [142, 143]. The calculation suggests that the III-nitrides could be helpful in overcoming the negative aspects of a short-length channel effects in modern FETs.

The deep ultra-violet optical applications in a water purification process such as a UV water treatment and a sanitation [144] or a toxic gases filtration [145] as well as optical applications spread over the visible spectrum [146, 147] also illustrate the versatility of III-nitrides. Even though, the predictions based on numerical calculations give promising results, the experimental evidences for these nanostructures are still rare.

The very first evidence of graphite-like hexagonal AlN laying on an Ag(111) substrate was reported by Tsipas et al. [148]. Even though STM characterization revealed an ordered hexagonal structure of 1.5 Å thin nanosheets, the dimensions below 20 nm put an obstacle to additional characterization. Another evidence of 2D AlN, in this case prepared on Si(111) [149] and sapphire [150] by an ammonia assisted molecular beam epitaxy, has been provided later but the authors have not brought any additional information but RHEED measurement.

Couple of years later, a new method of a migration-enhanced encapsulated growth (MEEG), in where the nanostructures grow encapsulated in between a substrate and graphene, has been introduced. This method was adopted for fabrication of two-dimensional gallium nitride [28] as well as two-dimensional aluminium nitride [151]. 2D GaN was grown sandwiched in between graphene and a silicon substrate passivated by hydrogen. Graphene is critical for stabilization of direct 5 eV GaN band-gap as authors proposed. MEEG method also allows to control the growth rate of 2D GaN structure resulting in the precise control of the number of formed layers. It has been shown that the number of layers is critical parameter in controlling the crystallographic structure which consequently defines the band-gap energy of the resultant GaN nanostructure [152]. Even though the MEEG method represents a strong technique for the growth of flat nanostructures, the measurement of electrical or optical characteristics is quite complicated as the graphene layer cannot be removed easily in this particular case.

Recently, researchers have brought a new light into this area by introducing a method for fabrication of micrometer-sized 2D GaN structures [153]. Heat induced decomposition of ammonia precursors and their subsequent reaction with liquefied gallium spread over tungsten foil led to a formation of an uniform 2D GaN layer. Measured characteristics of

a prepared functional device showed not only the promising electro-optical properties but also the possibility of transferring such nanostructures to an arbitrary substrate.

The presented theoretical as well as experimental works demonstrate the promising results related III-nitrides. At the same time they show that there is still a long way to the point in which these kinds of nanomaterials will be spread widely in the industry. Thus, the following sections aim to add a pinch of new knowledge into the pile of what-is-known about one of the 2D III-nitride - gallium nitride.

6.1 Sample preparation

The growth of the hexagonal gallium nitride was carried out on silicon Si(111) with two different miscuts which provided a varying surface terrace width. The process started with the substrate pretreatment which ensured the cleanliness of the surface. Then, a two-step growth process took place divided into (i) a deposition of gallium and (ii) a post-nitridation with low energy ions ($E = 50 \,\text{eV}$).

The substrates used for the growth of hexagonal GaN were n-doped silicon with native layer of silicon dioxide - Si (111) with the 4° miscut (resistivity $\rho = (0.029 - 0.030)\Omega \cdot \text{cm}$) and Si (111) with the 0.2° miscut (resistivity $\rho = (0.010 - 0.020)\Omega \cdot \text{cm}$). The substrates were pretreated before the growth itself in several steps in order to remove dust, carbon contaminants and the native oxide layer and to form reconstructed surface as listed:

- 1. Cutting the samples into $5 \times 17 \,\mathrm{mm}^2$ pieces from the 8" silicon wafer.
- 2. Sonication in an acetone bath for 5 min.
- 3. Sonication in an isopropylalcohol bath for 5 min.
- 4. Sonication in a deionized water bath for 5 min.
- 5. Blowing dry using nitrogen.
- 6. Inserting the samples into a vacuum chamber and heating them at 700 °C for 12 hours.
- 7. Exposing the samples to a temperature of 1250°C in short cycles for the overall time period equal to 1 min.

8. Cooling down to a deposition temperature.

The sonication in different chemical substances is suitable for removing dust and other contaminants soluble in alcohol. The heating of the samples is used in order to remove the carbon remnants and to decompose native oxide layer. The samples were attached to a sample manipulator before inserting to the vacuum system. The design of the sample manipulator allows a direct current heating at which the current flows directly through the sample which results in a rapid change of the substrate temperature. The direct heating technique is also suitable for high temperature routines since a PBN plate (used for an indirect sample heating as an alternative) cannot be exposed to the temperature above 900 °C. A temperature of 700 °C is high enough to the decompose native oxide layer but lower than the temperature causing formation of carbides from the organic carbon molecules which are adsorbed on the surface from the atmosphere. A flash-annealing routine is then carried out to induced reconstruction of the surface with minimal surface disorders. During the flash-annealing routine, the cycles of rising temperature are periodically repeated. At the beginning of each cycle, the temperature is kept at 1250°C for 5 seconds. Then the temperature is lowered down and the sample is kept at a temperature of 700 °C for 55 seconds. The cycle is then repeated for overall time of 12 minutes. After this time, the temperature is raised to 1250°C once again and then the sample is slowly cooled down to a deposition temperature (approximately 300°C).

6.2 Si (111) substrate with the 4° miscut

Growth of hexagonal GaN was carried out in a UHV complex system in the laboratories of the Institute of Physical Engineering at BUT. The UHV complex system as well as the gallium effusion cell and nitrogen ion-beam source were already described in Section 4.1 and 4.2.1, respectively. The growth routine consists of several steps:

- 1. Preparation of a substrate.
- 2. Deposition of gallium at various substrate temperatures.
- 3. Post-nitridation process using low energy nitrogen ions ($E = 50 \,\text{eV}$).

The preparation of n-type doped silicon Si (111) with the 4° miscut (resistivity $\rho = (0.029-0.030)\Omega \cdot \text{cm}$) followed the routine described in previous Section 6.1. In short, sonication in different chemical substances, degassing at a temperature of $T = 700^{\circ}\text{C}$ for 15 hours and the flash-annealing routine with a peak temperature of $T = 1250^{\circ}\text{C}$ for 12 cycles were performed to obtained clean surface with the 7x7 surface reconstruction.

After the preparation, the substrate temperature was decreased to T = 300 °C. On one hand the precise substrate temperature is critical for a formation of large gallium droplets (too low temperature results in formation of smaller droplets with higher surface density, while too high temperature leads to a desorption of gallium adatoms), on the other hand the interval in which temperature can be considered as optimal is quite broad (approximately from T = 270 °C to T = 330 °C). Setting the proper temperature was based on a previous experience with a deposition of pure gallium on pristine silicon in the UHV complex system.

Once the substrate temperature was stabilized, the deposition of gallium was initiated by opening an effusion cell shutter. The gallium effusion cell was handled to provided stable flux of gallium atoms of $f = 4 \times 10^{16} \, \mathrm{cm}^{-2} \cdot \mathrm{h}^{-1}$. The flux was measured by a Faraday cup before every deposition. After 1 hour the deposition was stopped and the sample was left for another 15 minutes at the same temperature to allow gallium adatoms diffuse over the surface and crate large droplets (mechanism of Oswald's ripening effect is described in Section 4.2.3 in detail). The deposition of gallium resulted in a formation of droplets with an average diameter of 50 nm. The density of gallium droplets was approximately 3×10^8 droplets per centimeter squared. After that the substrate temperature was decreased to the

values optimal for conducting the post-nitridation process.

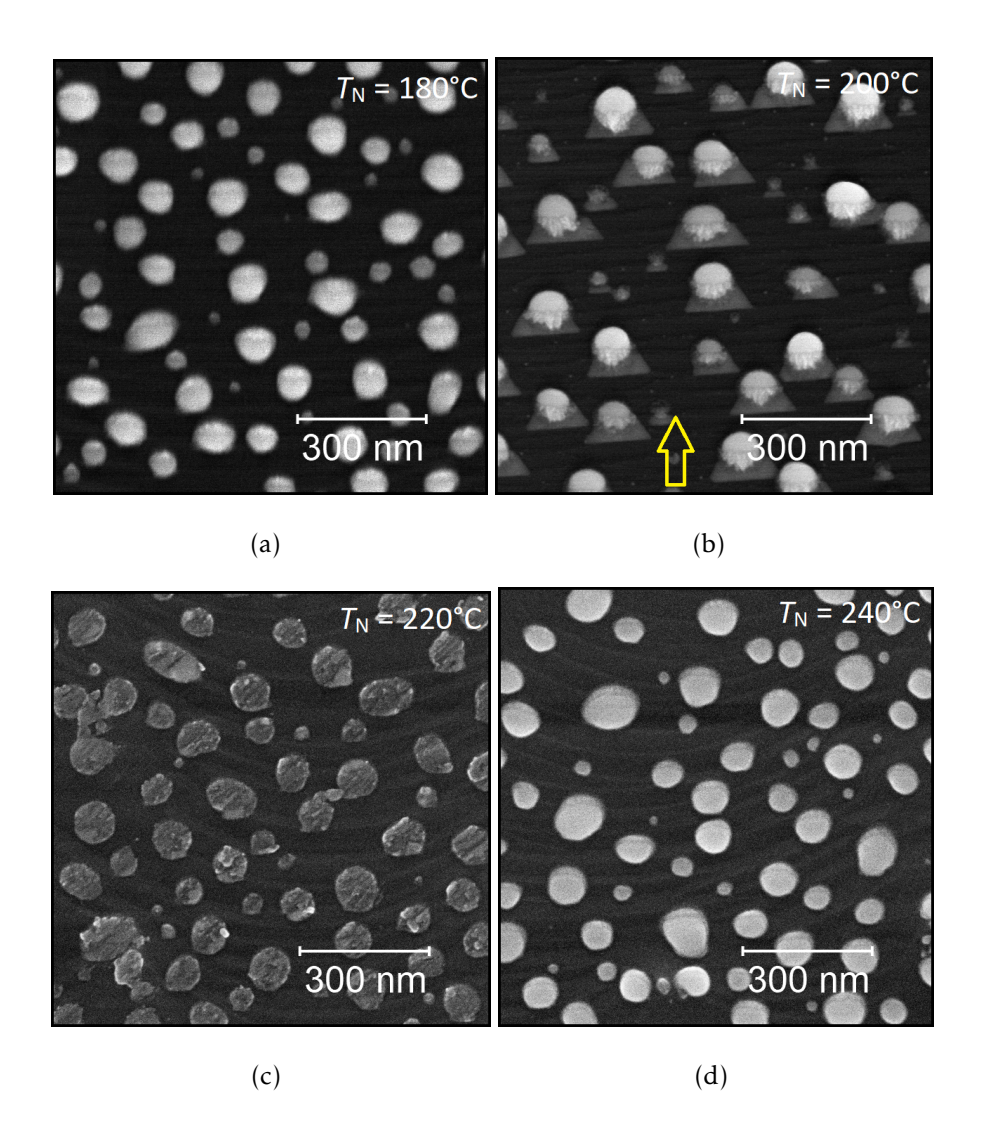


Figure 22: SEM images of GaN grown on pristine Si (111) illustrate the effect of the substrate temperature during post-nitridation. The deposition of gallium was carried out at the temperature $T = 290\,^{\circ}\text{C}$ for 1 hour. The subsequent post-nitridation was carried out for 2 hours at temperatures of (a) $T = 180\,^{\circ}\text{C}$, (b) $T = 200\,^{\circ}\text{C}$, (c) $T = 220\,^{\circ}\text{C}$ and (d) $T = 240\,^{\circ}\text{C}$. The yellow arrow indicates the direction of incoming ions. The SEM images were taken in a FEI Verios 460L microscope at landing energy of 8 kV and probe current of 25 pA.

Unlike in the case of deposition of gallium in which the deposition temperature interval is quite broad, the subsequent post-nitridation process has strict requirements on the substrate temperature. Figure 22 illustrates the effect of the substrate temperature during the post-nitridation procedure on the type of nanostructures grown. Before initiating the post-nitridation, the sample was kept at the set temperature for 15 minutes to stabilize possible

temperature fluctuations. Then, the UHV chamber was filled with the nitrogen up to a pressure of $p = 5.5 \times 10^{-5}$ Pa which provided a flux of nitrogen ions of $f_N = 2.24 \times 10^{16}$ cm⁻²·h⁻¹. The energy of nitrogen ions was set to E = 50 eV. The post-nitridation procedure was conducted for 2 hours.

The SEM images have revealed that the grown nanostructures were in the form of GaN droplets in the case that the temperature was $T = 180\,^{\circ}\text{C}$ and $T = 240\,^{\circ}\text{C}$ as can be clearly seen in Figure 22 (a) and (d), respectively. In contrary, the substrate temperatures of $T = 200\,^{\circ}\text{C}$ and $T = 220\,^{\circ}\text{C}$ led to a formation of more complex nanostructures as illustrated in Figure 22 (b) and (c), respectively. These nanostructures consists of remnants of the original gallium droplet, crystalline bulky GaN and crystalline triangle-like shaped GaN. Both the bulky GaN and triangle-like shaped GaN are formed from the side of the original Ga droplets facing towards the direction of incoming nitrogen ions. This finding suggests that incoming nitrogen ions interact with metallic gallium atoms of the droplet and this interaction (in the narrow temperature window) leads to a formation of additional features.

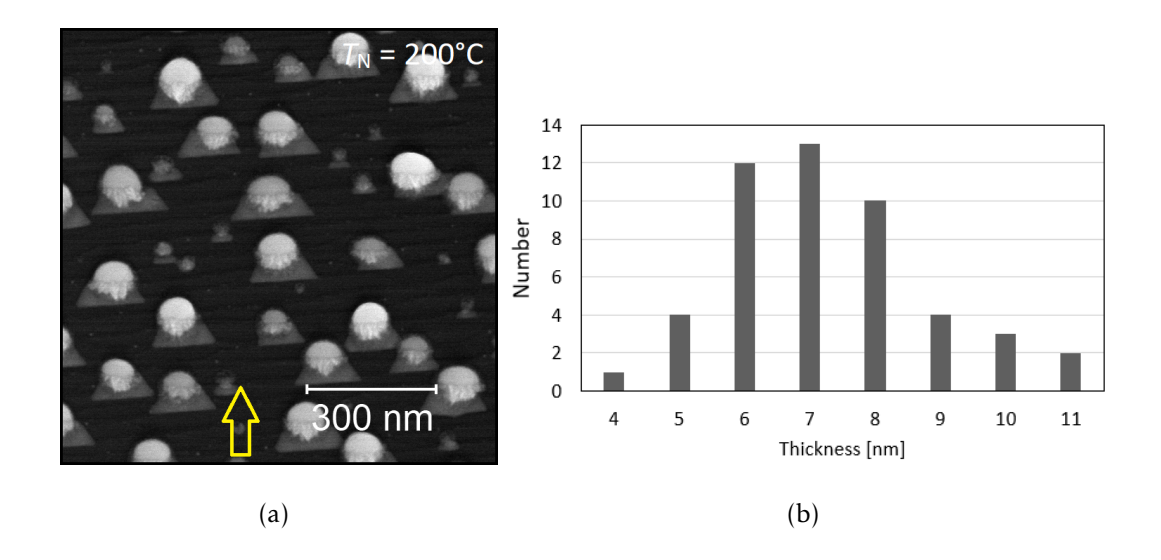


Figure 23: (a) SEM image of GaN triangle-like shaped structures grown on pristine Si (111) at T = 200 °C. The yellow arrow indicates the direction of incoming ions. (b) Thickness distribution of triangle-like shaped GaN nanostructures measured in AFM microscope (ICON Bruker).

As can be seen in Figure 23 (a) the size of triangle-like features is limited by the terraces of the silicon surface and controlled by the size of Ga droplets. More precisely, the terrace steps obstruct the further growth of the triangle-like features. Thus, the size of described

features is in the range of tens of nanometres at best. The thickness of triangular features was measured by AFM in a tapping mode. The obtained thickness distribution is plotted in Figure 23 (b). The thickness varies from 4 nm to 11 nm with the peak maximum at 7 nm.

In order to elucidate the crystalline structure of triangle-like features, a cross-sectional TEM lamella allowing the STEM imaging was prepared. Figure 24 reveals the cross-section of such a nanostructure. At first sight, a sharp interface between the silicon substrate and the formed nanoobject can be seen. The prepared nanostructures consists of the original metallic gallium droplet (the metallic gallium was most likely oxidized before the STEM measurement was done) and the crystalline GaN.

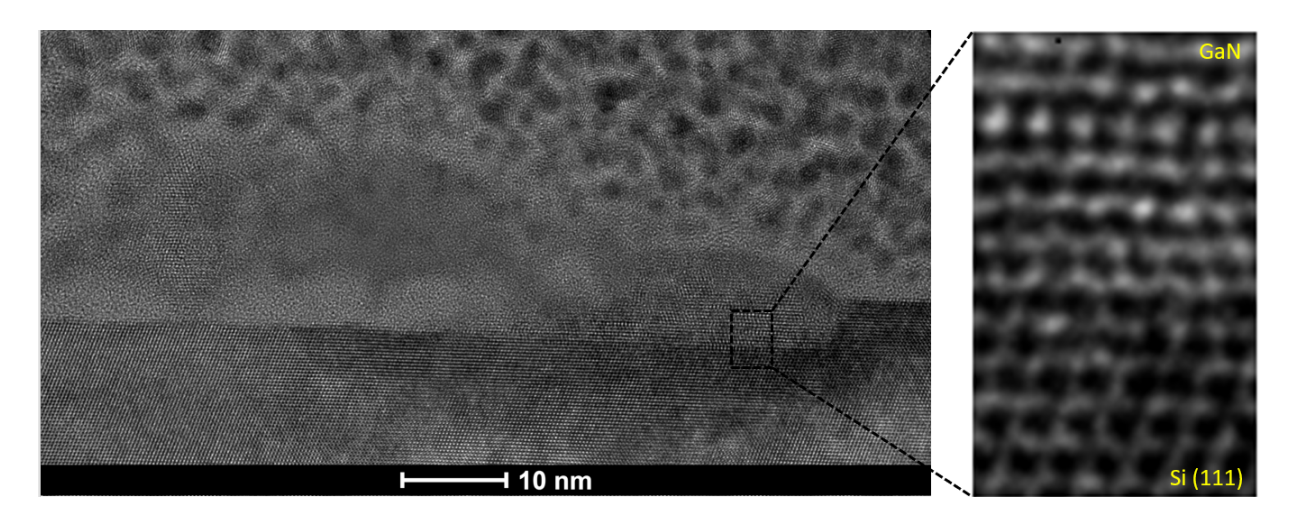


Figure 24: STEM image of the cross-sectional TEM lamella of an amorphous gallium droplet and crystalline GaN on a Si(111) substrate. The zoom-in STEM image of the Si(111) and hexagonal GaN interface.

The zoom-in part of the image shows several layers of the silicon Si (111) substrate and crystalline GaN in the close proximity of their interface. The measured interlayer distance of crystalline GaN was 3.14 Å. This value is higher than 2.59 Å observed in wurtzite bulk GaN [154, 155]. The interlayer distance of hexagonal two-dimensional GaN calculated by various numerical approaches varies from 2.22 Å [156] to 3.1 Å [133, 134, 157]. The variations in the interlayer distances of 2D GaN can be caused by the type of numerical calculation used but also because of the polarity of the Ga - N bond. Two nanosheets of GaN can be for instance layered in that way that nitrogen atoms of the first layer are above the gallium atoms of the second layer or the nanosheets can be mutually twisted which results in the change of

energy of interlayer bonds as predicted in [133]. Thus, a several stacking of hexagonal GaN appear to be stable at ambient conditions. Nevertheless, the measured interlayer distance seems to fit to the value calculated for 2D GaN.

The measured average lattice parameter $a = 3.28 \,\text{Å}$ is slightly higher than in a case of wurtzite GaN (3.18 Å) [154, 155, 158] but it is in a good agreement with the calculated value for hexagonal two-dimensional GaN [159] as well. These findings support our hypothesis that the observed triangle-like feature could be two-dimensional hexagonal gallium nitride.

The further characteristics were obstructed by the small dimensions of prepared structures. It can be clearly seen in Figure 24(a) that the surface step of the silicon substrate limits the growth of crystalline GaN. Therefore, a silicon substrate with larger surface terraces was chosen for additional experiments being described in the following Section 6.3 in which the silicon Si (111) with a miscut of 0.2° was used for preparation of the corresponding structures using the same growth method.

6.3 Si (111) substrate with the 0.2° miscut

The angle of miscut defines the size of terraces formed at the silicon surface. In this case, the miscut angle 0.2° provides larger terraces in the range of tens to hundreds nanometers depending on the quality of the flash-annealing routine. The GaN formation process is the same as was described in previous Section 6.2.

Initialy, the deposition of gallium was carried out. Preparation of the samples followed the routine described in Section 6.1. The base pressure after this routine was kept below $2 \times 10^{-7} \, \text{Pa}$. The optimal temperature of the substrate during the Ga deposition was set to $T = 300\,^{\circ}C$. The gallium effusion cell was handled to produce a flux rate of $f = 4 \times 10^{16} \, \text{cm}^{-2} \cdot \text{h}^{-1}$. After 1 hour of the gallium deposition, the substrate was covered by gallium droplets with a surface density of $n = 3 \times 10^8 \, \text{cm}^{-2}$ with an average diameter of 200 nm. The diameter and density were measured after exposing the sample to the atmosphere so the diameters of the droplets could be slightly modified. However, the average thickness (2-4 Å) of the native Ga oxide layer on the surface of pristine metals/semiconductors reported in [160] gives a strong argument that the oxide layer thickness is negligible with respect to the droplet diameter.

After the deposition of gallium, the substrate temperature was decreased. 15 minutes long interval between this reduction and initiating post-nitridation process ensured that the temperature was stabilized. After that time period, the chamber was filled with nitrogen atmosphere up to a pressure level of $p = 5.5 \times 10^{-5}$ Pa which provided the nitrogen ions flux of $f = 2.24 \times 10^{16}$ cm⁻²·h⁻¹. The energy of nitrogen ions was set to energy E = 50 eV. The post-nitridation was conducted for 2 hours. Similarly to the previous case described in Section 6.2, the substrate temperature during the post-nitridation process was critical as illustrated in Figure 25. At a temperature of T = 160°C (a) the droplets of Ga can be observed. As the temperature rises (T = 180°C (b)), the droplets begin to be deformed and a crystalline part of GaN protrudes in the direction of the surface projection of the incoming nitrogen flux. If the temperature is set to T = 200°C (c), GaN in the form of a layered triangular nanostructure is formed (detail description will be provided below). Once the temperature is increased above T = 220°C (d), the surface is covered by a mixture of layered triangle-like nanostructures and bulky chunks. In the following discussion, only the nanostructures grown at a temperature of T = 200°C (25 (c)) will be taken into consideration because they

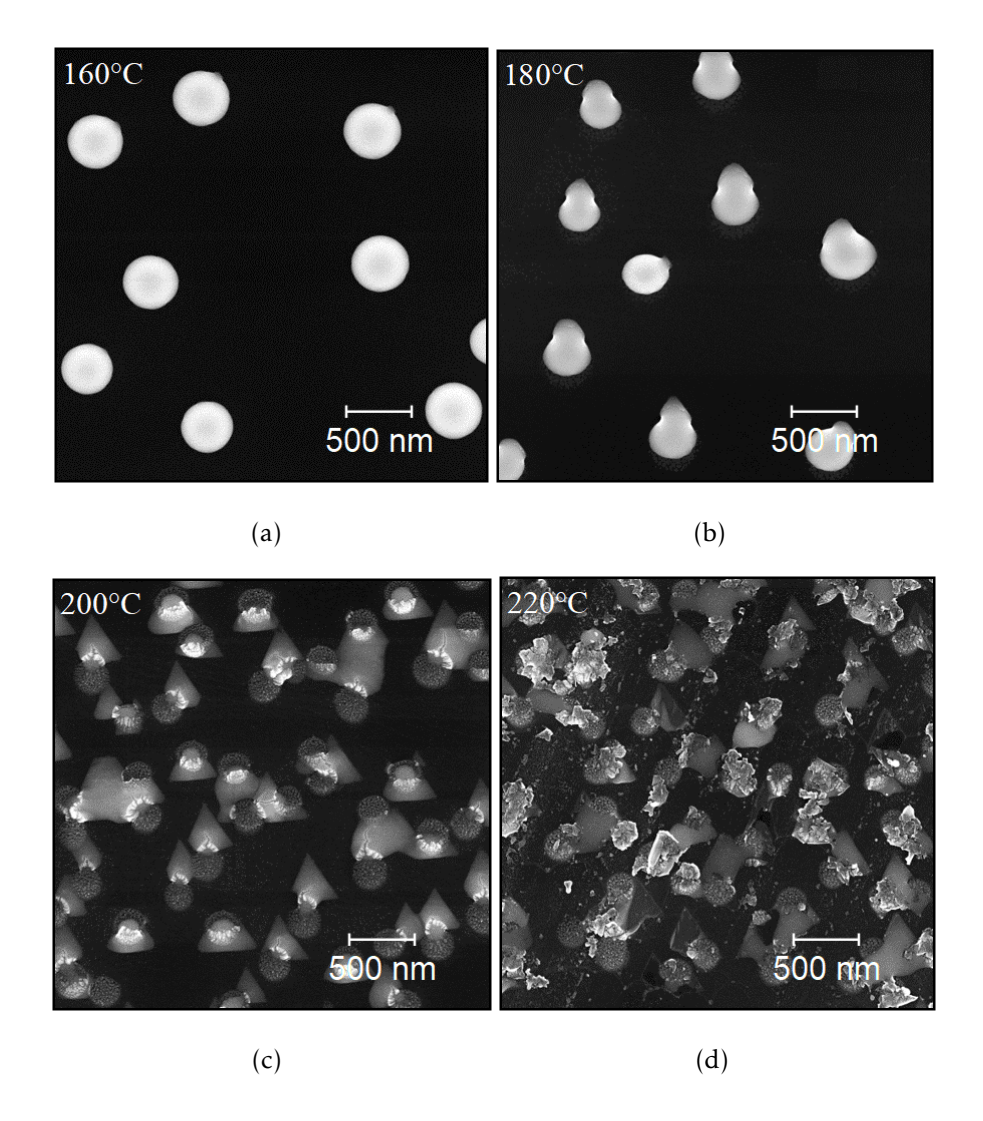


Figure 25: SEM images illustrating the effect of the substrate temperature during post-nitridation of GaN. The deposition of gallium was carried out at a substrate temperature of T = 290 °C for 1 hour. The subsequent post-nitridation was carried out for 2 hours at temperatures of (a) T = 160 °C, (b) T = 180 °C, (c) T = 200 °C and (d) T = 220 °C. The SEM images were taken in a FEI Verios 360L microscope at landing energy of 8 kV and probe current of 25 pA.

are the nanostructures of interest. It is worth emphasizing that the substrate temperature at which the triangle-like shaped GaN is formed corresponds to the optimal temperature used in previous case of the substrate with a larger miscut angle.

In contrary to SEM imaging, an XPS analysis was carried out in situ, i.e. directly after the deposition of gallium and post-nitridation inside the vacuum chamber without exposing the sample to the ambient atmosphere. In situ XPS was performed using an experimental setup consisting of an X-ray source - DAR400 and a hemispherical electrostatic analyzer -

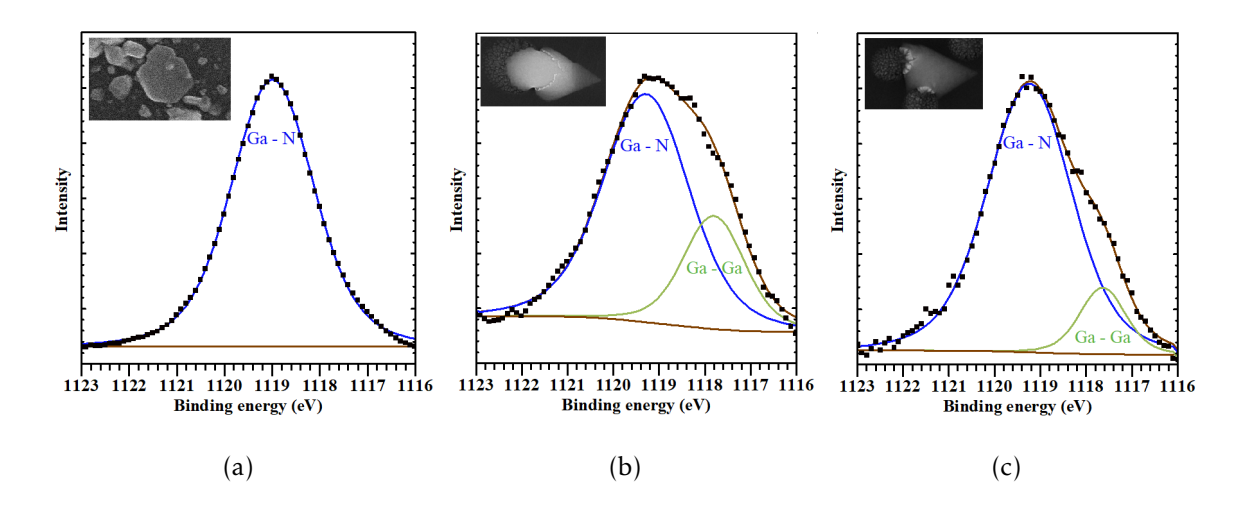


Figure 26: XPS spectra of the gallium $Ga2p_{3/2}$ peak. (a) $Ga2p_{3/2}$ peak corresponding to the bulky GaN used as a reference. (b) $Ga2p_{3/2}$ peak in the middle of the formation of the 2D GaN. (c) $Ga2p_{3/2}$ peak after the formation of the 2D GaN was finished. The subpeak at 1117.5 eV (green line) is attributed to the metallic gallium while the peak at 1119.5 eV (blue line) corresponds to the Ga - N bond.

EA125 (both Omicron). The experiments were performed at the room temperature using Al $K\alpha$ radiation. Figure 26 (a) shows the gallium $Ga2p_{3/2}$ peak in XPS spectrum corresponding to the Ga - N bond in a bulk GaN which serves here as a reference. The peaks in Figure 26 (b) and Figure 26 (c) show different stages of the formation of 2D GaN. The peaks in Figure 26 (b) show the middle phase of the formation process. There are two separate subpeaks in the spectrum corresponding to Ga - N and Ga - Ga types of bonds. The peak at 1117.5 eV (green line) corresponds to metallic gallium while the peak at 1119.5 eV (blue line) corresponds to the Ga - N bond in a bulk GaN. Figure 26 (c) reveals the $Ga2p_{3/2}$ peak after the formation of GaN is finished. The Ga - N subpeak becomes prominent at the expense of the Ga - Ga subpeak which, however, is still present in the spectrum. Based on these findings, we can speculate on the growth mechanisms of 2D GaN. The evolution of the Ga2p_{3/2} peak suggests that Ga atoms from the metallic gallium droplets react with nitrogen ions which results in the formation of GaN structures. As triangle-like shaped GaN grows in size, the portion of Ga - N bonds is becoming dominant. However, a small fraction of gallium droplets still remains in the metallic form which is supported by the presence of the remaining Ga - Ga subpeak in the spectrum. This is probably caused by the fact that not all gallium droplets are fully transformed into GaN since the area which is covered by the nitrogen flux is smaller than that one of the X-ray beam spot. Thus, the collected XPS

signal includes also the signal from the remaining gallium droplets at the edges of the sample. Alternatively, a portion of metallic gallium can be also preserved at the very border of the triangle-like nanostructures and the place of the original liquefied metallic gallium nanodroplet (bright part in the included SEM image in Figure 26 (c)).

The objects of interest are shown in the SEM image in Figure 27 (a). There are three features in each individual object of interest. The first is a triangle-like shaped GaN. The triangle-like GaN nanostructure is most likely defined by the surface reconstruction of Si (111) 7x7 which shows a six fold hexagonal symmetry. This nanostructure has a uniform thickness with slightly tapering tip. Each triangle is oriented towards the direction of incoming nitrogen atoms (during post-nitridation). The second feature of the object is a circular region. This is probably etched silicon with some remnants of Ga since a similar effect called "meltback etching" was already observed during the growth of other gallium structures on silicon [161]. The third feature is the most likely bulky GaN in between the triangle and the circular spot (bright features in the SEM image).

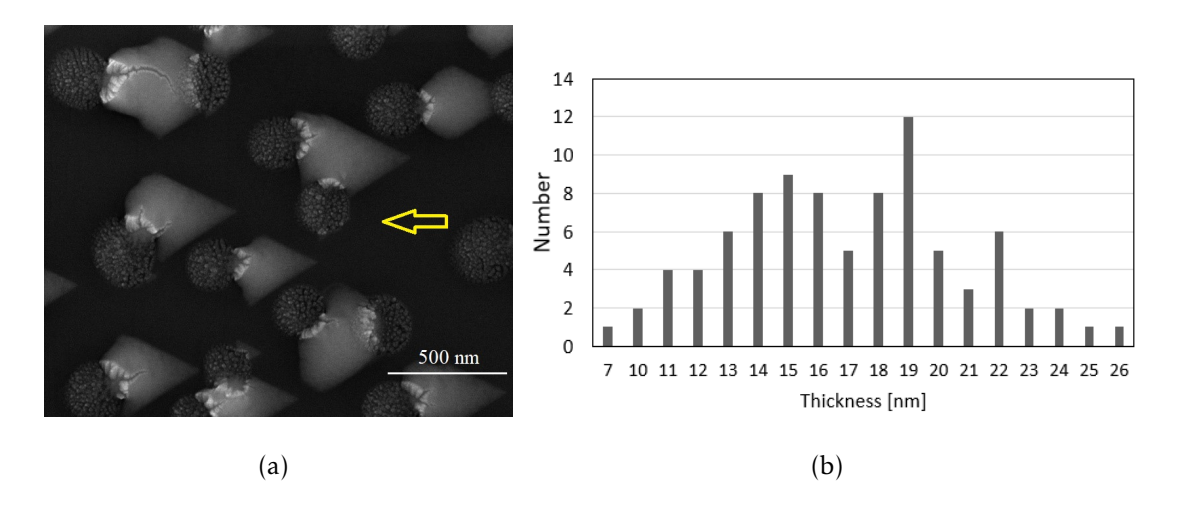


Figure 27: (a) SEM image of triangle-like shaped GaN nanostructures. The yellow arrow indicates the projected direction of incoming nitrogen ions. (b) Thickness distribution of the triagle-like shaped nanostructures measured by an AFM (ICON Bruker) in a tapping mode.

With this knowledge the growth mechanism can be outlined. The deposition of gallium results in a formation of metallic gallium droplets spread all over the surface. Once the nitrogen ions start to impinge on gallium droplets, they interact with gallium atoms, and thus post/nitridation is initiated. Several mechanisms enter the reaction as was explained

in Section 4.1 in detail. The metallic gallium is continuously consumed and transformed into hexagonal GaN. The question whether the growth of the triangle-like nanostructures is layer by layer or it is rather initiated in the vicinity of the original droplet and then continue growing in the upstream direction of incoming nitrogen ions is still open. The same stands for the etching of silicon. It is difficult to answer whether this etching is initiated during the deposition of gallium or after the initiation of post-nitridation. The in-SEM growth could possibly reveal the growth mechanisms in the future.

The AFM measurement of the thickness of the triangle-like shaped GaN provides a thickness distribution as plotted in Figure 27 (b). It can be clearly seen that the thickness varies from 7 nm to 26 nm with the maximum between 14 nm and 20 nm which is more than two times thicker than in the case of triangular nanostructures described in previous Section 6.2 with maximum at 7 nm. The increased thickness can be most likely attributed to the fact that gallium atoms can diffuse over longer distance because of wider surface terraces compared to the previous case. Thus, more material can be consumed from the gallium droplet.

The Auger microanalysis reveals an elemental composition in different regions around the nanostructure as illustrated in Figure 28. There are three different regions A, B, C selected in the SEM image in Figure 28 (a). The region A corresponds to the Si (111) surface in the place of the original Ga droplet, the region B represents the triangle-like nanostructure and the area of the remnants of the original gallium droplet is represented by the region C. The Figure 28 (b) represents the presence of Ga atoms in the selected regions measured by the Auger electron microscopy. Gallium is missing on the Si (111) surface as expected. However, gallium is present in the triangle-like nanostructure as well as in the region of the original droplet. Figure 28 (c) indicates the presence of nitrogen on the silicon surface (region A) which indicates that nitrogen ions initiated the formation of silicon nitride here. Nitrogen atoms are also present in the triangle-like nanostructure (region B). However, there are no nitrogen atoms in the place of the original gallium droplet (region C). Such finding can be interpreted so that the nitrogen atoms are not dissolved in the droplet of metallic gallium. As proposed by Gerlach et al. [118] nitrogen ions rather diffuse along the liquid-vapor (gallium droplet surface) and solid-vapor (substrate surface) interfaces. During the diffusion nitrogen ions interact with gallium atoms which initiates a nucleation which eventually results in a layer formation. Alternative explanation can be provided based on the fact that

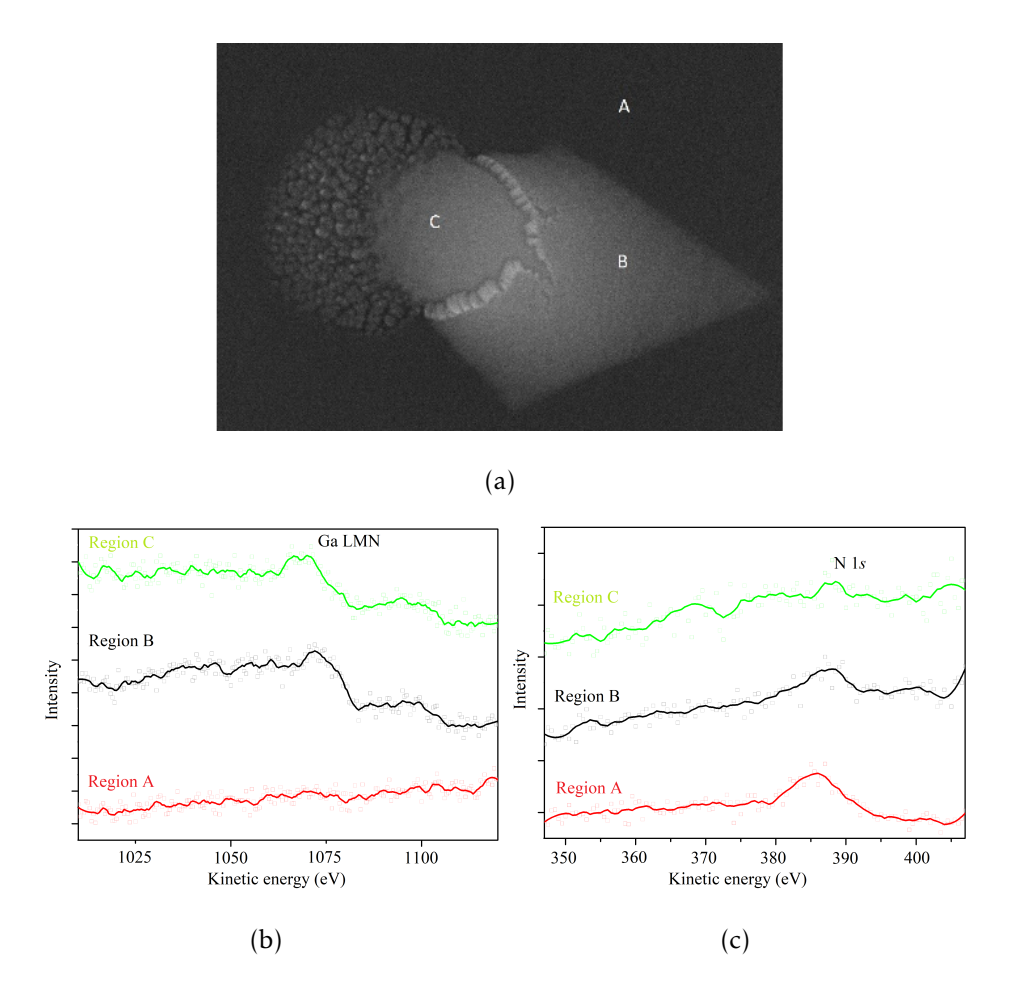


Figure 28: SEM image of a triangle-like shaped GaN with a not fully consumed gallium droplet. (a) SEM image of the structure of interest with the selected regions A, B and C. (b) Gallium presence in the selected regions. (c) Nitrogen abundance in the selected regions. The Auger microanalysis was conducted in a NanoSAM System (Scienta Omicron).

there is always observed crystalline border (bright crystals in SEM images in Figure 27 (a) or Figure 28 (a)) between the triangle-like nanostructure and etched silicon area. It is possible that nitrogen ions initially react with the gallium droplet and form crystalline bulky GaN on the side of the droplet exposed to the nitrogen flux. As nitridation continues, gallium and nitrogen atoms precipitate from this bulky nanocrystals and form observed thin layer.

The Auger microanalysis also suggested possible formation of silicon nitride. It is natural to expect that irradiation of a pristine silicon substrate by nitrogen ions will result in a formation of SiN. However, the structure of formed SiN is still an open question. It has been demonstrated that implantation of nitrogen ions of energies i) tens of keV [162], ii) units of keV [163] and iii) hundreds of eV [164, 165] into pristine silicon substrate results in a forma-

tion of i) crystalline [162], ii) amorphous [163] and iii) crystalline [164] or amorphous [165] SiN structures, respectively. So, it seems that with decreasing energy of nitrogen ions the formed layer changes from crystalline to amorphous. Obviously, this aspect is influenced by various parameters such as changing the dose, the incident angle or the substrate temperature. Despite a number of conditions which may affect a formation of SiN, the process itself seems to be described clearly. The nitrogen ions break the silicon bonds once they penetrate into the substrate. Subsequently, retarded ions react with broken or dangling bonds and form chemically stable silicon nitride (with Si₃N₄ stoichiometry [166]).

In order to investigate a crystalline structure, i.e. find lattice parameters, a cross-sectional TEM lamella was prepared and analyzed in FEI Titan HR (S)TEM microscope. STEM image shown in Figure 29 (a) reveals a crystalline structure of the prepared nanostructure. An interlayer distance of GaN structure was 3.15 Å which is in agreement with the interlayer distance of the crystalline GaN (3.14 Å) measured in previous Section 6.2. On one hand the measured interlayer distance is in the upper end of the interval (2.22 Å – 3.10 Å) of interlayer distances for 2D hexagonal GaN coming from numerical simulations, on the other hand the value is similar to the interlayer distance of silicon (a = 3.16 Å). The lattice parameter a = 3.32 Å is higher than in the case of smaller triangular GaN nanostructures described in previous Section 6.2 but still close to the value for 2D hexagonal GaN, which is a = 3.28 Å [159].

EDX maps showing the distribution of nitrogen and gallium in the structure are visualized in Figure 29 (b). The upper part of the STEM image shows studied GaN nanostructure on the silicon substrate. The middle part of the image reveals the distribution of gallium which seems to be uniform over the whole structure. Interestingly, the nitrogen atoms appears to be mostly distributed in the region of crystalline GaN which is in agreement with the argument given in the previous Section 6.2 that nitrogen and gallium atoms form a crystalline GaN mostly outside the original metallic gallium droplet.

The final argument about the nature of the prepared material could be provided by the photoluminescence measurement. The blue shift in the energy of emitted light (from 3.4eV in case of wurtzite GaN to 3.7eV in case of hexagonal GaN) described in [153] suggests a significant quantum confinement which is typical for sub-3D equivalent of bulky materials.

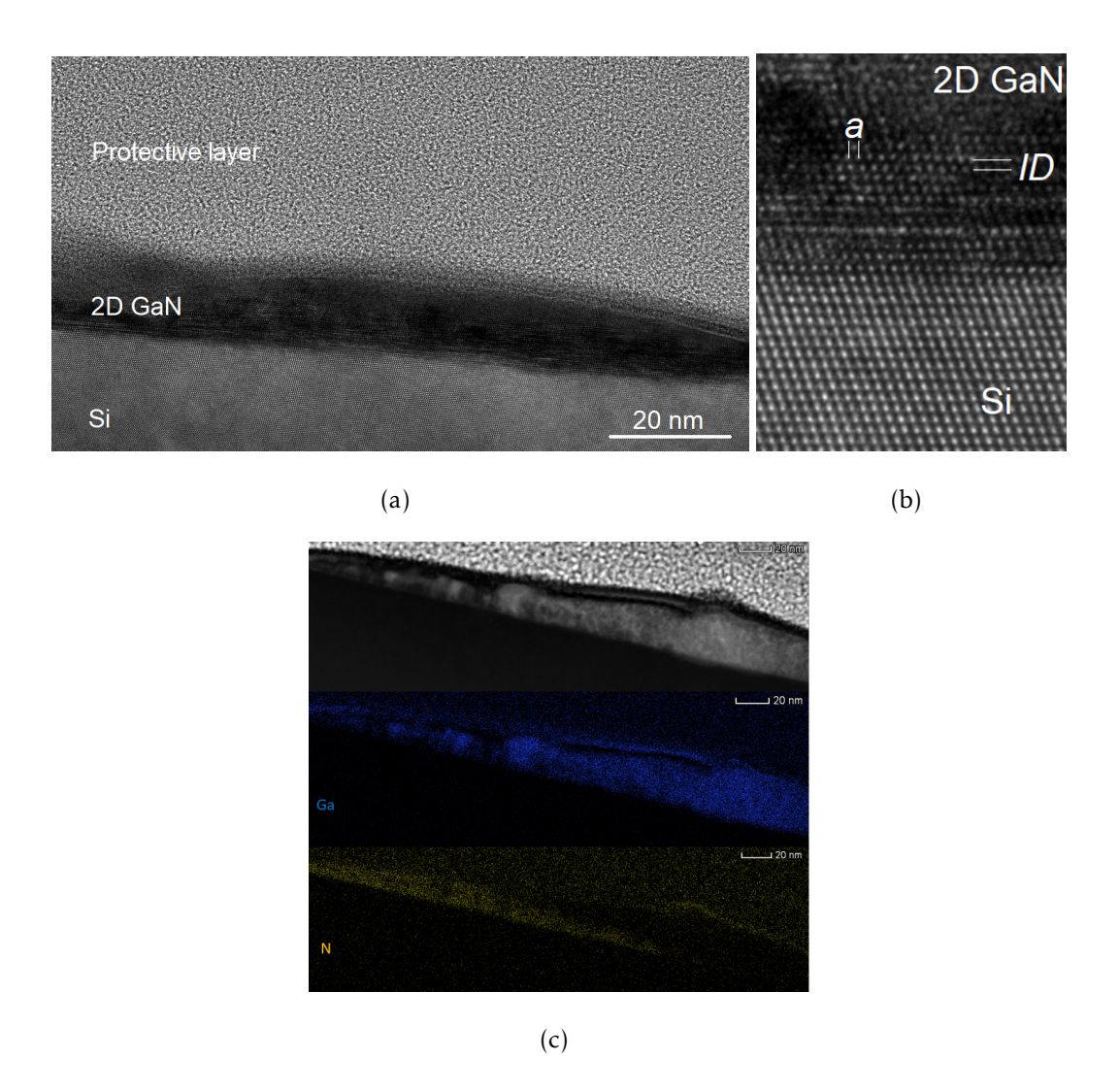


Figure 29: (a) STEM image of the cross-sectional lamella of crystalline GaN on the Si(111) substrate. b) The zoom-in image of an Si/GaN interface. a represents a lattice constant and ID represents an interlayer distance. (c) EDX maps of GaN structure. While gallium is detectable in the crystalline structure as well as in the amorphous droplet, nitrogen is present only in the crystalline GaN structure. The STEM images were taken in a HR (S) TEM (FEI Titan).

Thus, the allotropic modifications of prepared structures can be found based on the evaluation of emitted photoresponse. However, all attempts to measure a photoluminescence response were unsuccessful due to a low signal-to-noise ratio of the optical response. This might by caused by the high conductivity of the silicon substrate which is necessary for the flash-annealing routine but inappropriate for photoluminescence measurement in which it causes quenching of the photoluminescence signal.

6.4 Conclusion

It has been shown that post-nitridation of metallic gallium droplets on a Si(111) surface by hyperthermal nitrogen ions of energy $E = 50 \,\text{eV}$ at the substrate temperature $T = 200 \,^{\circ}\text{C}$ results in a formation of layered hexagonal triangular GaN nanostructures which indicates the 2D material structure. The size of formed nanostructures was up to 500 nm in the case of GaN nanostructers grown on Si (111) with the $0.2 \,^{\circ}$ miscut.

The XPS analysis as well as the Auger microanalysis enabled to determine the elemental composition of prepared structures and helped to clarify the growth mechanism.

The STEM and EDX analysis elucidated the crystalline structure of triangle-like GaN features rendering the lattice constant $a = 3.32\,\text{Å}$ and the interlayer distance 3.15 Å. The interlayer distance is considerably higher than in the case of the wurtzite GaN structure $(a = 2.53\,\text{Å})$ but is in the interval calculated for 2D hexagonal GaN $(2.22\,\text{Å} - 3.10\,\text{Å})$. The lattice parameter $a = 3.32\,\text{Å}$ is also larger than in the case of the wurtzite structure $a = 3.18\,\text{Å}$ and is very close to the value calculated for hexagonal GaN $(a = 3.28\,\text{Å})$ [159].

The photoresponse signal, however, exhibited an extremely low signal-to-noise ratio. Thus, it could not be evaluated. Extremely low signal-to-noise ratio could be probably caused by a high conductivity of the silicon substrate which is needed for the flash-annealing routine but causes quenching of the photoluminescence signal.

7 GaN nanowires

This Section summarizes the experimental work on fabrication of GaN in the one dimensional form - nanowires. Presented results were obtained during the internship in the group of professor Ernesto Joselevich at the Weizmann Institute of Science in Rehovot, Israel. The period of the internship was filled up with two different projects. First, an application of metal-organic precursors in an already established CVD fabrication process was tested. This project was focused on optimizing the GaN nanowires growth parameters motivated by the goal to find appropriate growth conditions of oxygen-free nanowires. Second, the nanowires growth kinetics was studied. In this project, geometrical characteristics of GaN nanowires grown on different sapphire planes were collected. Subsequently, collected data was used as an experimental approval of a developed theoretical model for horizontally grown nanowires.

The nanowires are one dimensional nanostructures which are result of anisotropic growth in the vertical as well as horizontal orientations with respect to the surface normal vector. During the last few decades a number of different materials has been studied from the point of view of materials suitable for nanowires. A variety of different substrates with different surface modifications - as for instance with lithographic patterns [167] - has been studied in the same time in order to match the most beneficial substrate to appropriate nanowires. Naturally, the pioneering work was done using silicon as the silicon is number one in the microelectronic field [168]. As the foundation of silicon nanowires fabrication had been laid down, the focus was directed to other combinations of materials such as germanium [169], II-VI [170] and III-V [171] group semiconductors or perovskites [172] to mentioned a few. Expanding the possibilities of fabrication of different kinds of nanowires have brought a large number of applications in electronic devices. To give only a few examples, nanowires were implemented into field effect transistors [173], nanowire waveguides [174], and even LEDs [175]. Following the trends, the nanowires have also been implemented into plasmonic applications which opened up another direction for possible research [176].

The comprehensive overview of the fundamental research activities considering synthesis, characterization and application of one dimensional nanostructures can be found in [177]. A follow-up overview of the advances in the nanowire semiconductors where the

fundamental principles of the bottom-up growth are summarized is then provided in [178]. However, following the topic of the presented PhD thesis the further focus will be directed to III-V group semiconductors exclusively, especially to GaN which is the material of interest in the following experimental work.

The story of discovering the 1D modification of III-nitrides goes several decades back when boron nitride was synthesized as a multi-wall nanostructure in 1995 [179]. Since that time a significant progress in fabrication of single-wall nanotubes and nanowires has been achieved. In these days, 1D h-BN modifications are used in the number of applications, especially due to its wide band-gap making h-BN insulating material [180].

Following the successful synthesis of h-BN, different kinds of synthesis strategies of gallium nitride nanotubes, nanorods or nanowires have also been developed. From synthesizing GaN nanorods through a carbon nanotube-confined reaction [181] to fabricating the single crystal GaN nanotubes [182], GaN 1D variants attract scientific interest because of their electrical and optical properties.

An interesting aspect of the GaN nanostructures is the possibility of a guided horizontal growth. The motivation behind this effort is very simple. Nanowires are often implemented into devices with a planar architecture such as transistors or photoactive devices. However, nanowires are usually synthesized in the form of vertical structures. After the synthesis, nanowires thus need to be harvested, transferred and aligned to the desired position. This process often erodes electrical, optical or mechanical properties since nanowires can be broken during each step. For that reason, the fabrication of nanowires in the region of interest with requested orientation seems to be beneficial for advanced applications.

The pioneering work in the synthesis of guided growth of GaN nanowires came with millimeter long epitaxial or graphoepitaxial GaN nanowires which were grown in the crystallographic directions defined by the surface of a substrate. Horizontal GaN nanowires were grown on sapphire [183], silicon carbide [184], quartz [185] and spinnel [186]. Self integration of GaN nanowires into an electrical circuit via guided growth is yet another step for achieving completely self-integrated nanowires during devices fabrication [187].

However, in order to take a full advantage of direct self-assembling nanostructures, several obstacles have to be overcame. Besides the obvious aspects such as choosing appropriate combinations of materials or tuning the parameters of the growth reactors, there are also more fundamental questions which are waiting to be answered. Among the others, understanding the mechanisms which are involved in a nucleation process or knowing the factors influencing the length and diameter of nanowires are crucial for a proper implementation of this growth concept into modern microelectronic devices. In order to describe these growth aspects, a theoretical description of the growth mechanisms can be used advantageously.

Up to date, the growth mechanism called vapor-liquid-solid (VLS) is the most widely adopted growth method for the fabrication of semiconductor nanowires [188]. As the name suggests, this process involves three phases of the source (nanowire) materials. First, the source materials are introduced into a growth chamber in the form of gases (vapor). Second, the source material atoms impinge on the surface and form a liquefied alloy (liquid) with the catalyst. Third, the crystalline material (solid) precipitates from the liquefied alloy in the form of a one dimensional nanowire. A detailed description of the VLS growth process will be provided in Section 7.3.1.

It is worth mentioning that the theoretical model of the growth kinetics of out-of-plane nanowires has already been provided and supported by various experimental works [189, 190]. On the other hand, the theoretical description of VLS mechanisms in the case of inplane nanowires has been provided just recently [191]. Experimental results in the following Sections of presented PhD thesis thus serve as an additional verification of the developed theoretical model.

7.1 Sample preparation

Sapphire (Al_2O_3) is an insulating crystal consisting of aluminium and oxygen atoms ordered in a hexagonal structure. Cutting the sapphire in different directions results in obtaining various crystal planes with various surface reconstructions and adequate surface energies. A non-polar annealed M-plane ([10 $\bar{1}0$]), C-plane ([$\bar{1}100$]) and a semi-polar R-plane ([1 $\bar{1}02$]) substrates were used for comparison of epitaxial and graphoepitaxial growth modes since these are two modes which can occur during horizontal nanowires growth process.

In a natural state, all three sapphire planes have a flat surface. However, in order to study the effect of the surface geometry on the horizontal growth, the M-plane was modified so that its originally flat surface was transformed into the jagged one. The M-plane wafer was exposed to a temperature of T = 1600 °C in air atmosphere for 10 hours using a high-temperature furnace (Nabertherm). Therefore, it is referred as an annealed M-plane (AM-plane) in the following sections. This treatment resulted in a formation of ordered V-shape nanogrooves covering the whole area of the surface wherein the nanogrooves were oriented in the main crystallographic direction [11 $\overline{2}0$].

Since the growth of horizontal GaN nanowires was catalyzed by the nickel nanoparticles, the samples were prepared adequately. Sapphire substrates were covered with a catalyst pattern in the form of a matrix of nickel rectangles, the size of which was $30 \times 5 \, \mu \text{m}^2$. The catalyst pattern was fabricated by a standard photolithography technique in the following steps. First, the sapphire wafer was covered by a negative photoresist (NR-9 1000PY) and held at a temperature of $100\,^{\circ}\text{C}$ for 1 minute. Second, sapphire was irradiated with a UV lamp through a lithography mask with a matrix of rectangulars (MA/BA6 Karl-Suss mask aligner). Third, the saphhire wafer was immersed into a developer for 10 seconds and placed on a hot plate at a temperature of $150\,^{\circ}\text{C}$ for 1.5 minute. Lastly, the wafer was placed into the evaporator (Telemark) where 0.5 nm of nickel was deposited. Samples were then washed in aceton, isopropylalcohol and deionized water before each synthesis in order to remove the photoresist. Afterwards, samples were held in a furnace at the atmospheric pressure and the temperature of $550\,^{\circ}\text{C}$ for 7 minutes to desorb residuals and to produce nickel nanodroplets of various sizes. At this point, prepared samples were loaded into a CVD reactor.

7.2 MOCVD gallium nitride nanowires

The MOCVD apparatus consists of a tube placed inside a three-zone furnace (Lindberg Blue M, Thermo Fisher Scientific) and a gas supply system. At the beginning of the routine, the tube was purged with a mixture of 1 300 sccm of molecular nitrogen and 90 sccm of molecular hydrogen at a pressure of 400 mbar. Purging ensures removing of dust contaminants and reducing the level of oxygen molecules from ambient atmosphere remaining inside the tube after sample loading. Following the purging, the temperature of the furnace was set to 950 °C and the gas flow was modified accordingly. The absolute values are listed in Table 3. Reaching the required temperature of the synthesis took approximately 30 minutes. During this period of time, the cleanliness of the sample surface was steadily increasing as a result of thermal desorption of contaminants.

$T_{furnace}(^{\circ}C)$	$T_{TMG}(^{\circ}C)$	N_2 (sccm)	H_2 (sccm)	NH_3 (sccm)	$N_2 + TMG$ (sccm)	p (mbar)
940	-15	80	80	30	120	150

Table 3: Parameters for the synthesis of GaN nanowires in the MOCVD apparatus using TMG.

The specifics of the MOCVD method is introducing the source materials in a form of metal organic compounds. In this particular case, an organogallium compound of three methyl derivatives bound to one gallium atom was used as a gallium source material. This pyrophoric liquid is called trimethylgallium $Ga(CH_3)_3$ (usually abbreviated as TMG or TMGa). The second material - nitrogen - was provided in the form of stable hydride - ammonia. Once those two gases are introduced to the tube, the enhanced temperature causes their decomposition according to the following chemical reaction:

$$Ga(CH_3)_3(g) \to Ga(s) + 3CH_3(g),$$
 (10)

$$2NH_3(g) \rightarrow N_2(g) + 3H_2(g),$$
 (11)

$$2 Ga(s) + N_2(g) \rightarrow 2 GaN(s).$$
 (12)

Obviously, the product of the reaction - gallium nitride - is adsorbed in the solid form on the surface. The main advantage of this approach is the absence of oxygen atoms which can, in general, negatively affect properties of gallium nitride as for instance photoluminescence peak.

GaN nanowires grown from TMG on an AM-plane substrate are shown in Figure 30. It can be clearly seen that the catalyst area is covered with large faceted crystals. However, no horizontal growth of nanowires can be observed. Nanowires preferentially grow from the tips of large crystals and bend at some arbitrary point towards the surface. Once the bent nanowires reach the surface, they tend to grow in the direction of the nanogrooves. Thus, the nanogrooves act as mediators of the growth direction.

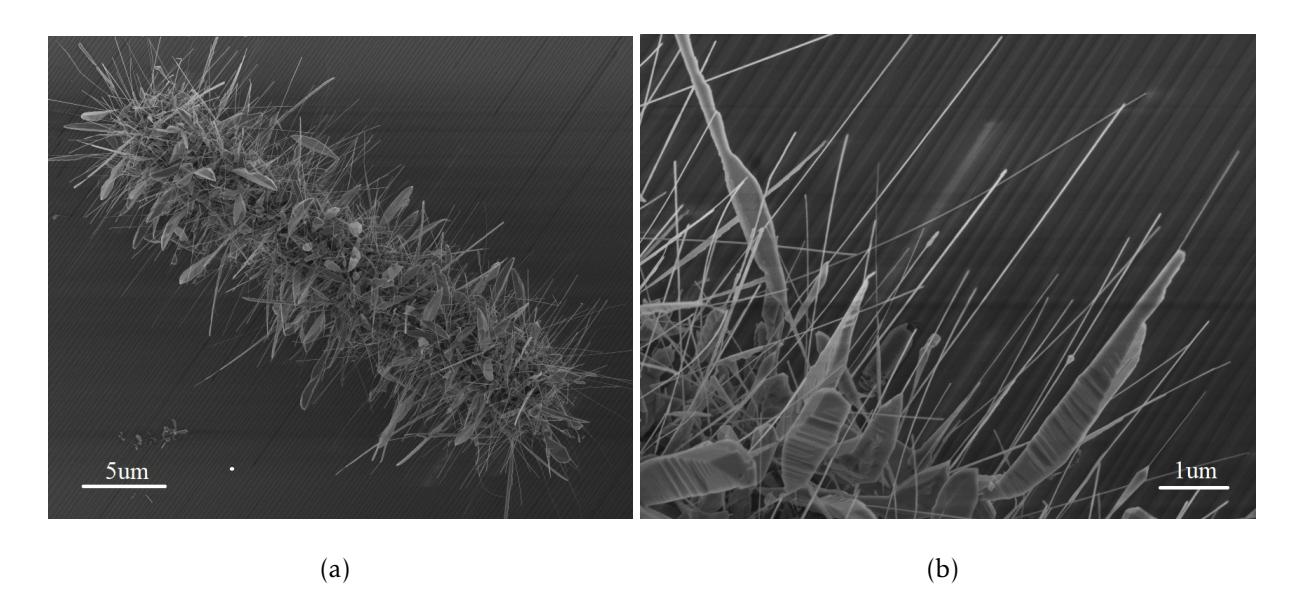


Figure 30: (a) MOCVD GaN nanowires growing from chunky crystals. The images were taken on SEM Sigma 500, Zeiss.

Initial experiments provided nanowires with the average length of about 3 μ m. Tuning the substrate temperature did not bring any improvement. On the other hand, the changing of the TMG gas flow resulted in increasing the average length of nanowires up to 9 μ m. The critical factor affecting the nanowires length seemed to be a concentration of TMG as resulted from follow-up synthesis. However, the further decreasing of the TMG gas flow was not possible because of limited sensitivity of used flowmeter. Therefore, the modification of the instrumentation was suggested and designed. Nonetheless, the delivery time of a special kind of flowmeter exceeded the project time in Israel. Thus, it was not possible to test suggested changes and the project was postponed.

Despite the fact that longer nanowires could not be synthesized, an additional analysis was performed. The EDX analysis (Figure 31) reveals the elemental composition of the syn-

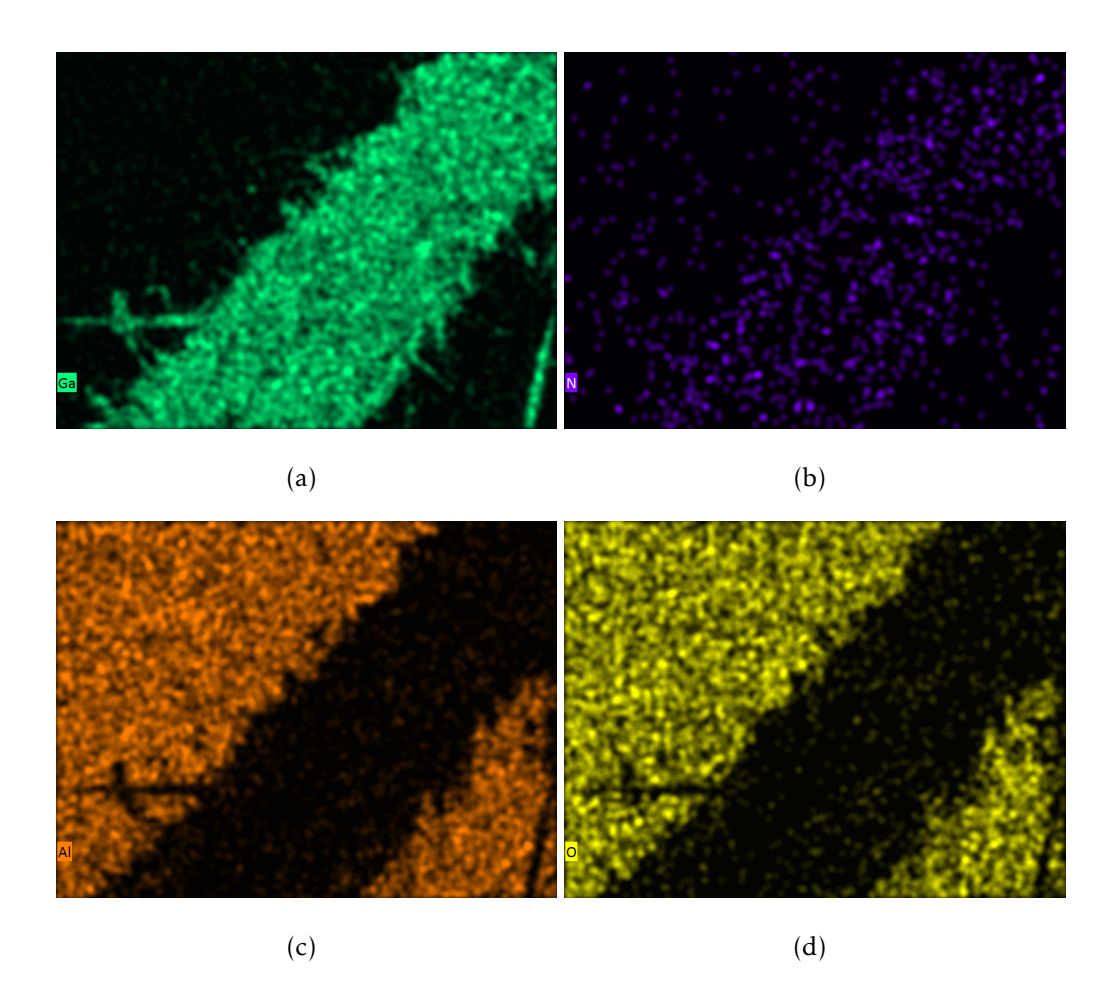


Figure 31: Elemental EDX maps of (a) gallium, (b) nitrogen, (c) aluminium and (d) oxygen related to MOCVD GaN nanowires. The images were taken on SEM Sigma 500, Zeiss, using an EDX spectrometer (Bruker) and software.

thesized structures. It can be clearly seen that the faceted crystals as well as nanowires (GaN) are composed of gallium (Figure 31 (a)) and nitrogen (Figure 31 (b)) as expected, while the sapphire substrate (Al_2O_3) is composed of aluminium (Figure 31 (c)) and oxygen (Figure 31 (d)). Yet, a low lateral resolution of EDX in SEM cannot provide a definite evidence of an absence of oxygen impurities in the GaN crystal structure.

The photoluminescence measurement in Figure 32 reveals a comparison of MOCVD GaN nanowires prepared using TMG as a precursor (blue line) and CVD GaN nanowires prepared using Ga₂O₃ powder as a source of gallium on R-plane (green line) and AM-plane (red line). The preparation of latter GaN nanowires will be discussed in the following Section 7.3. It can been clearly seen that the MOCVD GaN photoluminescence peak at 364 nm (3.40 eV) is shifted with respect to the CVD GaN photoluminescence peak at 354 nm

(3.50 eV) by 10 nm. The peak position at 364 nm (3.40 eV) is close to the value expected for a bulk GaN (3.42 eV) as defined in Table 1 in Section 4.4. Thus, the peak position for CVD GaN nanowires at 354 nm (3.50 eV) can be considered as a blue shift rather then a reference value.

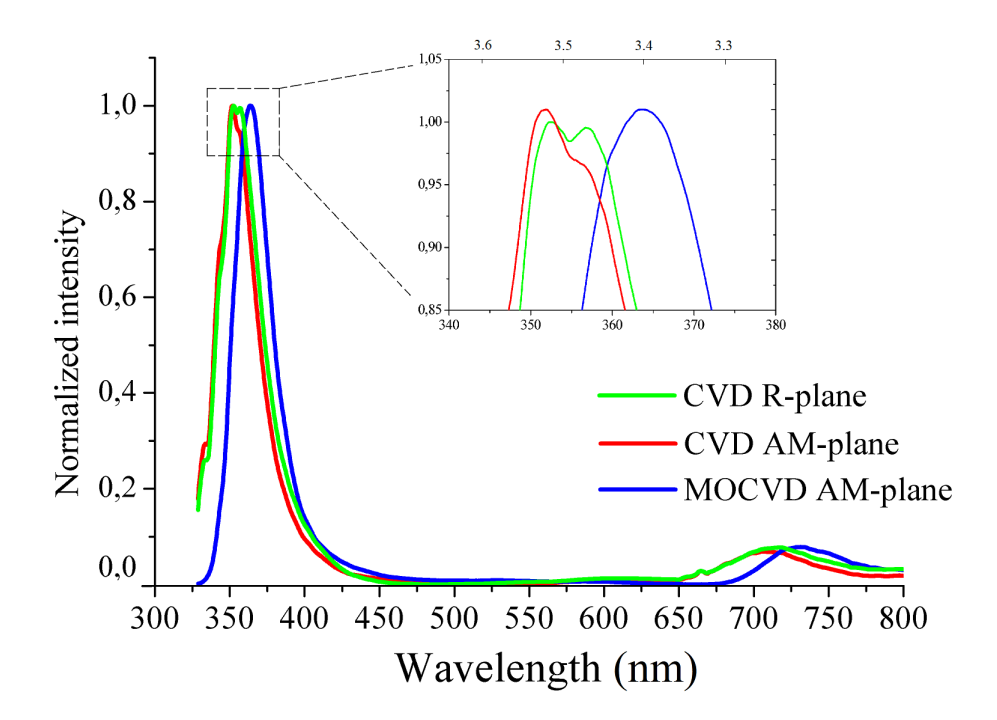


Figure 32: Photoluminescence of nanowires grown by different methods (MOCVD and CVD). The spectra were measured using a Raman/PL micro-spectroscopic setup (Witec) using 325 nm laser excitation laser.

Interestingly, the very same shift was already observed in [192], where the authors compared the photoluminescence of a-axis GaN nanowires (354 nm (3.50 eV)) and c-axis GaN nanowires (364 nm (3.40 eV)). The authors attributed the blue shift of a-axis GaN nanowires to "surface states that act as traps of photoexcited carriers". Their results suggest that the photoluminescence response is a crystal-orientation sensitive. However, in the presented case, no blue shift was observed between nanowires grown on different sapphire planes where the difference in orientation could be expected but it rather differs in nanowires grown using different methods. It is worth mentioning that the authors of the referred study used different conditions even though they used the same precursors (ammonia) for inducing a-axis and c-axis growth on a quartz glass and a graphite substrate. Therefore, in accordance with our observations, it is also possible that the photoluminescence response of GaN nanowires

is also dependent on the method used as the different methods might provide different crystal orientations.

Our photoluminescence measurements have also revealed that there is no yellow peak observed in an interval of 450 nm and 650 nm which suggests the absence of the impurities incorporated in the crystal lattice of nanowires. The effect of impurities was already discussed in detail in Section 5.1.3 where the photoluminescence response of GaN nanocrystals (Figure 18) was presented. The absence of the yellow emission peak indicates a high crystal quality of grown nanowires. Thus, the only difference between the MOCVD and CVD growth remains the blue shift of the characteristic GaN peak as described above.

7.3 CVD gallium nitride nanowires

The CVD instrumental arrangement was similar to one described in the previous section. The crucial difference was in the used source material. Contrary to gaseous TMG in the MOCVD case, a Ga_2O_3 powder was used in this case. The samples - annealed M-plane, R-plane and C-plane - were used with the same catalyst pattern as in the previous case, i.e. an array of $30 \times 5 \,\mu\text{m}^2$ rectangles of 5 Å thick layer of nickel. Additionally, R-plane was covered with an array of $30 \times 30 \,\mu\text{m}^2$ squares of this Ni layer. The optimal parameters found for the synthesis of GaN horizontal nanowires for all three sapphire plane variants are summarized in Table 5.

	T _{furnace} (°C)	$T_{Ga_2O_3}$ (°C)	H_2 (sccm)	NH_3 (sccm)	p (mbar)
AM-plane	940	1000	95	3.2	400
R-plane	940	1000	90	2.7	400
C-plane	950	1000	95	3.2	400

Table 4: Optimal parameters for the synthesis of GaN nanowires in the CVD reactor using gallium oxide powder.

As can be seen in Figure 33, the nanowires grow on all three substrates. However, the quality of guided growth depends on the surface termination. In the case of the annealed M-plane (Figure 33 (a)), GaN nanowires are guided by nanogrooves in the main crystallography direction - so-called graphoepitaxial growth was already introduced by the group of prof. Joselevich. Nanowires vary in lengths and diameters as will be shown later, but the longest nanowires reach tens of microns. As can be seen in Figure 33 (b), the tip of a nanowire is formed with a catalyst droplet. The R-plane surface is also covered with the nanowires as can be seen in Figure 33 (c). In this case, the epitaxial growth is directed by the crystalography of the surface. Therefore, some of nanowires can grow in the direction not parallel to the main crystallography direction. In the case of C-plane, the majority of nanowires has a zig-zag structure even though they tend to grow in the main crystalographic direction. Besides those zig-zag nanowires, the firm nanowires can also be observed in Figure 33 (e). It is also worth mentioning that the very tip of each nanowire is formed by a droplet catalyst. No self-catalyzed nanowires were observed which suggests that the growth process is initiated by the catalyst.

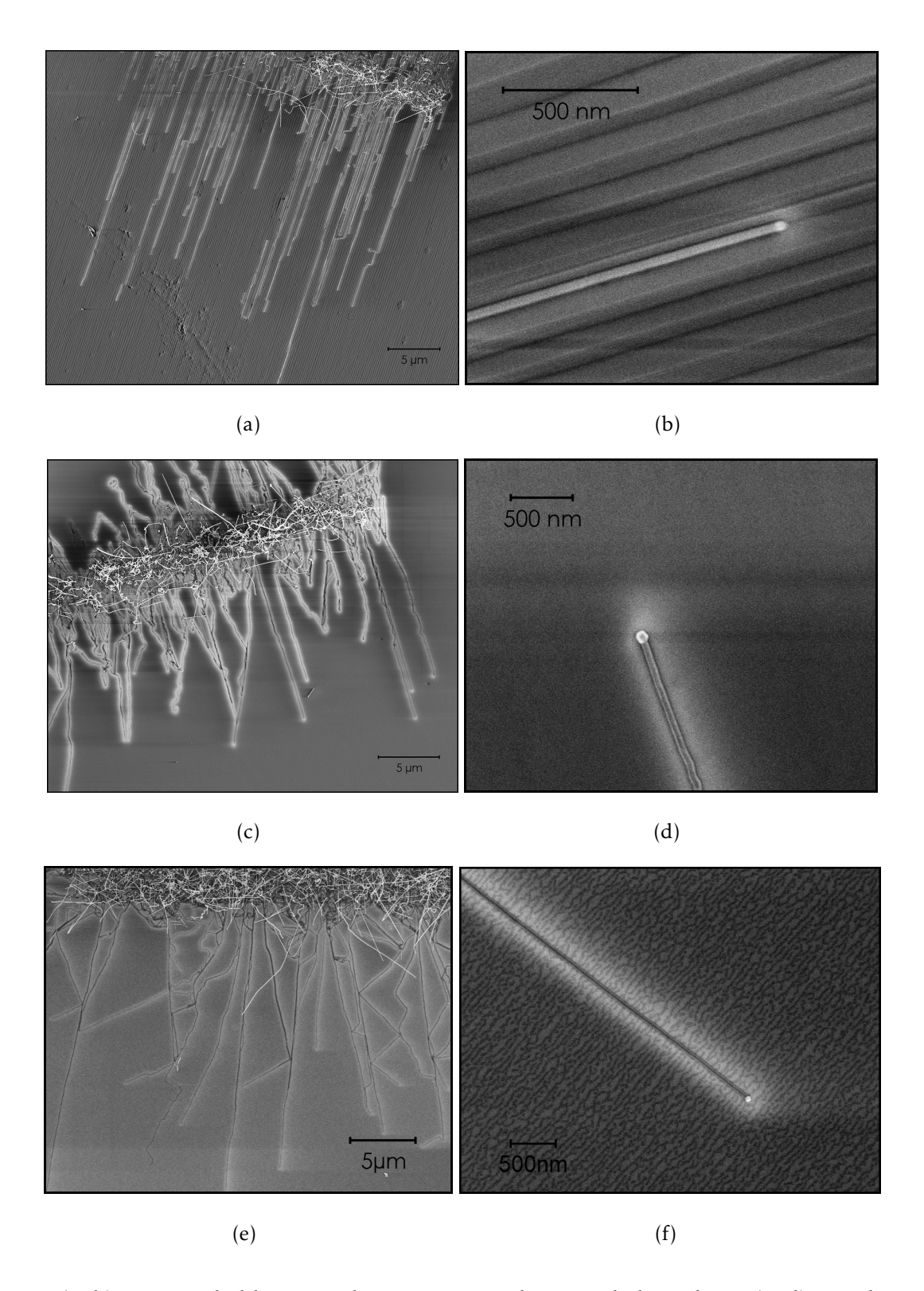


Figure 33: (a, b) GaN guided horizontal nanowires on the annealed M-plane. (c, d) GaN horizontal nanowires on the R-plane. (e, f) GaN horizontal nanowires on the C-plane.

The Raman spectra of GaN nanowires grown on different sapphire planes using different precursors (TMG and Ga_2O_3) are plotted in Figure 34. The reference sapphire spectrum

(black line) has the peaks at $380 \,\mathrm{cm^{-1}}$, $418 \,\mathrm{cm^{-1}}$, $645 \,\mathrm{cm^{-1}}$ and $750 \,\mathrm{cm^{-1}}$ which is in agreement with published literature [193]. There is no variation in the spectrum for the AMplane and the R-plane. The spectra corresponding to GaN nanowires possess three peaks at $570 \,\mathrm{cm^{-1}}$, $733 \,\mathrm{cm^{-1}}$ and $750 \,\mathrm{cm^{-1}}$. According to [194] where the GaN thin film on sapphire substrate was studied, the peak at $570 \,\mathrm{cm^{-1}}$ corresponds with $E_2(\mathrm{TO})$ (transverse) phonon mode while the $735 \,\mathrm{cm^{-1}}$ peak is attributed to $A_1(\mathrm{LO})$ (longitudinal) phonon mode.

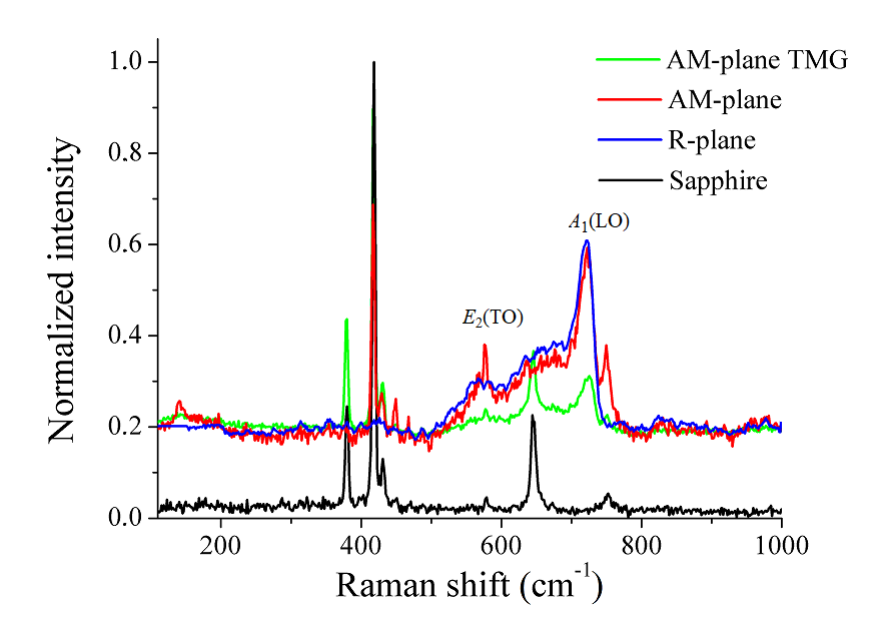


Figure 34: Raman spectra of nanowires grown using different precursors. The spectra were measured using Raman/PL micro-spectroscopic setup (Witec) using a 325 nm excitation laser.

The Raman peaks which would correspond to the disorder (300 cm⁻¹) or impurities induced vacancies or interstitial (420 cm⁻¹ and 670 cm⁻¹) according to [195] are either not observed (300 cm⁻¹) or cannot be distinguished from the sapphire peaks (420 cm⁻¹ and 670 cm⁻¹). Thus, the possible effect of oxygen impurities in CVD GaN nanowires or their absence in MOCVD GaN nanowires could not be estimated. However, the visual distinction between those two alternatives is clearly seen. While the spectra of CVD GaN nanowires on both the AM-plane and the R-plane between 500 cm⁻¹ and 800 cm⁻¹ exhibit peak broadening or background increase, the very same interval of the Raman spectrum corresponding to MOCVD GaN nanowires exhibits rather a flat profile with separated peaks. These findings may be associated with the actual difference between nanowires grown using different methods but one has to be bear in mind that it can be also caused by lower surface den-

sity (surface coverage) of nanowires in case of MOCVD growth which could cause a lower nanowires-to-substrate signal ratio.

Synthesized nanowires were further used as a dataset for a study of the growth kinetics of horizontal nanowires as will be described in the next Section 7.3.1. Serve to this purpose, only the nanowires grown on AM-plane and R-plane were taken into consideration. The number of acceptable nanowires grown on C-plane did not meet a criteria for high quality statistics. Therefore, the nanowires grown on C-plane were excluded from the kinetics study.

7.3.1 Kinetic model of horizontal nanowires

Growth of nanowires is an anisotropic thermodynamically driven process resulting in a formation of one-dimensional nanostructures. As such, the growth can be theoretically described involving several thermodynamic aspects which will be expressed further in this Section. Despite the fact that the nanowires can be grown by various method, the following derivation is limited to the vapor-liquid-solid (VLS) growth mechanism.

At the very beginning of the synthesis there are catalysts droplets (noble or transition metals) spread over the surface. Due to the high substrate temperature, the catalyst is in the form of liquefied droplets. The growth process is initiated by introducing the source materials into the CVD reactor in the form of gases. The CVD reactor is described in Section 4.3. Because of the elevated temperature, the precursors are dissociated and the source material impinges onto a substrate surface. The atoms of the source materials adsorbed on the surface (adatoms) start to diffuse over it. Such a movement is driven by the thermodynamically induced effects described in Section 4.2.2. Once the source material atom reaches a catalysts droplet, it penetrates through the droplet surface which leads to a formation of a liquefied alloy of the droplet and source materials.

The thermodynamic system of a source material dissolved in a catalyst droplet can be described by using of a phase diagram. The system of three different materials (in this case nickel, gallium and nitrogen) is represented by a three-dimensional plot (ternary diagram). However, the complexity of such ternary diagram can be inadequate for the growth descrip-

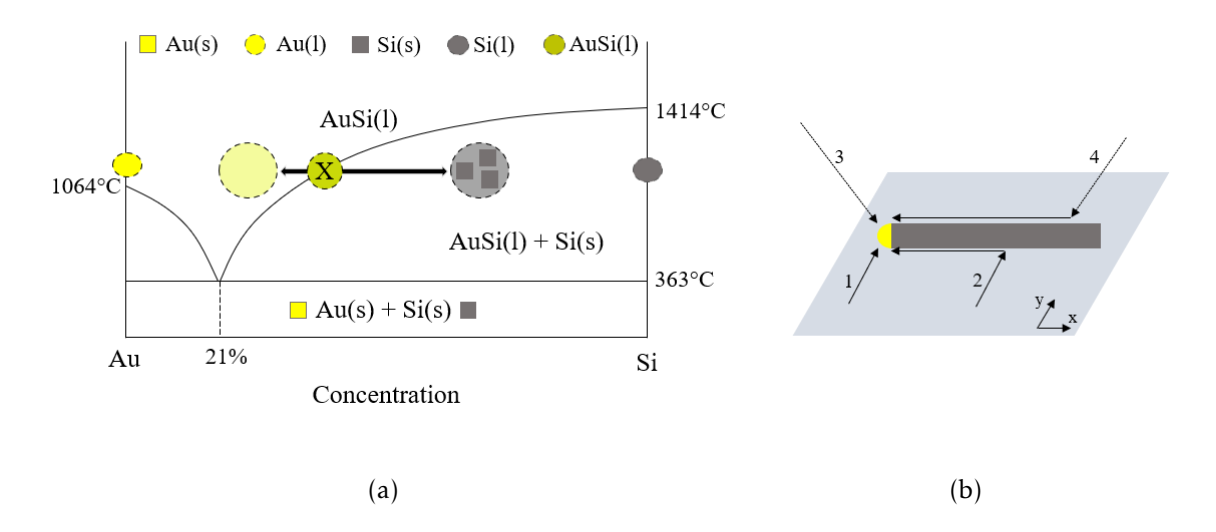


Figure 35: (a) Phase diagram of a Au+Si system [188]. (b) Schematic representation of adatoms pathways in diffusion-induced growth.

tion. Therefore, a gold-silicon binary diagram will be used for the exemplification since this system served for the development of the growth kinetics theoretical model in the past [188] and it is still used nowadays as the simplified system for the real time *in-situ* observation [196].

The phase diagram of the Au-Si system is plotted in Figure 35 (a). The eutectic point of the system (defining the minimal growth temperature) is 363 °C. The Au-Si alloy follows the liquidus line above the eutectic temperature which also defines the thermodynamic equilibrium between the liquid and the solid phase. For a given concentration of silicon atoms in the Au-Si alloy, the system is in the equilibrium only at the temperature given by the intersection of the liquidus line and the concentration (point X in the diagram). However, since the CVD process is a dynamic process, small fluctuations in the temperature or the vapor pressure around the equilibrium position are inevitably present. Such fluctuations can lead to dissolving more Si atoms in the Au-Si system which leads to establishing the state of supersaturation (solid arrow). The supersaturation represents an unstable state of a thermodynamic system, which has, in contrary, tendency to preserve in the equilibrium. Therefore, the precipitation of silicon solid phase from the Au-Si liquid is initiated. The precipitation continues until the system reaches the thermodynamic equilibrium again, i.e. until the concentration of the silicon is reduced to the equilibrium level (point X). As a result, the solid phase of silicon, i.e. crystalline nanowire, is formed as the CVD process

continues. In this sense, the formation of nanowires can be considered as a product of a thermodynamic system balancing around its equilibrium state.

Rapid development of environmental electron microscopy has enabled real time *in-situ* observations of this phenomenon as described in [197, 198]. The authors studied a Au droplet of initial diameter of 35 nm exposed to disilane (H_6Si_2) gas. After introducing disilane, an initial Au droplet was instantly covered by a thin Au+Si liquefied shell. The Au droplet further reduced its diameter to 15 nm. At that point, the Au solid core shrank very rapidly. The rapid shrinkage indicates that the Au(s)/AuSi(l) thermodynamic system is unstable below a critical solid Au nucleus radius. Ongoing supply of disilane eventually resulted in an initiation of solid silicon nucleation. The authors observed a sudden appearance of an Si nucleus at the edge of the liquefied alloy droplets. Subsequent observation of the same system revealed that the Si(111)/AuSi(l) interface further advances by 0.3 nm steps which corresponds to the interlayer distance in Si(111). Thus, the VLS growth of Si nanowires seems to proceeds in a layer-by-layer fashion [196].

In order to make the formation of the alloy possible, the catalyst has to be chosen carefully since there are several requirements which have to be fulfilled. 1) It must be chemically inert in order to avoid any chemical reaction with the source material. 2) It must not form an intermediate solid, which could cause a deprivation of catalytic potential. 3) It must form a solution with the source material components. 4) The solubility of the catalysts in a liquid phase have to be higher than in a solid form. 5) The vapor pressure of the catalyst material over its liquid phase should be minimal in order to minimize evaporation. The overview of suitable catalysts for variety of different nanowires can be found in [188].

The physico-chemical model which describes such a complex thermodynamic system from the point of view of a reaction rate is called a growth kinetics. The kinetic model discussed below is based on several simplifications and presumptions which are necessary to keep a complexity of the process at a level which could be described rigorously. However, it still brings a realistic description of the system and allows to obtain useful information about the reactions rates and how are these affected. A kinetic model of the growth of vertical nanowires developed by prof. Dubrovskii [199] is based on a mathematical description of a mutual interplay between two surface effects - the Gibbs-Thomson effect and a surface

diffusion induced growth. The kinetic model of vertically grown nanowire served then as a solid base for a development of the corresponding model for the growth of horizontal nanowires as will be discussed below.

The dynamic system of growing nanowires can be simplified in the way depicted in Figure 35 (b). The nanowire is in contact with the substrate along its whole length and is growing in the y direction. It is also isolated in space from other nanowires. The nanowire is represented by 1/2 of a cylinder while the catalyst droplet is defined as 1/4 of a sphere. The diameter of the nanowire and catalyst is time-independent and equal to R. The diffusion of catalyst atoms to the volume of nanowires is neglected, even though the catalyst loss channels were already observed [200]. The source material transport paths are simplified to follow either parallel or perpendicular directions with respect to the nanowire. There are four possible pathways which ensure the material transport (in this case gallium and nitrogen) into the catalyst:

- 1. Diffusion over the surface directly to the catalyst droplet.
- 2. Diffusion over the surface to the nanowire sidewall and subsequent diffusion along the sidewall.
- 3. Direct penetration from the flux of incoming source material to the catalyst droplet.
- 4. Direct impingement on the nanowire sidewall and subsequent diffusion along the sidewall.

Considering all possible pathways the growth rate dL/dt can be formulated as

$$\frac{\mathrm{d}L}{\mathrm{d}t} = 2\Omega \left(I - \frac{n_{\mathrm{l}}}{\tau_{\mathrm{l}}} + \frac{j_{\mathrm{diff}}^{\mathrm{s}}}{\pi R^{2}} + \frac{j_{\mathrm{diff}}^{\mathrm{f}}}{\pi R^{2}} \right),\tag{13}$$

where Ω is the elementary volume, I is the flux rate of the element limiting the growth rate (Ga in this case), $n_{\rm l}/\tau_{\rm l}$ is the desorption flux from the droplet with the characteristic lifetime in liquid $\tau_{\rm l}$, $j_{\rm diff}^{\rm s}$ is the diffusion current over the substrate surface towards the nanowire and $j_{\rm diff}^{\rm f}$ is the diffusion current along the sidewall (surface facet).

At this point, Equation 13 is strictly diffusion oriented. In order to account for the Gibbs-Thomson effect the effective concentration of adatoms inside the droplet can be expressed in the form:

$$n_{\rm l} = n_{\rm l}^{\infty} \exp\left(\frac{R_{\rm GT}}{R}\right),\tag{14}$$

where n_1^{∞} represents the concentration of adatoms inside the droplet for the limit case of $R \longrightarrow \infty$, i.e. $n_1^{\infty} = I\tau_1$, and $R_{\rm GT}$ is the characteristic Gibbs-Thomson radius which is defined by a droplet surface energy γ at a given temperature T. Equation 14 thus represents the elevation of chemical potential with respect to the varying radius R.

While the values of majority of variables in the equation are known, the two diffusion currents make the equation unsolvable analytically. However, by introducing several simplifications such as dividing the diffusion current directions into the perpendicular and parallel ones with respect to the nanowire only, the equation can be simplified into a more practical form:

$$\frac{\mathrm{d}L}{\mathrm{d}t} = 2\Omega I \left\{ 1 - \Theta_{\mathrm{lv}} \mathrm{e}^{\mathrm{R}_{\mathrm{GT}}/\mathrm{R}} + \left(1 - \Theta_{\mathrm{ls}} \mathrm{e}^{\mathrm{R}_{\mathrm{GT}}/\mathrm{R}} \right) \left(\frac{\lambda}{\mathrm{R}} \right)^{\mathrm{m}} \right\},\tag{15}$$

where $\Theta_{\rm lv}=n_{\rm l}^{\infty}=I\tau_{\rm l}$ is the liquid to vapor activity, $\Theta_{\rm ls}=n_{\rm l}^{\infty}=I\tau_{\rm s}$ is the liquid to solid activity, $R_{\rm GT}$ is the Gibbs-Thomson radius, λ is the diffusion length and m is the power exponent. The liquid to vapor $\Theta_{\rm lv}$ and liquid to solid $\Theta_{\rm ls}$ activities correspond to the overall diffusion flux of adatoms diffusing either towards or away from the catalyst droplet from vapor or over the surface, respectively. Interestingly, in the limit case of omitted surface diffusion $\lambda \to 0$, Equation 15 is reduced to the length-radius dependence.

The mathematical reasoning behind provided simplifications is out of scope of this thesis but can be found in [191]. For the purpose of presented results, a crucial parameter is the power exponent m varying between 1 and 2 and representing the three dominant diffusion pathways represented by 1, 1.5 and 2. For $m = 1 \Rightarrow 1/R$, the major material transport pathway is mediated by adatoms which directly impinged on the nanowire sidewall and diffuse along the sidewall subsequently. In contrary, $m = 1.5 \Rightarrow 1/R^{3/2}$ corresponding to thicker nanowires and $m = 2 \Rightarrow 1/R^2$ corresponding to thinner nanowires indicate diffusion of adatoms over the surface directly to the catalyst droplet. Collecting the data on nanowires lengths vs. radii can be thus used as an effective way how to determine the dominant diffusion pathways as will be shown in following Section 7.3.2.

7.3.2 Data fitting

Data collected for the study of growth kinetics consists of nanowires grown on the annealed M-plane (AM-plane) and the R-plane. The measurement of the length and diameter of the nanowires was carried out by analyzing the SEM images (Sigma 500, Zeiss) in the ImageJ software using a line profile module. The quality factor of the measured values was evaluated by a comparison with the AFM measurement (Multimode Nanoscope 7.30, Veeco/Bruker) of the same region of interest. The comparison revealed that the difference in measured diameters using SEM images versus AFM images is below 10% in case of nanowires grown on the R-plane. The AFM measurements on the AM-plane failed to provide a reliable comparison because of the presence of nanogrooves. The dimensions of nanowires grown within those nanogrooves are confined by the width of each nanogroove. The AFM tip cannot be placed at the very edge of the nanowire during scanning but rather forms a smooth transition over nanogroove edge. Therefore, only SEM images were used for the diameter and length evaluation of nanowires.

The edge of a nanowire (as well as a catalyst droplet) was defined as the place of a transition between bright and dark contrast in the SEM image. The diameter was then measured in the perpendicular direction to those edges. The length of the nanowires was measured from the very top of the catalyst droplet to the place from which the nanowire starts to grow firmly. In addition, the nanowires which were in contact (even at one point) with the neighboring nanowires were excluded from the data collection. Thus, only nanowires which grew straight from the place of the growth initiation without any affection by neighboring nanowires were included to the dataset.

In order to verify the assumption made upon the relationship between the diameter of the catalyst and the width of the nanowire in the kinetic model in Section 7.3.1, such a dependence was studied at first. Figure 36 shows the relationship between the catalyst radius and corresponding nanowire radius for nanowires grown on the annealed M-plane (blue points) and the R-plane (red points). In both cases the dependence shows a linear trend with slope coefficient $k_{\rm AM}=0.519$ and $k_{\rm R}=0.562$ for the AM-plane and the R-plane, respectively. These results clearly confirmed that the width of the nanowire was defined by the diameter of the catalyst droplet as assumed during the development of the model.

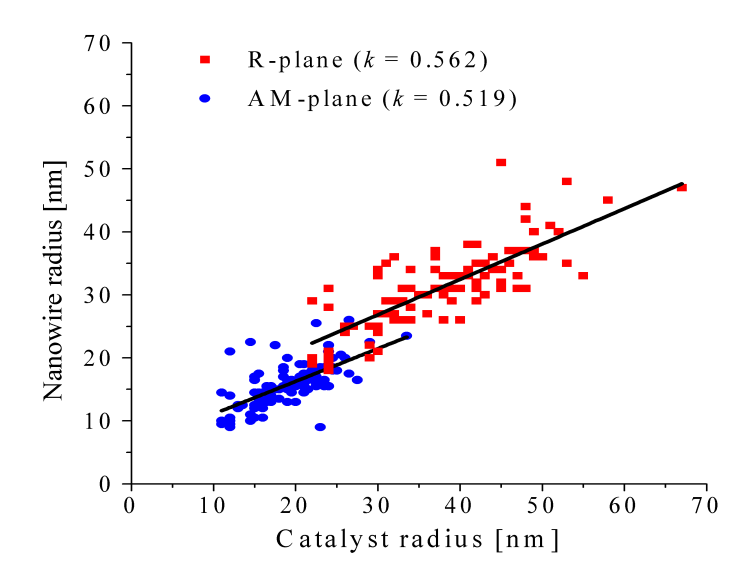


Figure 36: Catalyst radius versus corresponding nanowire radius for AM-plane (blue circles) and R-plane (blue square). Datasets are fitted with linear functions with the slope *k* parameter.

In the following, the diameter of nanowires and corresponding lengths were measured for each individual nanowire. Measured datasets are plotted in the Figure 37 (a) and (b). For further analysis, however, the radius of the nanowires was plotted as a function of the growth rate. Growth rate was calculated from the maximal nanowire length for a given radius by its division by the overall time of synthesis which was 25 min. Th reasoning for this simplification will be discussed later in this Section.

Figure 37 (a) represents dataset of nanowires dimensions measured on the AM-plane. The radius varies between 10 nm and 25 nm which corresponds with an approximate nanogrooves width of 40 nm. In contrary, the radius of nanowires grown on the R-plane varies from 20 nm to 50 nm as can be seen in Figure 37 (b). Considering the flatness, i.e. the absence of nanogrooves, on the R-plane, the difference in the radius range of nanowires on the AM-plane and the R-plane can be attributed to the topography of the surface. The length of nanowires on both types of substrates was spread over larger intervals. The maximal measured length was approximately 30 μ m which corresponds (considering the 25 min as a time of the synthesis) to the growth rate of $1.4 \, \mu$ m · min⁻¹ as can be seen in the both plots.

The spread of nanowires' lengths can be attributed to the different incubation times. Incubation time is defined as a period of time between the beginning of the synthesis and

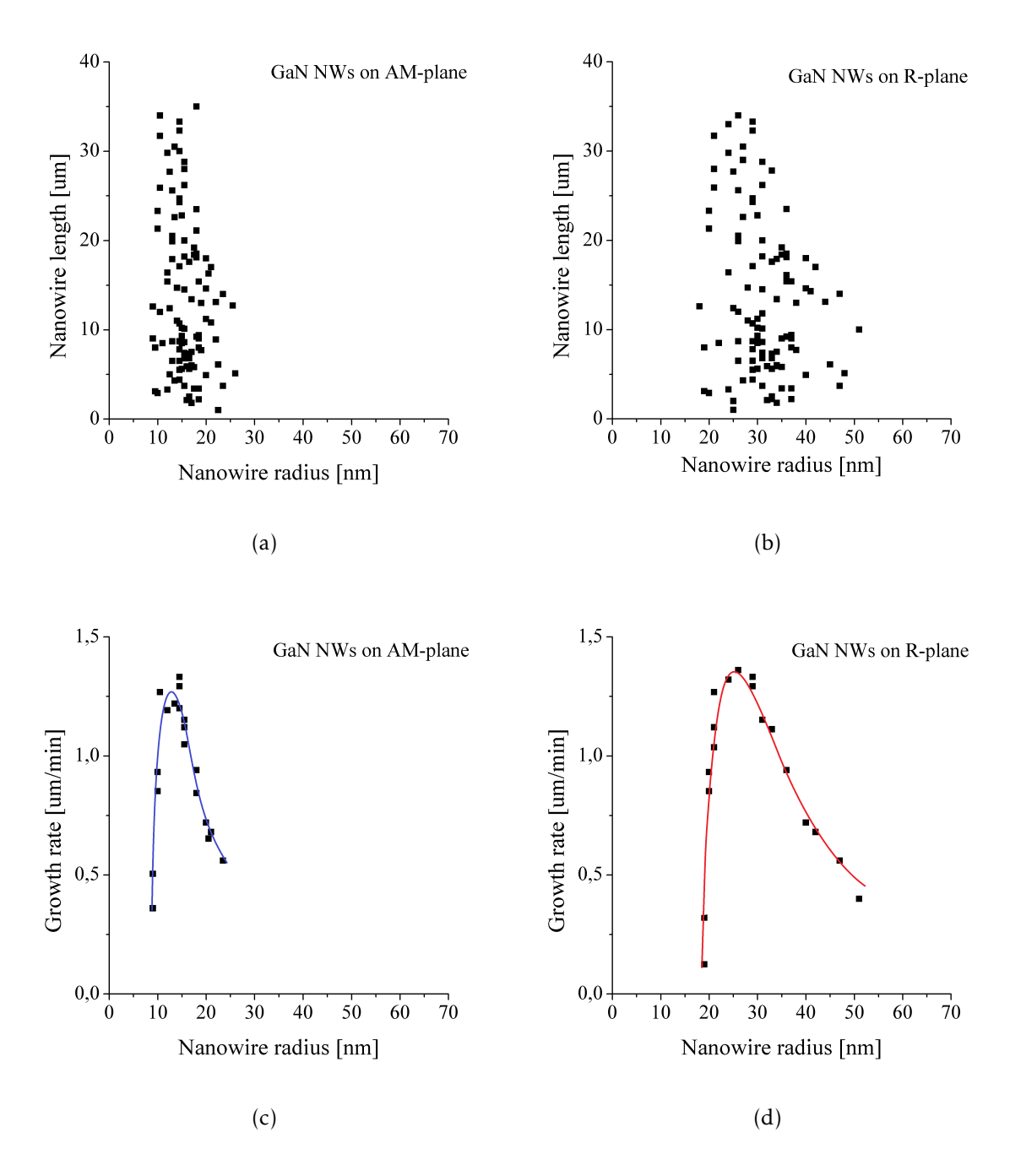


Figure 37: Dependence of nanowire length with respect to nanowire radius of GaN nanowires grown on (a) AM-plane and (b) R-plane. Envelope data of GaN nanowires grown on (c) AM-plane and (d) R-plane fitted with the kinetic Equation 15. The y-axis is recalculated from the length to the grow rate (L/t, where t is the time of synthesis).

the initiation of growth. As described in Section 7.3.1, the source material penetrates into a catalyst droplet and forms an alloy. Once this system reaches the supersaturation, i.e. the concentration of source material atoms exceeds the equilibrium value, the source material starts to precipitate from the material. The very moment of precipitation is considered

as the initiation of growth. However, the moment at which the source material starts to precipitate from the droplet significantly depends on the size of the droplet as well as its closest neighborhood. While the size of the droplet affects the amount of the source material dissolved in the catalyst before reaching supersaturation, the neighborhood of the droplet affects the diffusivity of the source material. In summary, while the beginning and the end of the synthesis is defined, the initiation period of growth varies for each catalyst droplet which significantly influences the maximum length.

In order to circumvent the variation in incubation time, only envelope data were considered for subsequent analysis. The justification of this simplification lays in the fact that the nanowires lengths laying on the envelope can be presumed to be the maximal with respect to corresponding radii [201]. Thus, the growth of these nanowires was initiated at the very beginning of the synthesis.

Sap. plane	$\Omega I (\mu \mathbf{m} \cdot \mathbf{min}^{-1})$	Θ_{lv}	Θ_{ls}	$R_{\mathrm{GT}}(\mathrm{nm})$	λ (nm)	m
AM-plane	0.63 ± 0.12	1.00 ± 0.05	0.47 ± 0.03	6.02 ± 0.13	40.93 ± 2.71	2.02 ± 0.15
R-plane	5.67 ± 0.78	1.00 ± 0.05	0.69 ± 0.02	5.34 ± 0.09	46.85 ± 0.55	1.93 ± 0.17

Table 5: Fitting parameters used and calculated based on the kinetic model.

Selected data (Figure 37 (c) and Figure 37 (d)) were then fitted using Equation 15. Obtained parameters are summarized in Table 5. The power factor m was found to be close to 2 for both the AM-plane ($m_{\rm AM}=2.02$) and the R-plane ($m_{\rm R}=1.93$). As was described above the power factor m=2 is associated with the surface diffusion of adatoms towards the catalyst droplet. Hence, the diffusion along the sidewall is limited in this case. The diffusion length λ differs from ≈ 41 nm for the AM-plane to ≈ 47 nm for the R-plane. The diffusion length in both cases is substantially smaller than the overall lengths of nanowires which varies from $5\,\mu{\rm m}$ to as much as $30\,\mu{\rm m}$. Interestingly, the diffusion length on the AM-plane is comparable to the width of the surface nanogrooves. In the same time, it is 13 % smaller in comparison with the R-plane with a flat surface. This can explain the difference in maximum diameter of nanowires which is almost two times bigger on the R-plane compared to the AM-plane. Since the nanogrooves act as a natural barrier for the adatoms diffusion, the amount of the source material capable of diffusing into the catalyst droplets is effectively reduced which results in a smaller maximum diameters while the length is comparable on

both sapphire planes.

The deduced power exponents m close to 2 are in good agreement with the already reported values for flat (sapphire C-plane) $m = 1.8 \pm 0.2$ and faceted (sapphire AM-plane) $m = 1.8 \pm 0.1$ Au-catalyzed ZnS and ZnSe horizontal nanowires [191]. As ZnS and ZnSe are representatives of II-VI semiconductors while the GaN is representative of III-V group, the obtained result may be generalized to surface guide horizontal nanowires. The mechanisms of the growth of horizontal nanowires is preferentially mediated by two-dimensional diffusion of adatoms over the substrate surface directly towards the catalyst droplets. This mechanism differs from the situation in the case of vertical nanowires, whose growth is dominated by the one-dimensional diffusion along the nanowire sidewalls[202].

7.4 Conclusion

In this Section, the guided growth of horizontal GaN nanowires has been demonstrated. The nanowires were synthesized applying two distinct approaches based on different types of the source material - trimethylgallium (TMG) and gallium oxide powder. In both cases, the growth of GaN nanowires was achieved. However, the synthesis of GaN nanowires from TMG was limited due to the instrumental issues. Thus, the yield of those nanowires were substantially lower than in the case of gallium oxide powder where the hardware allowed a fine tuning of the reactor conditions.

Nevertheless, both types of nanowires were studied in order to find possible differences in electro-optical properties. It was found that the GaN nanowires prepared from TMG exhibited a photoluminescence emission at $\lambda=364\,\mathrm{nm}$ which corresponds with the value expected for a bulk GaN. On the other hand, GaN nanowires synthesized from a gallium oxide powder exhibited a blue shift of the photoluminescence peak to $\lambda=354\,\mathrm{nm}$. Such a blue shift was already recognized as an effect of different growth directions. However, since the surface orientation was the same for both types of nanowires, it is possible that observed blue shift is linked to the method used for a synthesis. It is also worth emphasizing that neither of GaN nanowires exhibited a yellow 'defect' peak in the photoluminescence response which indicates a high crystal quality.

Further, the dataset of lengths vs. radii of nanowires was collected in order to provide the data fortheir fitting by a growth kinetic model. This theoretical growth model of horizontal nanowires was previously developed and reported by prof. Dubrovskii in cooperation with the group of prof. Joselevich [191]. The data collected on the growth of GaN horizontal nanowires were in agreement with the previously reported data for ZnS and ZnSe nanowires. Moreover, since ZnS and ZnSe represent semiconductors of a different elemental group than GaN, one may concluded that the theoretical model can be extended to the growth of horizontal nanowires in general.

To summarize the outcome, the growth of horizontal nanowires is fueled by the adatoms of the source material diffusing over the surface directly towards the catalyst droplet. This is in contradiction with the growth of vertical nanowires where the adatoms have to diffuse along the nanowire sidewall before they reach the catalyst droplet [199].

8 Conclusion

I have presented results of three individual projects which have been done during my PhD program. All projects were related to a fabrication and characterization of III-V group representative - GaN. I have presented preparation of GaN in three different forms - 1D, 2D and 3D structures - using different fabrication techniques.

First, 3D GaN in the form of nanocrystals prepared using droplet epitaxy method has been demonstrated. The fabricated GaN nanocrystals were studied using different analytical techniques in order to elucidate the quantitative aspect of the growth as well as the quality of prepared structures. GaN nanocrystals were grown on a graphene layer which have brought a possibility to fabricate an UV sensitive photodetector. A proof of concept - a design and basic functionality - has been explored with a positive outcome which paves the way for following research. As a result, a new PhD position focusing on further exploration of the designed UV sensitive photodetector has been opened in our group.

Second, growth of 2D GaN at low temperatures has been studied. 2D GaN nanostructures were grown on two different Si substrates and analyzed by various techniques such as XPS, TEM and Auger spectroscopy to provided qualitative study of their nature. The mechanisms of their growth was suggested based on the provided measurements and already published literature. The results of this side project were published in *Nanoscale Advances* [57] and presented as an oral talk at the International Vacuum Conference in Malmo in 2019.

Third, study of a 1D GaN nanowires growth kinetics has been performed. This project consisted of fabrication of GaN nanowires on various sapphire substrates and following measurement of their dimensions. Collected data were used for evaluation of a proposed theoretical model of the horizontal GaN nanowires growth. This effort is a part of a long-term cooperation between the group of Prof. Ernesto Joselevich in the Wiezmann Institute of Science and Prof. Vladimir Dubrovskii from St. Petersborough University in Russia. The results were published in *Nanomaterials* [58]. Provided data on GaN nanowires supported the model and extend its applicability to a III-V group of semiconductors.

9 Authors publications and other outputs

Publications

Maniš, J., Mach, J., Bartošík, M., Šamořil, T., Horak, Michal, Čalkovský, V., Nezval, D., Kachtik, L., Konečny, M. and Šikola, T. Low temperature 2D GaN growth on Si (111) 7x7 assisted by hypethermal nitrogen ions. *Nanoscale Advances*, 4:3549-3556, 2022.

Rothman, A., Maniš, J., Dubrovskii, V. G., Šikola, T., Mach, J. and Joslevich, E. Kinetics of guided growth of horizontal GaN nanowires on flat and faceted sapphire surfaces. *Nanomaterials*, 11, 2021.

My contribution: Fabrication and analysis of GaN nanowires.

Mach, J., Piastek, J., Maniš, J., Čalkovský, V., Šamořil, T., Damková, J., Bartošík, M. and Voborný, S., Konečný, M. and Šikola, T. Low temperature selective growth of GaN single crystals on pre-patterned Si substrates. *Applied Surface Science*, 297, 2019.

My contribution: Fabrication of GaN crystals.

Conferences

International Vacuum Conference 2019, Malmö, Sweden. Oral talk: Two-dimensional GaN grown on Si(111)7x7 with assisted hyperthermal nitrogen ions at low temperature.

CEITEC PhD Retreat II, Telč, Czech Republic, 2019. Oral talk: Two-dimensional GaN grown on Si(111)7x7 with assisted hyperthermal nitrogen ions at low temperature.

Internship

Weizmann Institute of Science, Rehovot, Israel. Group of prof. Ernesto Joselovich. Experimental work on *Kinetics of guided growth of horizontal GaN nanowires*.

References

- [1] Vilayanur S. Ramachandran. *The tell-tale brain: Unlocking the mystery of human nature*. Random House, 2012.
- [2] Klaus Schwab. The fourth industrial revolution. Crown Business, 2017.
- [3] Yuval N. Harari. Sapiens: A brief history of humankind. Random House, 2014.
- [4] R. Purohit, A. Mittal, S. Dalela, V. Warudkar, K. Purohit, and S. Purohit. Social, environmental and ethical impacts of nanotechnology. *Materials today: proceedings*, 4(4):5461–5467, 2017.
- [5] W. S. Alaloul, M. S. Liew, N. A. Zawawi Wan Abdullah, and I. B. Kennedy. Industrial revolution 4.0 in the construction industry: Challenges and opportunities for stakeholders. *Ain Shams Engineering Journal*, 2019.
- [6] G. Gurkaynak, I. Yilmaz, and G. Haksever. Stifling artificial intelligence: Human perils. *Computer Law & Security Review*, 32(5):749–758, 2016.
- [7] J. A. Buckley, P. B. Thompson, and K. P. Whyte. Collingridge's dilemma and the early ethical assessment of emerging technology: The case of nanotechnology enabled biosensors. *Technology in Society*, 48:54–63, 2017.
- [8] Semiconductor Industry Association. Worldwide semiconductor sales decrease 12 percent to \$412 billion in 2019. [online], URL: https://www.semiconductors.org/worldwide-semiconductor-sales-decrease-12-percent-to-412-billion-in-2019/, Last visited 16.3.2020.
- [9] World Economic Forum. A vission for a sustainable battery value chain in 2030. [online], URL: https://www.weforum.org/ reports/ a-vision-for-a-sustainable-battery-value-chain-in-2030, Last visited 16.3.2020.
- [10] ON Semiconductor. Wide bandgap technology enables future solar power solutions. [online], URL: https://www.onsemi.com/ blog/industrial-cloud-power/ wide-bandgap-enables-future-solar-power-solutions, Last visited 16.3.2020.
- [11] ON Semiconductor. Industry 4.0 robotics and emerging 48v. [online], URL: https://www.onsemi.com/ blog/industrial-cloud-power/ industry-4.0-robotics-and-emerging-48v, Last visited 16.3.2020.

- [12] McKinsey & Company. Internet of things: Opportunities and challenges for semiconductor companies. [online], URL: https://www.mckinsey.com/ industries/semiconductors/ our-insights/internet-of-things-opportunities-and-challenges-for-semiconductor-companies, Last visited 16.3.2020.
- [13] Deloitte. IoT opportunity in the world of semiconductor companies. [online], URL: https://www2.deloitte.com/ content/dam/Deloitte/us/Documents/technology/ ussemiconductor-internet-of-things.pdf, Last visited 16.3.2020.
- [14] Shuji Nakamura. Nobel lecture: Background story of the invention of efficient blue InGaN light emitting diodes. *Reviews of Modern Physics*, 87(4):1139, 2015.
- [15] A. P. P. Correia, P. M. Barquinha, and J. C. da Palma Goes. A Second-Order ΣΔ ADC Using Sputtered IGZO TFTs. Springer, 2015.
- [16] D. Y. Goswami, F. Kreith, and J. F. Kreider. *Principles of solar engineering*. CRC Press, 2000.
- [17] L. Lukasiak and A. Jakubowski. History of semiconductors. *Journal of Telecommunications and information technology*, pages 3–9, 2010.
- [18] F. Bassani and G. C. La Rocca. History of semiconductors. 2005.
- [19] Ferdinand Braun. On current conduction through metallic sulfides. In *Semiconductor Devices: Pioneering Papers*, pages 377–380. World Scientific, 1991.
- [20] Ch. Kittel, P. McEuen, and P. McEuen. *Introduction to solid state physics*, volume 8. Wiley New York, 1996.
- [21] Tudor Jenkins. A brief history of... semiconductors. *Physics education*, 40(5):430, 2005.
- [22] J. Bardeen and W. H. Brattain. The transistor, a semi-conductor triode. *Physical Review*, 74(2):230, 1948.
- [23] William Shockley. A unipolar "field-effect" transistor. *Proceedings of the IRE*, 40(11):1365–1376, 1952.
- [24] ITRS Group. International technology roadmap for semiconductors 2.0 more Moore. [online], URL: http://www.itrs2.net/ itrs-reports.html, Last visited 16.3.2020.

- [25] J. Wu and W. Walukiewicz. Band gaps of InN and group III nitride alloys. *Superlattices and Microstructures*, 34(1-2):63–75, 2003.
- [26] J. Wu, W. Walukiewicz, W. Shan, K. M. Yu, J. W. Ager, S. X. Li, E. E. Haller, H. Lu, and W. J. Schaff. Temperature dependence of the fundamental band gap of InN. *Journal of Applied Physics*, 94(7):4457–4460, 2003.
- [27] M. S. Prete, A. Mosca Conte, P. Gori, F. Bechstedt, and O. Pulci. Tunable electronic properties of two-dimensional nitrides for light harvesting heterostructures. *Applied Physics Letters*, 110(1):012103, 2017.
- [28] Z. Y. Al Balushi, K. Wang, R. K. Ghosh, R. l. A. Vila, S. M. Eichfeld, J. D. Caldwell, X. Qin, Y. Lin, P. l. A. DeSario, G. Stone, et al. Two-dimensional gallium nitride realized via graphene encapsulation. *Nature materials*, 15(11):1166, 2016.
- [29] Junqiao Wu. When group-III nitrides go infrared: New properties and perspectives. *Journal of Applied Physics*, 106(1):5, 2009.
- [30] D. Z. Ting, A. Soibel, A. Khoshakhlagh, S. A. Keo, B. Rafol, A. M. Fisher, B. J. Pepper, E. M. Luong, C. J. Hill, and S. D. Gunapala. Advances in III-V semiconductor infrared absorbers and detectors. *Infrared Physics & Technology*, 97:210–216, 2019.
- [31] A. Ajay, Y. Kotsar, and E. Monroy. Infrared emitters using III-nitride semiconductors. In *Nitride Semiconductor Light-Emitting Diodes (LEDs)*, pages 587–617. Elsevier, 2018.
- [32] H. P. Maruska and W. C. Rhines. A modern perspective on the history of semiconductor nitride blue light sources. *Solid-State Electronics*, 111:32–41, 2015.
- [33] Isamu Akasaki. Nobel lecture: Fascinated journeys into blue light. *Reviews of Modern Physics*, 87(4):1119, 2015.
- [34] Y. Li, M. Dvorak, P. N. Nesterenko, N. Nuchtavorn, and M. Macka. High power deep UV-LEDs for analytical optical instrumentation. *Sensors and Actuators B: Chemical*, 255:1238–1243, 2018.
- [35] Michael Shur. Wide band gap semiconductor technology: State-of-the-art. *Solid-State Electronics*, 155:65–75, 2019.

- [36] H. Morkoc, S. Strite, G. B. Gao, M. E. Lin, B. Sverdlov, and M. Burns. Large-band-gap SiC, III-V nitride, and II-VI ZnSe-based semiconductor device technologies. *Journal of Applied physics*, 76(3):1363–1398, 1994.
- [37] M. Razeghi and R. McClintock. A review of III-nitride research at the Center for Quantum Devices. *Journal of crystal growth*, 311(10):3067–3074, 2009.
- [38] A. Khan and K. Balakrishnan. III-nitride-based short-wavelength ultraviolet light sources. 2011.
- [39] A. L. Hicks, T. L. Theis, and M. L. Zellner. Emergent effects of residential lighting choices: prospects for energy savings. *Journal of Industrial Ecology*, 19(2):285–295, 2015.
- [40] J. Y. Tsao and P. Waide. The world's appetite for light: empirical data and trends spanning three centuries and six continents. *Leukos*, 6(4):259–281, 2010.
- [41] ON Semiconductors. Wide bandgap solutions. [online], URL: https://www.onsemi.com/PowerSolutions/, Last visited 16.3.2020.
- [42] M. Elbuluk and N. R. N. Idris. The role power electronics in future energy systems and green industrialization. In 2008 IEEE 2nd International Power and Energy Conference, pages 1–6. IEEE, 2008.
- [43] Rohm Semiconductors. Sic power devices and modules application note. [online], URL: https://d1d2qsbl8m0m72.cloudfront.net/en/products/databook/applinote/discrete/sic/common/sic-appli-e.pdf, Last visited 16.3.2020.
- [44] H. R. Chang, R. N. Gupta, C. Winterhalter, and E. Hanna. Comparison of 1200 V silicon carbide Schottky diodes and silicon power diodes. In *Collection of Technical Papers*. 35th Intersociety Energy Conversion Engineering Conference and Exhibit (IECEC)(Cat. No. 00CH37022), volume 1, pages 174–179. IEEE, 2000.
- [45] Y. Zhang, A. Dadgar, and T. Palacios. Gallium nitride vertical power devices on foreign substrates: a review and outlook. *Journal of Physics D: Applied Physics*, 51(27):273001, 2018.

- [46] S. Chowdhury, Z. Stum, Z. D. Li, K. Ueno, and T. P. Chow. Comparison of 600 V Si, SiC and GaN power devices. In *Materials Science Forum*, volume 778, pages 971–974. Trans Tech Publ, 2014.
- [47] A. A. Arendarenko, V. A. Oreshkin, Y. N. Sveshnikov, and I. N. Tsyplenkov. Trends in the development of the epitaxial nitride compounds technology. *Modern Electronic Materials*, 2(2):33–40, 2016.
- [48] Y. Zou, Y. Zhang, Y. Hu, and H. Gu. Ultraviolet detectors based on wide bandgap semiconductor nanowire: A review. *Sensors*, 18(7):2072, 2018.
- [49] P. Schreiber, T. Dang, T. Pickenpaugh, G. A. Smith, P. Gehred, and C. W. Litton. Solar-blind UV region and UV detector development objectives. In *Photodetectors: Materials and Devices IV*, volume 3629, pages 230–248. International Society for Optics and Photonics, 1999.
- [50] A. Gonzalez-Perez, K. M. Persson, and L. Samuelson. Semiconductor eco-materials for water treatment. 2019.
- [51] A. Mills, R. H. Davies, and D. Worsley. Water purification by semiconductor photocatalysis. *Chemical Society Reviews*, 22(6):417–425, 1993.
- [52] Y. Li, F. Chen, R. He, Y. Wang, and N. Tang. Semiconductor photocatalysis for water purification. In *Nanoscale Materials in Water Purification*, pages 689–705. Elsevier, 2019.
- [53] S. Zhao, H. P. T. Nguyen, M. G. Kibria, and Z. Mi. III-nitride nanowire optoelectronics. *Progress in Quantum Electronics*, 44:14–68, 2015.
- [54] P. Li and X. Meng. Thermal annealing effects on the optoelectronic characteristics of fully nanowire-based UV detector. *Journal of Materials Science: Materials in Electronics*, 27(7):7693–7698, 2016.
- [55] F. Liu, L. Li, T. Guo, H. Gan, X. Mo, J. Chen, S. Deng, and N. Xu. Investigation on the photoconductive behaviors of an individual AlN nanowire under different excited lights. *Nanoscale research letters*, 7(1):454, 2012.

- [56] C. Zhao, N. Alfaraj, R. Ch. Subedi, J. W. Liang, A. A. Alatawi, A. A. Alhamoud, M. Ebaid, M. S. Alias, T. K. Ng, and B. S. Ooi. III-nitride nanowires on unconventional substrates: From materials to optoelectronic device applications. *Progress in Quantum Electronics*, 61:1–31, 2018.
- [57] J. Maniš, J. Mach, M. Bartošík, T. Šamořil, Michal Horak, V. Čalkovský, D. Nezval, L. Kachtik, M. Konečny, and T. Šikola. Low temperature 2D GaN growth on Si (111) 7x7 assisted by hypethermal nitrogen ions. *Nanoscale Advances*, 4:3549–3556, 2022.
- [58] A. Rothman, J. Maniš, V. G. Dubrovskii, T. Šikola, J. Mach, and E. Joslevich. Kinetics of guided growth of horizontal GaN nanowires on flat and faceted sapphire surfaces. *Nanomaterials*, 11(3):624, 2021.
- [59] John R. Arthur. Molecular beam epitaxy. Surface science, 500(1-3):189-217, 2002.
- [60] T. D. Moustakas, E. Iliopoulos, A. V. Sampath, H. M. Ng, D. Doppalapudi, M. Misra, D. Korakakis, and R. Singh. Growth and device applications of III-nitrides by MBE. *Journal of crystal growth*, 227:13–20, 2001.
- [61] Q. D. Zhuang. Molecular beam epitaxy growth of nitride semiconductors. In *Nitride Semiconductor Light-Emitting Diodes (LEDs)*, pages 3–26. Elsevier, 2014.
- [62] S. Yamada, H. Higashi, T. Kanashima, and K. Hamaya. Growth of ferromagnetic Co2FeSi films on flexible Ge (111). *Materials Science in Semiconductor Processing*, 112:104997, 2020.
- [63] P. Chang, W. C. Lee, T. D. Lin, C. H. Hsu, J. Kwo, and M. Hong. MBEâ€"enabling technology beyond Si CMOS. *Journal of crystal growth*, 323(1):511–517, 2011.
- [64] S. Voborný, M. Kolíbal, P. Bábor, S. Pruša, J. Spousta, and T. Šikola. Deposition and in-situ characterization of ultra-thin films. *Thin solid films*, 459(1-2):17–22, 2004.
- [65] S. Sanguinetti, S. Bietti, and N. Koguchi. Droplet epitaxy of nanostructures. In *Molecular Beam Epitaxy*, pages 293–314. Elsevier, 2018.
- [66] S. Bietti, C. Somaschini, and S. Sanguinetti. Crystallization kinetics of Ga metallic nano-droplets under As flux. *Nanotechnology*, 24(20):205603, 2013.
- [67] C. Somaschini, S. Bietti, N. Koguchi, and S. Sanguinetti. Fabrication of multiple concentric nanoring structures. *Nano letters*, 9(10):3419–3424, 2009.

- [68] C. Somaschini, S. Bietti, N. Koguchi, and S. Sanguinetti. Coupled quantum dot–ring structures by droplet epitaxy. *Nanotechnology*, 22(18):185602, 2011.
- [69] J. Mach, T. Šamoril, S. Voborný, M. Kolibal, J. Zlámal, J. Spousta, L. Dittrichová, and T. Šikola. An ultra-low energy (30–200 eV) ion-atomic beam source for ion-beam-assisted deposition in ultrahigh vacuum. *Review of Scientific Instruments*, 82(8):083302, 2011.
- [70] K. Oura, M. Katayama, A. V. Zotov, V. G. Lifshits, and A. A. Saranin. Elementary processes at surfaces: Surface diffusion. In *Surface Science*, pages 325–356. Springer, 2003.
- [71] Rep Gomer. Diffusion of adsorbates on metal surfaces. *Reports on progress in Physics*, 53(7):917, 1990.
- [72] Axel Gross. Theoretical surface science. A Microscopic Perspective. Originally published in the series: Advanced Texts in Physics,, 132, 2003.
- [73] S. Bietti, C. Somaschini, L. Esposito, A. Fedorov, and S. Sanguinetti. Gallium surface diffusion on GaAs (001) surfaces measured by crystallization dynamics of Gadroplets. *Journal of Applied Physics*, 116(11):114311, 2014.
- [74] J. N. Shapiro, A. Lin, D. L. Huffaker, and C. Ratsch. Potential energy surface of In and Ga adatoms above the (111) and (110) surfaces of GaAs nanopillars. *Physical Review B*, 84(8):085322, 2011.
- [75] X. Xia, S. Xie, M. Liu, H. Ch. Peng, N. Lu, J. Wang, M. J. Kim, and Y. Xia. On the role of surface diffusion in determining the shape or morphology of noble-metal nanocrystals. *Proceedings of the National Academy of Sciences*, 110(17):6669–6673, 2013.
- [76] Tom Kuech. Handbook of Crystal Growth: Thin Films and Epitaxy. Elsevier, 2014.
- [77] Peter W. Voorhees. The theory of Ostwald ripening. *Journal of Statistical Physics*, 38(1-2):231–252, 1985.
- [78] A. Baldan. Review progress in Ostwald ripening theories and their applications to nickel-base superalloys part i: Ostwald ripening theories. *Journal of materials science*, 37(11):2171–2202, 2002.

- [79] D. V. Alexandrov. On the theory of Ostwald ripening: formation of the universal distribution. *Journal of Physics A: Mathematical and Theoretical*, 48(3):035103, 2014.
- [80] M. Asmann, J. Heberlein, and E. Pfender. A review of diamond CVD utilizing halogenated precursors. *Diamond and related materials*, 8(1):1–16, 1999.
- [81] M. Schwander and K. Partes. A review of diamond synthesis by CVD processes. *Diamond and related materials*, 20(9):1287–1301, 2011.
- [82] Madhav Datta. Electrochemical processing technologies in chip fabrication: challenges and opportunities. *Electrochimica acta*, 48(20-22):2975–2985, 2003.
- [83] P. C. McIntyre and A. F. Morral. Semiconductor nanowires: To grow or not to grow? *Materials Today Nano*, page 100058, 2019.
- [84] B. Alloing and J. Zuniga-Perez. Metalorganic chemical vapor deposition of GaN nanowires: From catalyst-assisted to catalyst-free growth, and from self-assembled to selective-area growth. *Materials Science in Semiconductor Processing*, 55:51–58, 2016.
- [85] M. P. Lu, M. Y. Lu, and L. J. Chen. p-type ZnO nanowires: From synthesis to nanoenergy. *Nano Energy*, 1(2):247–258, 2012.
- [86] B. Li, B. Mao, X. Wang, and T. He. Fabrication and frictional wear property of bamboo-like SiC nanowires reinforced SiC coating. *Surface and Coatings Technology*, page 125647, 2020.
- [87] X. J. Lee, B. Y. Z. Hiew, K. C. Lai, L. Y. Lee, S. Gan, S. Thangalazhy-Gopakumar, and S. Rigby. Review on graphene and its derivatives: Synthesis methods and potential industrial implementation. *Journal of the Taiwan Institute of Chemical Engineers*, 98:163–180, 2019.
- [88] T. Kente and S. D. Mhlanga. Gallium nitride nanostructures: Synthesis, characterization and applications. *Journal of Crystal Growth*, 444:55–72, 2016.
- [89] M. H. Kane and N. Arefin. Gallium nitride on silicon substrates for LEDs. In *Nitride Semiconductor Light-Emitting Diodes*, pages 99–143. Elsevier, 2014.
- [90] Victor Bermudez. The fundamental surface science of wurtzite gallium nitride. *Surface Science Reports*, 72(4):147–315, 2017.

- [91] E. S. Hellman. The polarity of GaN: a critical review. *Materials Research Society Internet Journal of Nitride Semiconductor Research*, 3, 1998.
- [92] S. Strite and H. Morkoç. GaN, AlN, and InN: a review. *Journal of Vacuum Science & Technology B: Microelectronics and Nanometer Structures Processing, Measurement, and Phenomena*, 10(4):1237–1266, 1992.
- [93] J. Neugebauer and C. G. Van de Walle. Gallium vacancies and the yellow luminescence in GaN. *Applied Physics Letters*, 69(4):503–505, 1996.
- [94] M. A. Reshchikov, H. Morkoc, S. S. Park, and K. Lee. Yellow and green luminescence in a freestanding GaN template. *Applied Physics Letters*, 78(20):3041–3043, 2001.
- [95] I. Vurgaftman, J. Meyer, and L. Ram-Mohan. Band parameters for III–V compound semiconductors and their alloys. *Journal of applied physics*, 89(11):5815–5875, 2001.
- [96] M. E. Levinshtein, S. L. Rumyantsev, and M. S. Shur. *Properties of Advanced Semiconductor Materials: GaN, AlN, InN, BN, SiC, SiGe*. John Wiley & Sons, 2001.
- [97] A. S. Augustine Fletcher and D. Nirmal. A survey of gallium nitride HEMT for RF and high power applications. *Superlattices and Microstructures*, 109:519–537, 2017.
- [98] Chris G. Van de Walle. Defects and doping in GaN. equilibrium, 5(14):15, 1997.
- [99] H. Amano, Y. Baines, E. Beam, M. Borga, T. Bouchet, P. R. Chalker, M. Charles, K. J. Chen, N. Chowdhury, R. Chu, et al. The 2018 gallium nitride power electronics roadmap. *Journal of Physics D: Applied Physics*, 51(16):163001, 2018.
- [100] W. Kim, O. Aktas, A. Salvador, A. Botchkarev, B. Sverdlov, S. N. Mohammad, and H. Morkoç. MBE grown high quality GaN films and devices. *Solid-State Electronics*, 41(2):169–175, 1997.
- [101] S. Sienz, J. W. Gerlach, T. Höche, A. Sidorenko, T. G. Mayerhöfer, G. Benndorf, and B. Rauschenbach. Comparison of ion-beam-assisted molecular beam epitaxy with conventional molecular beam epitaxy of thin hexagonal gallium nitride films. *Journal of crystal growth*, 264(1-3):184–191, 2004.
- [102] M. Mensing, P. Schumacher, J. W. Gerlach, S. Herath, A. Lotnyk, and B. Rauschenbach. Influence of nitrogen ion species on mass-selected low energy ion-assisted growth of epitaxial GaN thin films. *Applied Surface Science*, 498:143830, 2019.

- [103] J. W. Gerlach, T. Hoche, F. Frost, and B. Rauschenbach. Ion beam assisted MBE of GaN on epitaxial TiN films. *Thin solid films*, 459(1-2):13–16, 2004.
- [104] H. Lu, C. Reese, S. Jeon, A. Sundar, Y. Fan, E. Rizzi, Y. Zhuo, L. Qi, and R. S. Goldman. Mechanisms of GaN quantum dot formation during nitridation of Ga droplets. *Applied Physics Letters*, 116(6):062107, 2020.
- [105] Y. Z. Su and I. S. Yu. Crystal structures of GaN nanodots by nitrogen plasma treatment on Ga metal droplets. *Metals*, 8(6):419, 2018.
- [106] T. Kouno, M. Sakai, K. Kishino, A. Kikuchi, N. Umehara, and K. Hara. Crystal structure and optical properties of a high-density ingan nanoumbrella array as a white light source without phosphors. *NPG Asia Materials*, 8(7):e289–e289, 2016.
- [107] J. Mach, J. Piastek, J. Maniš, V. Čalkovský, T. Šamořil, J. Damková, M. Bartošík, S. Voborný, M. Konečný, and T. Šikola. Low temperature selective growth of GaN single crystals on pre-patterned Si substrates. *Applied Surface Science*, 497:143705, 2019.
- [108] W. Wang, H. Wang, W. Yang, Y. Zhu, and G. Li. A new approach to epitaxially grow high-quality GaN films on Si substrates: the combination of MBE and PLD. *Scientific Reports*, 6:24448, 2016.
- [109] K. Chung, H. Oh, J. Jo, K. Lee, M. Kim, and G. C. Yi. Transferable single-crystal GaN thin films grown on chemical vapor-deposited hexagonal BN sheets. *NPG Asia Materials*, 9(7):e410–e410, 2017.
- [110] Z. Y. Al Balushi, T. Miyagi, Y. C. Lin, K. Wang, L. Calderin, G. Bhimanapati, J. M. Redwing, and J. A. Robinson. The impact of graphene properties on GaN and AlN nucleation. *Surface Science*, 634:81–88, 2015.
- [111] L. Goswami, R. Pandey, and G. Gupta. Epitaxial growth of GaN nanostructure by PA-MBE for UV detection application. *Applied Surface Science*, 449:186–192, 2018.
- [112] T. Journot, V. Bouchiat, B. Gayral, J. Dijon, and B. Hyot. Self-assembled UV photodetector made by direct epitaxial GaN growth on graphene. *ACS applied materials & interfaces*, 10(22):18857–18862, 2018.

- [113] P. Blake, E. W. Hill, A. H. Castro Neto, K. S. Novoselov, D. Jiang, R. Yang, T. J. Booth, and A. K. Geim. Making graphene visible. *Applied physics letters*, 91(6):063124, 2007.
- [114] I. Childres, L. A. Jauregui, W. Park, H. Cao, Y. P. Chen, et al. Raman spectroscopy of graphene and related materials. *New developments in photon and materials research*, 1:1–20, 2013.
- [115] T. M. G. Mohiuddin, A. Lombardo, R. R. Nair, A. Bonetti, G. Savini, R. Jalil, N. Bonini, D. M. Basko, C. Galiotis, N. Marzari, et al. Uniaxial strain in graphene by raman spectroscopy: G peak splitting, Grüneisen parameters, and sample orientation. *Physical Review B*, 79(20):205433, 2009.
- [116] I. Childres, L. A. Jauregui, J. Tian, and Y. P. Chen. Effect of oxygen plasma etching on graphene studied using Raman spectroscopy and electronic transport measurements. *New Journal of Physics*, 13(2):025008, 2011.
- [117] L. Ravi, K. Boopathi, P. Panigrahi, and B. Krishnan. Growth of gallium nitride nanowires on sapphire and silicon by chemical vapor deposition for water splitting applications. *Applied Surface Science*, 449:213–220, 2018.
- [118] J. W. Gerlach, T. Ivanov, L. Neumann, T. Hoche, D. Hirsch, and B. Rauschenbach. Epitaxial GaN films by hyperthermal ion-beam nitridation of Ga droplets. *Journal of Applied Physics*, 111(11):113521, 2012.
- [119] P. Procházka. Fabrication of graphene and study of its physical properties. *PhD these, Brno University of Technology*, 2018.
- [120] J. Mach, P. Procházka, M. Bartošík, D. Nezval, J. Piastek, J. Hulva, V. Švarc, M. Konečný, L. Kormoš, and T. Šikola. Electronic transport properties of graphene doped by gallium. *Nanotechnology*, 28(41):415203, 2017.
- [121] A. K. Geim and K. S. Novoselov. The rise of graphene. In *Nanoscience and Technology:* A Collection of Reviews from Nature Journals, pages 11–19. World Scientific, 2010.
- [122] N. Mounet, M. Gibertini, P. Schwaller, D. Campi, A. Merkys, A. Marrazzo, T. Sohier, A. Castelli, I. E.and Cepellotti, G. Pizzi, et al. Two-dimensional materials from high-throughput computational exfoliation of experimentally known compounds. *Nature nanotechnology*, 13(3):246–252, 2018.

- [123] S. Haastrup, M. Strange, M. Pandey, T. Deilmann, P. S. Schmidt, N. F. Hinsche, M. N. Gjerding, D. Torelli, P. M. Larsen, A. C. Riis-Jensen, et al. The computational 2D materials database: high-throughput modeling and discovery of atomically thin crystals. 2D Materials, 5(4):042002, 2018.
- [124] C. R. Dean, A. F. Young, I. Meric, C. Lee, L. Wang, S. Sorgenfrei, K. Watanabe, T. Taniguchi, P. Kim, K. L. Shepard, et al. Boron nitride substrates for high-quality graphene electronics. *Nature nanotechnology*, 5(10):722, 2010.
- [125] L. Britnell, R. V. Gorbachev, R. Jalil, B. D. Belle, F. Schedin, A. Mishchenko, T. Georgiou, M. I. Katsnelson, L. Eaves, S. V. Morozov, et al. Field-effect tunneling transistor based on vertical graphene heterostructures. *Science*, 335(6071):947–950, 2012.
- [126] K. Zhang, Y. Feng, F. Wang, Z. Yang, and J. Wang. Two dimensional hexagonal boron nitride 2D-hBN: synthesis, properties and applications. *Journal of Materials Chemistry C*, 5(46):11992–12022, 2017.
- [127] L. H. Li and Y. Chen. Atomically thin boron nitride: unique properties and applications. *Advanced Functional Materials*, 26(16):2594–2608, 2016.
- [128] G. R. Bhimanapati, N. R. Glavin, and J. A. Robinson. 2D boron nitride: synthesis and applications. In *Semiconductors and Semimetals*, volume 95, pages 101–147. Elsevier, 2016.
- [129] H. Sahin, S. Cahangirov, M. Topsakal, E. Bekaroglu, E. Akturk, R. T. Senger, and S. Ciraci. Monolayer honeycomb structures of group-IV elements and III-V binary compounds: First-principles calculations. *Physical Review B*, 80(15):155453, 2009.
- [130] M. G. Ahangari, A. Fereidoon, and A. H. Mashhadzadeh. Interlayer interaction and mechanical properties in multi-layer graphene, boron nitride, aluminum nitride and gallium nitride graphene-like structure: A quantum-mechanical DFT study. *Superlattices and Microstructures*, 112:30–45, 2017.
- [131] Q. Peng, X. J. Chen, S. Liu, and S. De. Mechanical stabilities and properties of graphene-like aluminum nitride predicted from first-principles calculations. *RSC advances*, 3(19):7083–7092, 2013.

- [132] J. V. N. Sarma, R. Chowdhury, and R. Jayaganthan. Mechanical behavior of gallium nitride nanosheets using molecular dynamics. *Computational materials science*, 75:29–34, 2013.
- [133] A. Onen, D. Kecik, E. Durgun, and S. Ciraci. GaN: From three- to two-dimensional single-layer crystal and its multilayer van der Waals solids. *Physical Review B*, 93(8):085431, 2016.
- [134] A. Onen, D. Kecik, E. Durgun, and S. Ciraci. Onset of vertical bonds in new GaN multilayers: beyond van der Waals solids. *Nanoscale*, 10(46):21842–21850, 2018.
- [135] F. Hussain, Y. Q. Cai, M. J. I. Khan, M. Imran, M. Rashid, H. Ullah, E. Ahmad, F. Kousar, and S. A. Ahmad. Enhanced ferromagnetic properties of Cu doped two-dimensional GaN monolayer. *International Journal of Modern Physics C*, 26(01):1550009, 2015.
- [136] S. Wang, Y. An, C. Xie, H. Zhang, and Q. Zeng. First-principles prediction of ferromagnetism in transition-metal doped monolayer AlN. *Superlattices and Microstructures*, 122:171–180, 2018.
- [137] N. Alaal and I. S. Roqan. Tuning the electronic properties of hexagonal two-dimensional GaN monolayers via doping for enhanced optoelectronic applications. *ACS Applied Nano Materials*, 2(1):202–213, 2018.
- [138] R. Gonzalez, W. Lopez-Perez, A. Gonzalez-Garcia, M. G. Moreno-Armenta, and R. Gonzalez-Hernandez. Vacancy charged defects in two-dimensional GaN. *Applied Surface Science*, 433:1049–1055, 2018.
- [139] L. Tong, J. He, M. Yang, Z. Chen, J. Zhang, Y. Lu, and Z. Zhao. Anisotropic carrier mobility in buckled two-dimensional GaN. *Physical Chemistry Chemical Physics*, 19(34):23492–23496, 2017.
- [140] X. Zhang, L. Jin, X. Dai, G. Chen, and G. Liu. Two-dimensional GaN an excellent electrode material providing fast ion diffusion and high storage capacity for Li-ion and Na-ion batteries. *ACS applied materials & interfaces*, 10(45):38978–38984, 2018.
- [141] M. Moradi and N. Naderi. First principle study of hydrogen storage on the graphene-like aluminum nitride nanosheet. *Structural Chemistry*, 25(4):1289–1296, 2014.

- [142] M. Chhowalla, D. Jena, and H. Zhang. Two-dimensional semiconductors for transistors. *Nature Reviews Materials*, 1(11):1–15, 2016.
- [143] Q. Hao, H. Zhao, and Y. Xiao. A hybrid simulation technique for electrothermal studies of two-dimensional GaN-on-SiC high electron mobility transistors. *Journal of Applied Physics*, 121(20):204501, 2017.
- [144] N. Sanders, D. Bayerl, G. Shi, K. A. Mengle, and E. Kioupakis. Electronic and optical properties of two-dimensional GaN from first-principles. *Nano letters*, 17(12):7345–7349, 2017.
- [145] C. Feng, H. Qin, D. Yang, and G. Zhang. First-principles investigation of the adsorption behaviors of CH2O on BN, AlN, GaN, InN, BP, and P monolayers. *Materials*, 12(4):676, 2019.
- [146] C. Pashartis and O. Rubel. Alloying strategy for two-dimensional GaN optical emitters. *Physical Review B*, 96(15):155209, 2017.
- [147] S. Pimputkar, J. S. Speck, S. P. DenBaars, and S. Nakamura. Prospects for LED lighting. *Nature photonics*, 3(4):180–182, 2009.
- [148] P. Tsipas, S. Kassavetis, D. Tsoutsou, E. Xenogiannopoulou, E. Golias, S. A. Giamini, C. Grazianetti, D. Chiappe, A. Molle, M. Fanciulli, et al. Evidence for graphite-like hexagonal AlN nanosheets epitaxially grown on single crystal Ag (111). *Applied Physics Letters*, 103(25):251605, 2013.
- [149] V. Mansurov, T. Malin, Y. Galitsyn, and K. Zhuravlev. Graphene-like AlN layer formation on (111) Si surface by ammonia molecular beam epitaxy. *Journal of Crystal Growth*, 428:93–97, 2015.
- [150] T. Malin, V. Mansurov, Y. Galitsyn, and K. Zhuravlev. 2D AlN crystal phase formation on (0001) Al2O3 surface by ammonia MBE. *physica status solidi c*, 12(4-5):443–446, 2015.
- [151] W. Wang, Y. Li, Y. Zheng, X. Li, L. Huang, and G. Li. Lattice structure and bandgap control of 2D GaN grown on graphene/Si heterostructures. *Small*, 15(14):1802995, 2019.

- [152] W. Wang, Y. Zheng, X. Li, Y. Li, H. Zhao, L. Huang, Z. Yang, X. Zhang, and G. Li. 2D AlN layers sandwiched between graphene and Si substrates. *Advanced Materials*, 31(2):1803448, 2019.
- [153] Y. Chen, K. Liu, J. Liu, T. Lu, B. Wei, T. Zhang, M. Zeng, Z. Wang, and L. Fu. Growth of 2D GaN single crystals on liquid metals. *Journal of the American Chemical Society*, 140(48):16392–16395, 2018.
- [154] M. Leszczynski, H. Teisseyre, T. Suski, I. Grzegory, M. Bockowski, J. Jun, S. Porowski, K. Pakula, J. M. Baranowski, C. T. Foxon, et al. Lattice parameters of gallium nitride. *Applied Physics Letters*, 69(1):73–75, 1996.
- [155] Chris G. Van de Walle. Effects of impurities on the lattice parameters of GaN. *Physical Review B*, 68(16):165209, 2003.
- [156] Y. Gao and S. Okada. Energetics and electronic structures of thin films and heterostructures of a hexagonal GaN sheet. *Japanese Journal of Applied Physics*, 56(6):065201, 2017.
- [157] D. Xu, H. He, R. Pandey, and S. P. Karna. Stacking and electric field effects on the electronic properties of the layered GaN. *arXiv* preprint *arXiv* 1302.5157, 2013.
- [158] V. Darakchieva, P. P. Paskov, T. Paskova, E. Valcheva, B. Monemar, and M. Heuken. Lattice parameters of GaN layers grown on a-plane sapphire: Effect of in-plane strain anisotropy. *Applied physics letters*, 82(5):703–705, 2003.
- [159] Celal Yelgel. First-principles modeling of GaN/MoSe van der Waals heterobilayer. *Turkish Journal of Physics*, 41(5):463–468, 2017.
- [160] A. H. Al-Bayati, K. G. Orrman-Rossiter, J. A. Van den Berg, and D. G. Armour. Composition and structure of the native Si oxide by high depth resolution medium energy ion scattering. *Surface science*, 241(1-2):91–102, 1991.
- [161] M. Khoury, O. Tottereau, G. Feuillet, P. Vennegues, and J. Zuniga-Perez. Evolution and prevention of meltback etching: Case study of semipolar GaN growth on patterned silicon substrates. *Journal of Applied Physics*, 122(10):105108, 2017.

- [162] D. Dorranian, P. Azadfar, A. H. Sari, S. Ghorbani, A. Hojabri, and M. Ghoranneviss. Structural and optical properties of silicon nitride film generated on Si substrate by low energy ion implantation. *The European Physical Journal-Applied Physics*, 42(2):103–107, 2008.
- [163] V. I. Bachurin, A. B. Churilov, E. V. Potapov, V. K. Smirnov, V. V. Makarov, and A. B. Danilin. Formation of thin silicon nitride layers on Si by low energy N2+ ion bombardment. *Nuclear Instruments and Methods in Physics Research Section B: Beam Interactions with Materials and Atoms*, 147(1-4):316–319, 1999.
- [164] Z. M. Ren, Z. F. Ying, X. X. Xiong, M. Q. He, F. M. Li, Y. C. Du, and L. Y. Cheng. Study of the growth of thin nitride films under low-energy nitrogen-ion bombardment. *Applied Physics A*, 58(4):395–399, 1994.
- [165] O. C. Hellman, O. Vancauwenberghe, N. Herbots, J. Olson, R. J. Culbertson, and W. J. Croft. Structure and properties of silicon nitride and SixGe1-x nitride prepared by direct low energy ion beam nitridation. *Materials Science and Engineering: B*, 12(1-2):53–59, 1992.
- [166] I. Kusunoki, T. Takaoka, Y. Igari, and K. Ohtsuka. Nitridation of a Si (100) surface by 100–1000 eV N+ 2 ion beams. *The Journal of chemical physics*, 101(9):8238–8245, 1994.
- [167] F. Cerrina and C. Marrian. A path to nanolithography. *Mrs Bulletin*, 21(12):56–62, 1996.
- [168] R. S. Wagner and W. C. Ellis. Vapor-liquid-solid mechanism of single crystal growth. *Applied physics letters*, 4(5):89–90, 1964.
- [169] L. Z Pei and Z. Y Cai. A review on germanium nanowires. *Recent Patents on Nanotechnology*, 6(1):44–59, 2012.
- [170] M. I. B. Utama, J. Zhang, R. Chen, X. Xu, D. Li, H. Sun, and Q. Xiong. Synthesis and optical properties of II–VI 1D nanostructures. *Nanoscale*, 4(5):1422–1435, 2012.
- [171] E. Barrigon, M. Heurlin, Z. Bi, B. Monemar, and L. Samuelson. Synthesis and applications of III–V nanowires. *Chemical reviews*, 119(15):9170–9220, 2019.

- [172] J. Im, J. Luo, M. Franckeviccius, N. Pellet, P. Gao, T. Moehl, S. M. Zakeeruddin, M. K. Nazeeruddin, M. Gratzel, and N. Park. Nanowire perovskite solar cell. *Nano letters*, 15(3):2120–2126, 2015.
- [173] Y. Cui, X. Duan, J. Hu, and C. M. Lieber. Doping and electrical transport in silicon nanowires. *The journal of physical chemistry B*, 104(22):5213–5216, 2000.
- [174] D. J. Sirbuly, M. Law, P. Pauzauskie, H. Yan, A. V. Maslov, K. Knutsen, C. Ning, R. J. Saykally, and P. Yang. Optical routing and sensing with nanowire assemblies. *Proceedings of the National Academy of Sciences*, 102(22):7800–7805, 2005.
- [175] F. Qian, Y. Li, S. Gradecak, H. Park, Y. Dong, Y. Ding, Z. L. Wang, and C. M. Lieber. Multi-quantum-well nanowire heterostructures for wavelength-controlled lasers. *Nature materials*, 7(9):701–706, 2008.
- [176] R. F. Oulton, V. J. Sorger, T. Zentgraf, R. Ma, C. Gladden, L. Dai, G. Bartal, and X. Zhang. Plasmon lasers at deep subwavelength scale. *Nature*, 461(7264):629–632, 2009.
- [177] Y. Xia, P. Yang, Y. Sun, Y. Wu, B. Mayers, B. Gates, Y. Yin, F. Kim, and H. Yan. One-dimensional nanostructures: synthesis, characterization, and applications. *Advanced materials*, 15(5):353–389, 2003.
- [178] N. P. Dasgupta, J. Sun, C. Liu, S. Brittman, S. C. Andrews, J. Lim, H. Gao, R. Yan, and P. Yang. 25th anniversary article: semiconductor nanowires–synthesis, characterization, and applications. *Advanced materials*, 26(14):2137–2184, 2014.
- [179] N. G. Chopra, R.J. Luyken, K. Cherrey, V. H. Crespi, M. L. Cohen, S. G. Louie, and A. Zettl. Boron nitride nanotubes. *Science*, 269(5226):966–967, 1995.
- [180] D. Golberg, Y. Bando, C. C. Tang, and C. Y. Zhi. Boron nitride nanotubes. *Advanced Materials*, 19(18):2413–2432, 2007.
- [181] W. Han, S. Fan, Q. Li, and Y. Hu. Synthesis of gallium nitride nanorods through a carbon nanotube: confined reaction. *Science*, 277(5330):1287–1289, 1997.
- [182] J. Goldberger, R. He, Y. Zhang, S. Lee, H. Yan, H. J. Choi, and P. Yang. Single-crystal gallium nitride nanotubes. *Nature*, 422(6932):599, 2003.

- [183] D. Tsivion, M. Schvartzman, R. Popovitz-Biro, P. von Huth, and E. Joselevich. Guided growth of millimeter-long horizontal nanowires with controlled orientations. *Science*, 333(6045):1003–1007, 2011.
- [184] D. Tsivion and E. Joselevich. Guided growth of epitaxially coherent GaN nanowires on SiC. *Nano letters*, 13(11):5491–5496, 2013.
- [185] L. Goren-Ruck, D. Tsivion, M. Schvartzman, R. Popovitz-Biro, and E. Joselevich. Guided growth of horizontal GaN nanowires on quartz and their transfer to other substrates. *ACS nano*, 8(3):2838–2847, 2014.
- [186] D. Tsivion and E. Joselevich. Guided growth of horizontal GaN nanowires on spinel with orientation-controlled morphologies. *The Journal of Physical Chemistry C*, 118(33):19158–19164, 2014.
- [187] M. Schvartzman, D. Tsivion, D. Mahalu, O. Raslin, and E. Joselevich. Self-integration of nanowires into circuits via guided growth. *Proceedings of the National Academy of Sciences*, 110(38):15195–15200, 2013.
- [188] Heon-Jin Choi. Vapor-liquid-solid growth of semiconductor nanowires. In *Semiconductor Nanostructures for Optoelectronic Devices*, pages 1–36. Springer, 2012.
- [189] V. G. Dubrovskii, G. E. Cirlin, I. P. Soshnikov, A. A. Tonkikh, N. V. Sibirev, Y. B. Samsonenko, and V. M. Ustinov. Diffusion-induced growth of GaAs nanowhiskers during molecular beam epitaxy: Theory and experiment. *Physical review B*, 71(20):205325, 2005.
- [190] X. Zhang, V. G. Dubrovskii, N. V. Sibirev, G. E. Cirlin, C. Sartel, M. Tchernycheva, J. C. Harmand, and F. Glas. Growth of inclined GaAs nanowires by molecular beam epitaxy: theory and experiment. *Nanoscale research letters*, 5(10):1692, 2010.
- [191] A. Rothman, V. G. Dubrovskii, and E. Joselevich. Kinetics and mechanism of planar nanowire growth. *Proceedings of the National Academy of Sciences*, 117(1):152–160, 2020.
- [192] A. H. Chin, T. S. Ahn, H. Li, S. Vaddiraju, C. J. Bardeen, C.g Ning, and M. K. Sunkara. Photoluminescence of GaN nanowires of different crystallographic orientations. *Nano letters*, 7(3):626–631, 2007.

- [193] J. Thapa, B. Liu, S. D. Woodruff, B. T. Chorpening, and M. P. Buric. Raman scattering in single-crystal sapphire at elevated temperatures. *Applied optics*, 56(31):8598–8606, 2017.
- [194] A. Hushur, M. H. Manghnani, and J. Narayan. Raman studies of GaN/sapphire thin film heterostructures. *Journal of Applied Physics*, 106(5):054317, 2009.
- [195] M. Katsikini, K. Papagelis, E. C. Paloura, and S. Ves. Raman study of Mg, Si, O, and N implanted GaN. *Journal of Applied Physics*, 94(7):4389–4394, 2003.
- [196] C. Wen, M. C. Reuter, J. Bruley, J. Tersoff, S. Kodambaka, E. A. Stach, and F. M. Ross. Formation of compositionally abrupt axial heterojunctions in silicon-germanium nanowires. *Science*, 326(5957):1247–1250, 2009.
- [197] B. J. Kim, J. Tersoff, C. Wen, M. C. Reuter, E. A. Stach, and F. M. Ross. Determination of size effects during the phase transition of a nanoscale Au-Si eutectic. *Physical review letters*, 103(15):155701, 2009.
- [198] B. J. Kim, J. Tersoff, S. Kodambaka, M. C. Reuter, E. A. Stach, and F. M. Ross. Kinetics of individual nucleation events observed in nanoscale vapor-liquid-solid growth. *Science*, 322(5904):1070–1073, 2008.
- [199] V. G. Dubrovskii, N. V. Sibirev, J. C. Harmand, and F. Glas. Growth kinetics and crystal structure of semiconductor nanowires. *Physical Review B*, 78(23):235301, 2008.
- [200] J. B. Hannon, S. Kodambaka, F. M. Ross, and R. M. Tromp. The influence of the surface migration of gold on the growth of silicon nanowires. *nature*, 440(7080):69–71, 2006.
- [201] C. B. Maliakkal, N. Hatui, R. D. Bapat, B. A. Chalke, A. A. Rahman, and A. Bhattacharya. The mechanism of Ni-assisted GaN nanowire growth. *Nano letters*, 16(12):7632–7638, 2016.
- [202] V. G. Dubrovskii, N. V. Sibirev, G. E. Cirlin, I. P. Soshnikov, W. H. Chen, R. Larde, E. Cadel, P. Pareige, T. Xu, B. Grandidier, et al. Gibbs-thomson and diffusion-induced contributions to the growth rate of Si, InP, and GaAs nanowires. *Physical Review B*, 79(20):205316, 2009.